UNIVERSITY OF CALIFORNIA,
IRVINE

Mathematical modeling of collective cell migration in wound healing

DISSERTATION

submitted in partial satisfaction of the requirements
for the degree of

DOCTOR OF PHILOSOPHY

in Mathematics

by

Jinghao Chen

Dissertation Committee:
Chancellor's Professor John S. Lowengrub, Chair
Professor Medha M. Pathak
Professor Long Chen

2024

DEDICATION

To my mother and father

TABLE OF CONTENTS

LIST OF FIGURES

3.1 **PIEZO1 activity is predicted to regulate wound closure by hindering coordinated directionality**. **(A)** Schematic depicting experimentally measured features used to generate the single cell migration dataset. Left, representative still image of migrating keratinocyte with overlaid cell trajectory. Trajectory is derived from tracking cell motility during time-lapse experiments. Color denotes passage of time such that yellow is the starting position and purple denotes track end position. Cell boundary is in white. Scale bar = 100 μm. Kymographs (*right*) taken at the leading edge of migrating cells (e.g., similar to black box in the left image) are used to obtain information regarding inter-retraction duration and retraction duration. The cell protrusion quantification software, ADAPT [6] was used to gain information regarding retraction strength. Scale bar = 10 μm, Time bar = 5 min. **(B)** Cumming plots showing simulation results using the calibrated model ($^{\text{CM}}$) to predict how PIEZO1 affects normalized wound closure (*left plots*) and wound edge length (*right plots*) in simulated $\text{Control}_{\text{GoF}}$ monolayers (*dark gray*), *Piezo1*-GoF monolayers without altered coordinated directionality parameters (*white*), and *Piezo1*-GoF monolayers with coordinated directionality decreased (*green*). See Methods Section *Model parameter adjustment* for the details. **(C)** Similar to B but using simulation results from DMSO-treated monolayers (*black*), Yoda1-treated monolayers without altered coordinated directionality parameters (*white*), and Yoda1-treated monolayers with coordinated directionality decreased (*red).* **(D)** Similar to B but using simulation results from $\text{Control}_{\text{cKO}}$ monolayers (*light gray*), *Piezo1*-cKO monolayers without altered coordinated directionality parameters (*white*), and *Piezo1*-cKO monolayers with coordinated directionality increased (*purple).* In B-D, n = 100 simulation results for each condition, and $^{\text{CM}}$ denotes "Calibrated Model". To account for

Figure 3.1 continued on next page 36

LIST OF TABLES

ACKNOWLEDGMENTS

I would like to express my sincere gratitude to my advisor, Prof. John Lowengrub, for all the patience, support and guidance over the years as I explored my research from computational differential equations to mathematical biology. Thank you for teaching me so much, and for always taking the time to offer highly professional advice and help me grow as a scientist.

I also want to extend my great appreciation to Prof. Medha Pathak, my collaborator and unofficial co-advisor, for providing me such an engaging project that has kept me highly motivated to explore further, leading me into the wonderful world where mathematicians and biologists closely work together. A big thank you to all my co-authors and collaborators from the Pathak Lab who contributed to the multidisciplinary work presented within this dissertation, especially Dr. Jesse Holt. Our project would not have been nearly as successful without your excellent experiments.

Thank you to everyone in the Department of Mathematics, both professors and fellow graduate students, for all your thoughtful insights and feedback and for helping me reach this milestone. I am deeply grateful to my committee member Prof. Long Chen for his mentorship and encouragement, particularly during my early years at UC Irvine. I would also like to thank every instructor I worked with during my five years as a teaching assistant, especially Prof. Christopher Davis, who served as my teaching reference for my postdoc application.

Beyond my department, I want to extend my sincere appreciation to my mentor Dr. William Hlavacek from Los Alamos National Laboratory, who pushed me to strive for excellence during my research internship. I also thank my alumni mentor Dr. Santiago Guisasola and my career counselor Lauren Lyon for their tremendous support during my transition to the next stage of my career. My appreciation also goes to my coach Chris Stark, who trained me in Brazilian Jiu-Jitsu, helping me stay both physically and spiritually strong.

To all my friends — I appreciate you for struggling along with me, providing community and building memories. A special thank you to my fellow von Neumann laureates Dr. Ziang Long and Dr. Yang Yang for their warm support and heartfelt help at every critical turning point throughout my graduate school. I would also like to thank Dr. Dong Yan for involving me in hosting the Mathematics Graduate Student Colloquium, where I enjoyed so much fun in organizing great events with milk tea and fried chicken. My thanks also go to my friend Dr. Min-Jhe Lu for assisting my research and introducing me to his welcoming community. Shout to the other children of the Cartel de Justo Hanekawa, including but not limited to So Nakamura, Jongwon Kim, Thurman Ye and Yiyun He. The stories we have written together in my last year have made for a perfect ending to this memorable journey.

Last but the most importantly, I would like to express my deepest appreciation to my family, both present and past, for their unconditional love and support. I am thankful to have had all of you in my life, and I would not be where I am today without you.

Portions of my dissertation are reprints of material from the article "PIEZO1 regulates leader cell formation and cellular coordination during collective keratinocyte migration," published in *PLoS Computational Biology*, 2024.

Funding Acknowledgement: This work was partially supported by NIH grants R01NS109810 and DP2AT010376; NSF grant DMS-1953410; a skin seed grant through 5P30AR075047-03; a James H Gilliam Fellowship for Advanced Study (GT11549) from the Howard Hughes Medical Institute, and an Interdisciplinary Opportunity Award from the UCI NSF-Simons Center for Multiscale Cell Fate Research (funded by NSF grant DMS1763272 and a Simons Foundation grant 594598).

VITA

Jinghao Chen

EDUCATION

Doctor of Philosophy in Mathematics **2024**
University of California, Irvine *Irvine, California*

Master of Science in Mathematics **2020**
University of California, Irvine *Irvine, California*

Bachelor of Science in Mathematics **2018**
Tianjin University *Tianjin, China*

RESEARCH EXPERIENCE

Graduate Research Assistant **2019–2024**
University of California, Irvine *Irvine, California*

NSF Mathematical Sciences Graduate Intern **2023**
Los Alamos National Laboratory *Los Alamos, New Mexico*

Mitacs Globalink Research Intern **2017**
University of British Columbia *Vancouver, Canada*

TEACHING EXPERIENCE

Lecture Instructor **2023**
University of California, Irvine *Irvine, California*

Teaching Assistant **2018–2023**
University of California, Irvine *Irvine, California*

Teaching Assistant **2022**
California State Summer School for Mathematics and Science *Irvine, California*

REFEREED JOURNAL PUBLICATIONS

PIEZO1 regulates leader cell formation and cellular coordination during collective keratinocyte migration **2024**
PLoS Computational Biology

ABSTRACT OF THE DISSERTATION

Mathematical modeling of collective cell migration in wound healing

By

Jinghao Chen

Doctor of Philosophy in Mathematics

University of California, Irvine, 2024

Chancellor's Professor John S. Lowengrub, Chair

The collective migration of keratinocytes during wound healing requires both the generation and transmission of mechanical forces for individual cellular locomotion and the coordination of movement across cells. Leader cells along the wound edge transmit mechanical and biochemical cues to ensuing follower cells, ensuring their coordinated direction of migration across multiple cells. Despite the observed importance of mechanical cues in leader cell formation and in controlling coordinated directionality of cell migration, the underlying biophysical mechanisms remain elusive. The mechanically-activated ion channel PIEZO1 was recently identified to play an inhibitory role during the reepithelialization of wounds. Here, through an integrative experimental and mathematical modeling approach, we elucidate PIEZO1's contributions to collective migration. Time-lapse microscopy reveals that PIEZO1 activity inhibits leader cell formation at the wound edge. To probe the relationship between PIEZO1 activity, leader cell formation and inhibition of reepithelialization, we developed an integrative 2D continuum model of wound closure that links observations at the single cell and collective cell migration scales. Through numerical simulations and subsequent experimental validation, we found that coordinated directionality plays a key role during wound closure and is inhibited by upregulated PIEZO1 activity. We propose that PIEZO1-mediated retraction suppresses leader cell formation which inhibits coordinated directionality between cells during collective migration. We also extended the model to include two distinct cell

types, each governed by its own set of equations and parameters, interacting through cell-cell adhesion, volume-filling effects, and wound edge retraction. Simulations with various cell mixtures reveal that mutually repulsive cells promote wound closure more effectively than homogeneous populations, with the promotion level amplified by mixture heterogeneity. Additionally, simulations show that cells with higher PIEZO1 activity are generally less represented among edge cells, correlating with wound edge retraction. Through the study of this extended model, we comprehensively explored the roles of cell-cell interactions and heterogeneity in collective cell migration involving PIEZO1 mixtures.

Chapter 1

Introduction

Cell migration plays an essential role in driving a diverse range of physiological processes including embryonic morphogenesis, tissue formation, repair and regeneration [25, 26]. This multistep process of cellular locomotion relies upon the coordination between several cellular processes including: actin polymerization, exertion of actomyosin-based contractile forces, and the dynamics of adhesion complexes [73]. During single cell migration, cells migrate directionally by becoming polarized. Located at the front of polarized cells, the leading edge drives forward locomotion while the rear, or retracting region, underlies the physical translocation of the cell body [76, 77, 86]. Under many physiological contexts, cells increase their migration efficiency by migrating together as a multicellular unit. During this collective form of cell migration, cells locomote while maintaining cell-cell contacts thus enabling subpopulations of cells to move interdependently [62, 90]. In addition to each cell polarizing individually, collectively migrating populations of cells become uniformly polarized due to the communication of mechanical and biochemical information through cell-cell contacts [14, 85]. This multicellular polarization is initiated by the highly specialized leader cells which are located at the front of groups of collectively migrating cells [69]. Leader cells are located at the tip of cellular outgrowths that develop along the wound edge and these cells

are distinct from neighboring cells, as they display increased polarity and large lamellipodial protrusions [88]. Through the local coordination of intercellular mechanical forces, leader cells dictate the speed and the directional migration of individual follower cells located behind them [2, 17, 19, 20, 48, 80, 83]. Here, we use the term "coordinated directionality" to refer to how cohesively cells migrate in a direction similar to neighboring cells. This large-scale polarization and coordination of motion by leader cells is able to span across multiple cells, covering hundreds of micrometers in length [68, 69]. Thus the collective behaviors and dynamics of migrating sheets of cells are largely dependent upon the formation and dynamics of leader cells, and the transduction of guidance cues to the ensuing followers.

The collective movements of cells during epithelial sheet migration play a central role in guiding keratinocyte migration during reepithelialization, an essential component underlying the repair of wounded skin, wherein the cutaneous epidermal barrier is reinstated [44]. Recent research led by Holt *et al.* identified the mechanically activated ion channel, PIEZO1, as a key regulator of the reepithelialization process [35]. Wounds generated in skin-specific *Piezo1* knockout mice ($Krt14^{Cre};Piezo1^{fl/fl}$; hereafter *Piezo1*-cKO) were found to close faster than those in littermate Control ($\text{Control}_{\text{cKO}}$) mice. On the other hand, $Krt14^{Cre};Piezo1^{cx/+}$ and $Krt14^{Cre};Piezo1^{cx/cx}$ mice (hereafter *Piezo1*-GoF) which express a skin-specific *Piezo1* gain-of-function mutation exhibited slower wound closure relative to littermate Control ($\text{Control}_{\text{GoF}}$) mice (Fig 1.1A; [35]). Scratch wound assays performed in monolayers of keratinocytes isolated from these mice recapitulate the *in vivo* results, confirming that PIEZO1 activity inhibits keratinocyte reepithelialization (Fig 1.1B; [35]). Moreover, treatment of monolayers with Yoda1, a chemical agonist of PIEZO1, also resulted in delayed wound closure further indicating the channel's involvement in regulating wound closure (Fig 1.1B) [47, 79]. Given the different genetic backgrounds between conditions (i.e., *Piezo1*-cKO, *Piezo1*-GoF, Yoda1-treated) and the differences observed in migration properties across the Control samples of these different backgrounds [35], keratinocytes are only compared to control conditions of the same genetic background for all analyses. Through a

combined series of *in vitro* experimentation and bioimage analyses, PIEZO1 channel activity was found to increase localized cell retraction along the wound edge during *in vitro* wound closure assays, inhibiting advancement of cells and thus slowing wound closure. The finding that PIEZO1 enhances retraction provided a working mechanism for how PIEZO1 activation slows wound closure, while the absence of the channel accelerates wound closure.

Efficient collective migration is driven by the formation of leader cells [8, 29, 71]. These highly specialized cells are distinct from their surrounding follower cells and play a key role in dictating collective dynamics [88]. In a recent investigation conducted by Chen *et al.*, it was discovered that PIEZO1 activity inhibits wound edge dynamics and leader cell formation [37]. Using differential interference contrast (DIC) time-lapse imaging, the study examined the evolution of wound margins in scratch wounds generated in *Piezo1*-cKO, *Piezo1*-GoF, and Yoda1-treated keratinocyte monolayers, alongside their respective controls (Fig 1.1C-E). During reepithelialization, multicellular finger-like protrusions often form along the wound margin as cells work together to close the wound area [93]. At the front of these cellular outgrowths, leader cells can be identified by their specialized phenotypic morphology in which they display a larger size, increased polarity, and prominent lamellipodia (Figs 1.1F and A.1) [69, 71]. Leader cells were manually identified in time-lapse images of wound closure, similar to methods other groups have used for leader cell quantification within migrating collectives [72]. In *Piezo1*-cKO monolayers, the monolayer edge shows an increase in the number of leader cells compared to those from $\text{Control}_{\text{cKO}}$ keratinocyte monolayers (Figs 1.1C, 1.1G and A.1A). On the other hand in both *Piezo1*-GoF and Yoda1-treated monolayer conditions, where PIEZO1 activity is increased, the wound edge remains relatively flat throughout the imaging period due to a decrease in the formation of leader cells at the wound edge compared to respective control monolayers (Figs 1.1D, 1.1E, 1.1G, A.1B and A.1C).

To quantify the effect that PIEZO1 activity has on wound edge dynamics and leader cell protrusions, Chen *et al.* also measured the change in the length of the wound edge within

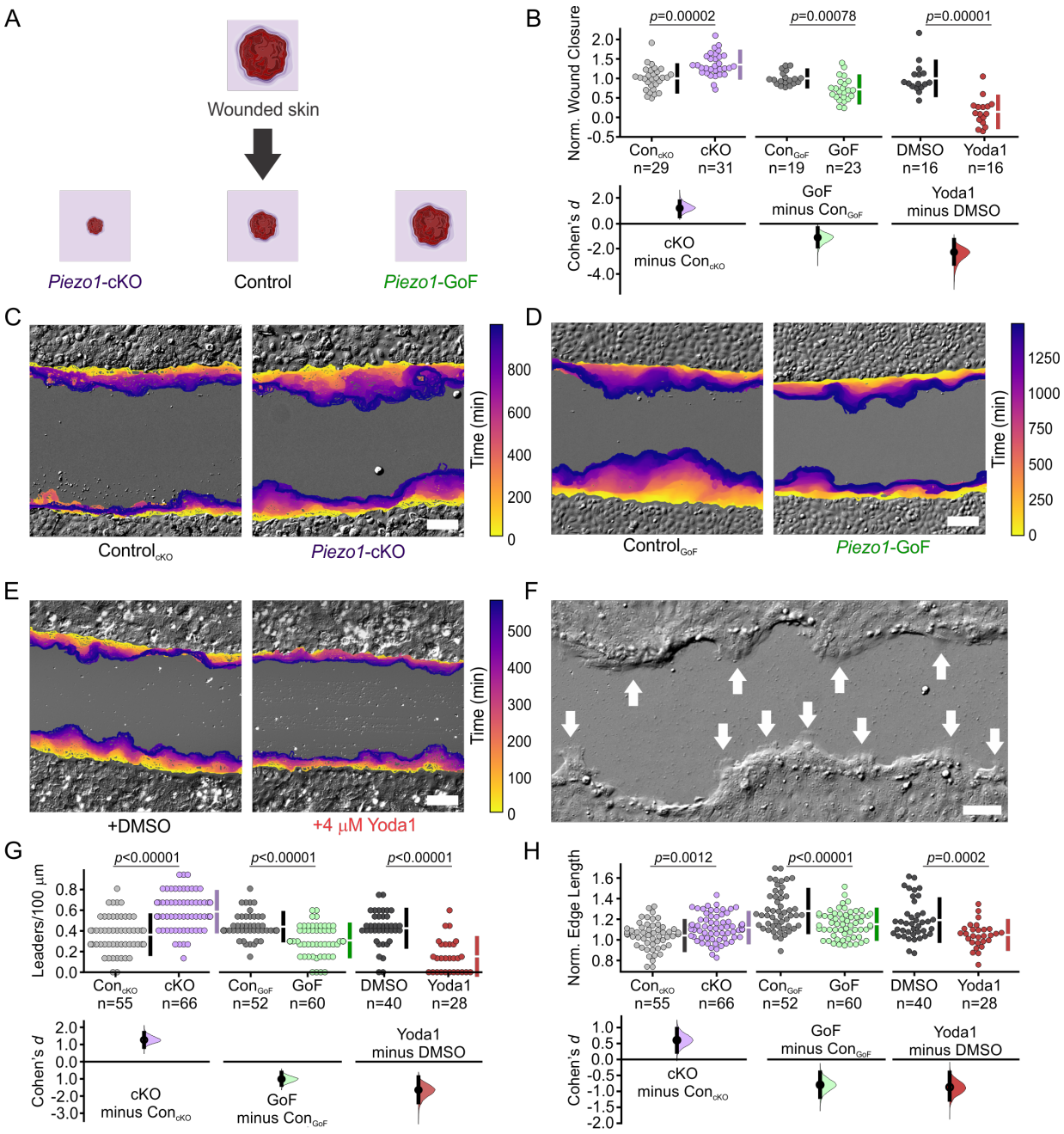

Figure 1.1: **PIEZO1 activity inhibits wound edge dynamics and leader cell formation**. **(A)** Summary schematic depicting PIEZO1's effect on keratinocyte reepithelialization reported in Holt *et al.*, 2021 [35]. **(B)** Reproduced from Fig 1L in [35] under a Creative Commons Attribution license, Cumming plot illustrating wound closure during *in vitro* scratch assays utilizing keratinocytes isolated from: $\text{Control}_{\text{cKO}}$ and *Piezo1*-cKO mice (*left*; p value calculated via two-sample t-test; Cohen's d = 1.19; images from three independent experiments), $\text{Control}_{\text{GoF}}$ and *Piezo1*-GoF mice (*middle*; p value calculated via two-sample t-test; Cohen's d = -1.13; images from four independent experiments), and DMSO-treated and 4 μM Yoda1-treated keratinocytes (*right*; p value calculated via

Figure 1.1 continued on next page

Figure 1.1 continued
Mann-Whitney test; Cohen's d = -2.28; images from three independent experiments). n in B denotes the number of unique fields of view imaged. **(C)** Representative overlay of the leading edge detected and segmented from DIC time-lapse images taken during *in vitro* scratch assay experiments in $\text{Control}_{\text{cKO}}$ (left) and *Piezo1*-cKO (right) monolayers. Color of the cell boundary outline indicates passage of time. Scale bar = 100 μm. The data in C are representative of three independent experiments. **(D)** Similar to C but for scratch assay experiments performed in $\text{Control}_{\text{GoF}}$ (*left*) and *Piezo1*-GoF (*right*) monolayers. The data in D are representative of four independent experiments. **(E)** Similar to C but for scratch assay experiments performed in DMSO-treated (*left*) and 4 μM Yoda1-treated (*right*) monolayers. The data in E are representative of three independent experiments. **(F)** Representative DIC image of wound closure during an *in vitro* scratch assay showing the appearance of finger-like protrusions led by leader cells (shown by white arrows). Scale bar = 100 μm. See also Fig A.1. **(G)** Cumming plot showing the number of leader cells per 100 μm which were manually identified from DIC time-lapse images along the wound margin in monolayers of: $\text{Control}_{\text{cKO}}$ vs. *Piezo1*-cKO keratinocytes (*left*; p value calculated via two-sided permutation t-test; Cohen's d = 1.26), $\text{Control}_{\text{GoF}}$ vs. *Piezo1*-GoF keratinocytes (*middle*; p value calculated via Mann Whitney test; Cohen's d = -1), DMSO-treated vs. 4 μM Yoda1-treated keratinocytes (*right*; p value calculated via Mann Whitney test; Cohen's d = -1.65). **(H)** Cumming plot showing quantification of the normalized edge length in monolayers of: $\text{Control}_{\text{cKO}}$ vs. *Piezo1*-cKO keratinocytes (*left*; p value calculated via two-sided permutation t-test; Cohen's d= 0.6), $\text{Control}_{\text{GoF}}$ vs. *Piezo1*-GoF keratinocytes (*middle*; p value calculated via two-sided permutation t-test; Cohen's d= -0.8), DMSO-treated vs. 4 μM Yoda1-treated keratinocytes (*right*; p value calculated via two-sided permutation t-test; Cohen's d= -0.9). To account for differences in the starting edge length which might occur when scratching monolayers in H, data are normalized by dividing the scratch length at either the end of the imaging period, or at the moment the wound edges touch, by the starting scratch length. A higher normalized edge length indicates a more featured wound edge, corresponding to the presence of more leader cells. n in G & H denotes the number of monolayer sheets imaged. See also Table 3.2.

a field of view over the course of the imaging period [37], similar to methods employed by other groups [50]. The presence of leader cells, which are located at the front of cellular outgrowths, increases the length of the wound edge. Therefore, a shorter wound edge length would indicate fewer leader cells while a longer wound edge would indicate an increase in leader cells along the wound margin. It was found that *Piezo1*-cKO monolayers have a longer wound edge length relative to $\text{Control}_{\text{cKO}}$ monolayers, which further supports the observation that the absence of PIEZO1 results in increased leader cells along the wound edge (Fig 1.1H, *left*). Conversely, in both *Piezo1*-GoF and Yoda1-treated monolayers it was discovered that edge lengths are significantly shorter than the respective control monolayers (Fig 1.1H, *middle*, *right*). Thus, PIEZO1 inhibits the formation of leader cells, resulting in a shorter and flatter wound edge, while the absence of the channel results in a longer and more featured wound edge due to an increase in leader cell protrusions.

Mathematical modeling has emerged as a powerful technique to systematically probe how biological factors contribute to the complex orchestration of collective migration [3, 5, 10, 81]. Here, we build upon these previous works and develop a novel two-dimensional continuum model of reepithelialization. This model is derived by upscaling from a discrete model, incorporating key factors such as cell motility, retraction, cell-cell adhesion, and coordinated directionality. While motility and retraction are determined by single cell behaviors, cell-cell adhesion and coordinated directionality are influenced by the presence of neighboring cells. An upscaling procedure enables us to identify the contributions of these components to cell migration at the monolayer scale. We calibrated the cell-scale parameters in the model using data from experiments on single cells and performed parameter studies to investigate the influence of cell-cell adhesion and coordinated directionality, which are harder to measure experimentally. Our numerical simulations revealed that coordinated directionality is a critical factor in recapitulating the influence of PIEZO1 on wound closure and that elevated PIEZO1 activity leads to the inhibition of coordinated directionality. These predictions of the model were experimentally validated. Experiments also revealed that PIEZO1 activity

suppresses the formation of leader cells, contributing further to the inhibition of collective migration during keratinocyte reepithelialization.

By extending the mathematical model with the upscaled framework, we construct a new framework for studying collective cell migration during wound healing, focusing on scenarios where two PIEZO1 genotypes are present. Each cell type is governed by its own set of equations with unique parameters while interacting through cell-cell adhesion, volume-filling effects, and wound edge retraction. Building on the parameters inherited from the previous upscaled model, this new model emphasizes the interactions between the different cell types and the heterogeneity of their mixtures. Through simulations with various combinations of cell mixtures, we observe that mutually repelling cells can promote wound closure more effectively than a homogeneous population of a single cell type. Moreover, the level of promotion is positively correlated with the heterogeneity of the mixture. Near the wound edge, simulations show that higher PIEZO1 activity correlates with a lower representation of edge cells. By enforcing additional model assumptions, we find that cells with higher PIEZO1 activity are more likely to be found among the backward edge cells compared to the forward edge cells, suggesting that PIEZO1 activity promotes wound edge retraction. This observation aligns with prior experimental findings that link wound edge retraction to PIEZO1 enrichment [35]. Furthermore, using this extended model, we explore parameter inference by integrating appropriate experimental data. This approach enhances our understanding of the dynamic interactions and provides deeper insights into the roles of PIEZO1 activity and cell heterogeneity in the wound healing process.

This dissertation is organized as follows. Chapter 2 provides a mathematical model of collective cell migration with an upscaled framework, along with an alternative fully continuum model, designed to study the role of PIEZO1 in wound healing. Chapter 3 details the use of this model to derive predictions and subsequent experimental validation. Chapters 2 and 3 are based on a published research article coauthored with Jesse Holt, Elizabeth Evans, John

Lowengrub, and Medha Pathak. Chapter 4 extends the model presented in Chapter 2 to study collective cell migration involving two cell types with distinct PIEZO1 activity, which is part of a paper in preparation with Medha Pathak and John Lowengrub. Appendix A includes supplementary materials for Chapters 2 and 3, Appendix B includes supplementary materials for Chapter 4, and Appendix C summarizes experimental methods and materials.

Chapter 2

Modeling PIEZO1's influence on keratinocyte collective dynamics

2.1 Introduction

To address the complexities inherent in the biological phenomena of collective cell migration, we adopted a theoretical approach to characterize the biophysical relationship between PIEZO1 activity, leader cell initiation, and wound closure. By designing a mathematical model of keratinocyte reepithelialization, we aimed to study how PIEZO1 activity influences this critical healing process. We first separated reepithelialization into essential phenomenological components which could be incorporated into the design of the model as manipulable variables. As such we accounted for cell motility, and cellular retraction, a process central to the migration process and one which is promoted by PIEZO1 activity [35].

In our experimental data, we found that retraction varied in intensity such that in some instances it led to small regions of individual cells retracting while in other cases it led to the entire cell body pulling back away from the wound area [35]. Therefore we modeled

retraction as a stochastic process at the leading edge associated with backward cell motion. We incorporated into our model design: (1) the average duration of retraction events at the monolayer edge, (2) the interval of time between sequential edge retractions, and (3) the strength of retraction. We also incorporated two hallmarks of collective cell migration: cell-cell adhesion and the coordination of keratinocyte migration direction, or coordinated directionality, both of which have been central to mathematical models proposed by other groups [40, 81, 33, 45]. Instead of modeling the mechanical forces involved in adhesion and retraction explicitly, we encoded the mechanistic effects such as cell motility, coordinated directionality, cell-cell adhesion, and retraction into model parameters. We then systematically manipulate these biological components of wound closure within our models and compare simulation results to experimental data garnered from scratch assays of PIEZO1 mutant keratinocytes (Table 3.2).

Due to the inherent multivariate nature of our system, we utilized a partial differential equation (PDE) model to describe the spatiotemporal effects of PIEZO1 on reepithelialization. The PDE governing collective cell migration, which captures behavior at the monolayer scale, is derived by upscaling a discrete model from the single-cell level. This upscaled model, introduced in Section 2.2.1, is our primary tool for studying PIEZO1's role in regulating wound closure. Additionally, a fully continuum model, built directly on a PDE, is presented as an alternative approach to reaffirm the results obtained from the upscaled model, as detailed in Section 2.2.2.

We present a dimensionless version of our models here. We rescale the cell density by its maximal value, which can be quantified by counting the maximum number of cells in squares of a grid in the monolayer region away from the wound edge, where we expect cell density to exhibit spatial and temporal uniformity. The characteristic length scale l is defined as the distance from the wound edge to the region where the cells reach the maximal density in the monolayer (typically $\sim$10 cell lengths). Hence, our computational domain is a small region

around the wound edge. From the experimental data, we can extract a characteristic wound edge velocity v, which allows us to derive a characteristic time $\lambda^{-1} = l/v$. See Section 2.3.6 for additional details.

2.2 Model frameworks

2.2.1 From discrete to continuum: an upscaled model

The two-dimensional spatial discretization of a field of view containing a monolayer covered by a uniform grid of size h allows the labeling of indices (i, j) in space as $\boldsymbol{x} = \boldsymbol{x}_{i,j} = (ih, jh)$, and cell density, $\rho = \rho(\boldsymbol{x}, t) = \rho(x, y, t)$, a function of space, $\boldsymbol{x} = (x, y)^T$, and time, t, can be represented by $\rho_{i,j} = \rho(\boldsymbol{x}_{i,j}, t)$ at time t (Fig 2.1A). The dimensionless experimental field of view is a unit square domain: $[0, 1] \times [0, 1] \in \mathbb{R}^2$ (see Section 2.3.6 for the details of nondimensionalization). By incorporating the essential biological components of reepithelialization (Table 3.2, *bottom*), we construct the following discrete master equation (Fig 2.1A, *left*; Eq. 2.1), which demonstrates the change rate of cell density over time (Eq. 2.1; left hand side) in response to the net flux of cells (Eq. 2.1; right hand side):

$$\begin{aligned}\frac{\partial \rho_{i,j}}{\partial t} =& T^{\rightarrow}_{i-1,j}\rho_{i-1,j} + T^{\leftarrow}_{i+1,j}\rho_{i+1,j} + T^{\uparrow}_{i,j-1}\rho_{i,j-1} + T^{\downarrow}_{i,j+1}\rho_{i,j+1} \\ & - (T^{\rightarrow}_{i,j} + T^{\leftarrow}_{i,j} + T^{\uparrow}_{i,j} + T^{\downarrow}_{i,j}) \cdot \rho_{i,j}.\end{aligned} \tag{2.1}$$

Here, the T's are transitional probabilities per unit time associated with given directions of movement (i.e., $T^{\rightarrow}_{i,j}$, $T^{\leftarrow}_{i,j}$, $T^{\uparrow}_{i,j}$ and $T^{\downarrow}_{i,j}$) for cells migrating between adjacent grid points (e.g., from $\boldsymbol{x}_{i,j}$ to $\boldsymbol{x}_{i+1,j}$ for $T^{\rightarrow}_{i,j}$). Each transitional probability accounts for cell motility, cell-cell adhesion, coordinated directionality, retraction events, and volume filling limitations.

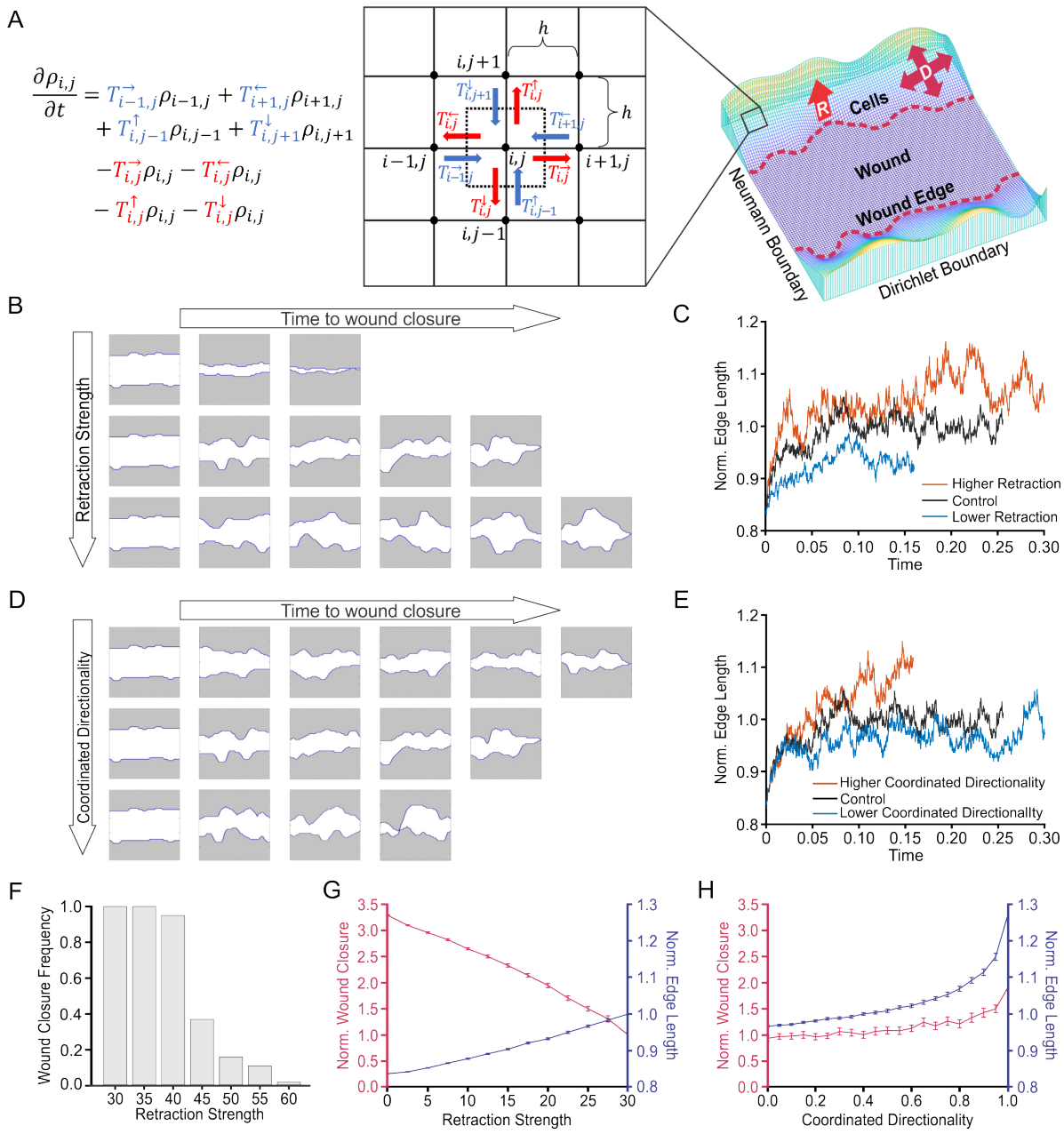

Figure 2.1: **Coordinated directionality is the key model parameter which replicates PIEZO1 reepithelialization phenotypes.** **(A)** Schematic showing a simplified visual of the modeling approach and visualization of the simulation domain. In the semi-discrete master equation (*left*; Eq. 2.1), transitional probabilities associated with cell influx are highlighted in blue, while cell efflux related transitional probabilities are in red. Corresponding arrows depict this process on the grid (*middle*), indicating that the net flux is equal to the change in cell density over time at grid point (i, j). $\boldsymbol{D}$ represents coordinated directionality, and $\boldsymbol{R}$ represents retraction. **(B)** Simulation snapshots taken at equidistant time intervals depicting the evolution of the wound edge until wound closure (the moment interfaces touched) under low (*top*), Control (*middle*) and increased (*bottom*) levels of

Figure 2.1 continued on next page

Figure 2.1 continued
retraction strength. Shaded areas represent cell monolayers, while unshaded areas denote the cell-free space. **(C)** Plots showing quantification of the normalized edge length of simulated wounds, a measurement indicative of the number of leader cells, under different levels of retraction strength as a function of time. Shorter lines indicate simulation ending earlier due to faster wound closure. **(D, E)** Same as for (B) and (C), but under different levels of coordinated directionality. **(F)** The proportion of wound closure cases under different retraction magnitudes. The proportion of open wound closure cases start to decline after increasing retraction strength to 40, and almost no closure cases occur as retraction strength approaches 60. See also Fig A.2. **(G)** Line graphs showing the mean of 100 simulation results depicting the effect of retraction strength on normalized wound closure (*red; left axes*) and normalized edge length (*blue; right axes*). Error bars depict the standard error of mean. **(H)** Similar to (G) but for coordinated directionality. In C, E, F-H, all numbers have no unit because the model is dimensionless. See also Fig A.3 and Table 3.2.

In the discrete master equation (Eq. 2.1), $T_{i,j}^{\rightarrow}$ the transitional probability for cells traveling from $\boldsymbol{x}_{i,j}$ to $\boldsymbol{x}_{i+1,j}$ is defined as the following:

$$T_{i,j}^{\rightarrow} = (1-\rho_{i+1,j})(1-\alpha\rho_{i-1,j})(1-\alpha\rho_{i,j+1})(1-\alpha\rho_{i,j-1})(f_{i,j}^{\rightarrow} + b_{i,j}^{\rightarrow}). \tag{2.2}$$

The term $(1-\rho_{i+1,j})$ models the effects of volume filling, e.g., if the cell density at $\boldsymbol{x}_{i+1,j}$ has reached its maximal value, it restricts further cell movement into that point. The term $(1-\alpha\rho_{i-1,j})(1-\alpha\rho_{i,j+1})(1-\alpha\rho_{i,j-1})$ models cell-cell adhesion from three directions that hinder the cell migration, where $\alpha \in [0,1]$ is the adhesion coefficient, which is assumed to be the same in each direction [3]. In the last term $f_{i,j}^{\rightarrow} + b_{i,j}^{\rightarrow}$, the vector $f_{i,j}^{\rightarrow} = d^{\leftrightarrow}\rho_{i,j}/h^2$ models diffusive cell motion while $b_{i,j}^{\rightarrow} = r_{i,j}^{\rightarrow}/h$ models cell movement due to retraction. The dependence on h reflects diffusive ($\mathcal{O}(1/h^2)$) and advective ($\mathcal{O}(1/h)$) scaling of the equations, respectively. The diffusive component $f_{i,j}^{\rightarrow}$, scaled as $\mathcal{O}(1/h^2)$, generates a diffusion flux that depends on the gradient of cell density. The advective component $b_{i,j}^{\rightarrow}$, scaled as $\mathcal{O}(1/h)$, results in an advection velocity independent of cell density that mimics the influence of retraction events (see Section 2.3.4 for details). Further, $d^{\leftrightarrow}$ represents the magnitude of

movement in the horizontal coordinate direction, while $r_{i,j}^{\rightarrow}$ accounts for cell retraction. Note that the cell density term $\rho_{i,j}$ in $f_{i,j}^{\rightarrow}$ models the moving front that connects a region of zero cell density (wound) with a region of non-zero density (monolayer), e.g., [91]. The other transitional probabilities, $T_{i,j}^{\leftarrow}$, $T_{i,j}^{\uparrow}$ and $T_{i,j}^{\downarrow}$ are defined analogously. Hence, Eq. 2.2 can be rewritten as

$$\begin{aligned} T_{i,j}^{\rightarrow} =& \frac{(1-\rho_{i+1,j})(1-\alpha\rho_{i-1,j})(1-\alpha\rho_{i,j+1})(1-\alpha\rho_{i,j-1})d^{\leftrightarrow}\rho_{i,j}}{h^2} \\ &+ \frac{(1-\rho_{i+1,j})(1-\alpha\rho_{i-1,j})(1-\alpha\rho_{i,j+1})(1-\alpha\rho_{i,j-1})r_{i,j}^{\rightarrow}}{h}. \end{aligned} \tag{2.3}$$

A continuum limit can be obtained by taking $h \to 0$ in the discrete master equation (Eq. 2.1) to yield the partial differential equation

$$\frac{\partial \rho}{\partial t} = \nabla \cdot (\boldsymbol{D}\nabla\rho + \boldsymbol{R}\rho) \tag{2.4}$$

which is a diffusion-advection equation where the diffusion, $\boldsymbol{D}$, models cellular locomotion and coordinated directionality, whereas the advection velocity, $\boldsymbol{R}$, models retraction of the leading edge. The diffusion coefficient, or diffusivity, $\boldsymbol{D}$, is a 2×2 positive definite matrix given by

$$\boldsymbol{D} = d \cdot (w_I \boldsymbol{I} + w_A \boldsymbol{A}) \cdot \hat{D}_\alpha(\rho) \tag{2.5}$$

where $d > 0$ models cell motility during collective migration. The diffusion decomposition

$w_I \boldsymbol{I} + w_A \boldsymbol{A}$ combines the diffusion isotropy, where the identity matrix $\boldsymbol{I} = \boldsymbol{I}_2$ models the randomness of cellular migration, and diffusion anisotropy, where the matrix $\boldsymbol{A}$ models directed cellular migration. During wound closure, directional cues received from leader cells promote the migration of followers into the cell-free space to close the wound, thus promoting cells to have a higher probability of moving into the wound area and resulting in an anisotropic direction of diffusion.

The information regarding coordinated directionality is transmitted from the discrete level through the incorporation of distinct magnitudes of movement in the coordinate directions ($d^{\leftrightarrow}$ and $d^{\updownarrow}$ in Eq. 2.2, 2.3) that influence the transitional probabilities in two directions. Considering that cells receive signals to migrate towards the wound gap, we assume a larger magnitude of movement in the vertical direction ($d^{\updownarrow} \geq d^{\leftrightarrow}$) based on our experimental configuration (Fig 2.1A, *right*). This assumption facilitates the following decomposition:

$$
\begin{aligned}
\begin{pmatrix} d^{\leftrightarrow} & 0 \\ 0 & d^{\updownarrow} \end{pmatrix} &= d^{\updownarrow} \cdot \begin{pmatrix} \frac{d^{\leftrightarrow}}{d^{\updownarrow}} & 0 \\ 0 & 1 \end{pmatrix} = d^{\updownarrow} \cdot \begin{pmatrix} \frac{d^{\leftrightarrow}}{d^{\updownarrow}} & 0 \\ 0 & \frac{d^{\leftrightarrow}}{d^{\updownarrow}} + \frac{d^{\updownarrow} - d^{\leftrightarrow}}{d^{\updownarrow}} \end{pmatrix} \\
&= d^{\updownarrow} \cdot \left(\begin{pmatrix} \frac{d^{\leftrightarrow}}{d^{\updownarrow}} & 0 \\ 0 & \frac{d^{\leftrightarrow}}{d^{\updownarrow}} \end{pmatrix} + \begin{pmatrix} 0 & 0 \\ 0 & \frac{d^{\updownarrow} - d^{\leftrightarrow}}{d^{\updownarrow}} \end{pmatrix} \right) \\
&= d^{\updownarrow} \cdot \left(\frac{d^{\leftrightarrow}}{d^{\updownarrow}} \cdot \begin{pmatrix} 1 & 0 \\ 0 & 1 \end{pmatrix} + \frac{d^{\updownarrow} - d^{\leftrightarrow}}{d^{\updownarrow}} \cdot \begin{pmatrix} 0 & 0 \\ 0 & 1 \end{pmatrix} \right) \\
&= d \cdot (w_I \boldsymbol{I} + w_A \boldsymbol{A})
\end{aligned}
\tag{2.6}
$$

where the continuous coefficients of cell motility d, isotropic strength w_I, and anisotropic strength w_A (representing coordinated directionality) are derived from the discrete coefficients of the magnitudes of movement in the coordinate directions $d^{\leftrightarrow}$ and $d^{\updownarrow}$ through the following relation:

$$
\begin{aligned}
d &= d^{\updownarrow}, \\
w_I &= \frac{d^{\leftrightarrow}}{d^{\updownarrow}}, \\
w_A &= \frac{d^{\updownarrow} - d^{\leftrightarrow}}{d^{\updownarrow}}.
\end{aligned}
\tag{2.7}
$$

Here, the directionality assumption $d^{\updownarrow} \geq d^{\leftrightarrow}$ guarantees the weights w_I and w_A are non-negative and bounded by 1, and the convex weighting relation $w_I + w_A = 1$ naturally holds from the derivation of w_I and w_A. From these relations, we can observe how w_A measures coordinated directionality. Systems with stronger coordinated directionality, e.g., larger w_A that results from large relative differences between between $d^{\updownarrow}$ and $d^{\leftrightarrow}$, are more likely to migrate towards the direction of closure.

The scalar diffusion coefficient $\hat{D}_\alpha(\rho)$ in Eq. 2.5 is a polynomial of cell density ρ:

$$
\hat{D}_\alpha(\rho) = 2\rho - (1 + 11\alpha)\rho^2 + (8\alpha + 16\alpha^2)\rho^3 - (13\alpha^2 + 7\alpha^3)\rho^4 + 6\alpha^3\rho^5, \tag{2.8}
$$

which is derived through a multi-scale modeling process from the scaled cell density $\rho_{i,j}/h^2$, cell-cell adhesion (e.g., $(1 - \alpha\rho_{i-1,j})(1 - \alpha\rho_{i,j+1})(1 - \alpha\rho_{i,j-1})$ in $T^{\rightarrow}_{i,j}$) and volume filling (e.g., $1 - \rho_{i+1,j}$ in $T^{\rightarrow}_{i,j}$). The adhesion coefficient, α, which lies in the range $[0, 1]$, models the adhesion forces between adjacent cells, with a larger α corresponding to larger adhesion forces. Volume-filling limitations to cell movement are also modeled in $\hat{D}_\alpha(\rho)$ to hinder cells from migrating into a cell-dense area. In order to maintain a positive diffusivity, the value of α is bounded by ~ 0.66 from above (see the detailed derivation in Section 2.3.3).

Analogous to the derivation of diffusion, retraction, $\boldsymbol{R}$ (Fig 2.1A, *right*), is derived from

the $\mathcal{O}(1/h)$ component of the discrete transitional probability (Eq. 2.3) by taking the limit $h \to 0$:

$$\boldsymbol{R} = (1-\rho)(1-\alpha\rho)^3 \cdot (\Delta r^{\leftrightarrow}, \Delta r^{\updownarrow})^T \in \mathbb{R}^2 \tag{2.9}$$

where $1-\rho$ and $(1-\alpha\rho)^3$ model the effects of volume filling and cell-cell adhesion respectively. The retraction magnitude and directions are modeled phenomenologically in $\Delta r^{\leftrightarrow}$ and $\Delta r^{\updownarrow}$ as being localized in space and time, motivated by prior studies [35]. In particular, we assume:

1. Retraction occurs locally along the wound edge. This means only a part of wound edge cells are involved in retraction events at each time, while the rest of the cells on the edge and cells within the monolayer away from the edge just migrate by diffusion.

2. Retraction occurs intermittently in time. This means no retraction event is endless, i.e., no regions retract indefinitely. Hence at a wound edge point, there is a finite interval of duration time for each retraction event, and there is also a finite interval of time between two consecutive retraction events.

Because the computational domain is a small region around the wound edge ($\sim$10 cell lengths, see Section 2.3.6), we assume there is one localized retraction region of fixed width that occurs at random times and locations on each side of the wound edge.

Following the localization assumptions (1) and (2), a choice for $\Delta r^{\leftrightarrow}$ and $\Delta r^{\updownarrow}$ is

$$\Delta r^{\leftrightarrow} = \Delta r^{\updownarrow} = \tilde{H}(\gamma - \rho) \cdot \sum_{i=1}^{\infty} s_i \cdot \tilde{\mathbb{1}}_{[\tau_i, \tau_i + \mathcal{T}_i^r)}(t) \cdot \tilde{\mathbb{1}}_{\Omega_i}(\boldsymbol{x}), \tag{2.10}$$

where H is a Heaviside function

$$H(\gamma - \rho) = \begin{cases} 1 & , \rho < \gamma \\ 0 & , \rho \geq \gamma \end{cases} \tag{2.11}$$

with threshold γ, which localizes the retraction to the wound edge ($\gamma = 0.4$ was adapted in the simulation). In particular, $H(\gamma - \rho) = 0$ turns off the retraction for $\rho > \gamma$, which is the high cell density region far away from the wound edge, while $H(\gamma - \rho) = 1$ turns on the retraction for $\rho < \gamma$, which is the low cell density region near the wound edge.

By labeling retraction events in chronological order with positive integers $i = 1, 2, 3, ...$, indicator functions $\mathbb{1}_{[\tau_i, \tau_i + \mathcal{T}_i^r)}(t)$ and $\mathbb{1}_{\Omega_i}(\boldsymbol{x})$ localize the regions where the edge retracts in time and space, respectively. We take the retraction to be localized in a region $\Omega_i := [c_i - \omega_r/2, c_i + \omega_r/2] \times [0, 1]$ about a line segment $x = c_i$ with width ω_r ($\omega_r = 0.2$ was used in the simulation):

$$\mathbb{1}_{\Omega_i}(\boldsymbol{x}) = \mathbb{1}_{[c_i - \omega_r/2, c_i + \omega_r/2]}(x) = \begin{cases} 1 & , |x - c_i| \leq \omega_r/2 \\ 0 & , \text{otherwise} \end{cases} \tag{2.12}$$

where we account for randomness by taking the uniform distribution $c_i \sim \mathcal{U}(0, 1)$. This allows the region Ω_i to randomly slide around $[0, 1]$ to localize the retraction events.

The retractions are assumed to occur at particular times τ_i with durations $\mathcal{T}_i^r$. Accordingly, we take

$$s_i \cdot \mathbb{1}_{[\tau_i, \tau_i + \mathcal{T}_i^r)}(t) = \begin{cases} s_i & , \tau_i \leq t < \tau_i + \mathcal{T}_i^r \\ 0 & , \text{otherwise} \end{cases} \tag{2.13}$$

where s_i is the speed (or strength) of the retraction, and the next retraction occurs at $\tau_{i+1} = \tau_i + \mathcal{T}_i^r + \mathcal{T}_i^{nr}$ where $\mathcal{T}_i^{nr}$ is the inter-retraction duration. To account for randomness, we assume:

$$\mathcal{T}_i^r \overset{iid}{\sim} \mathcal{N}(\mu_r, \sigma_r^2) \quad \perp\!\!\!\perp \quad \mathcal{T}_i^{nr} \overset{iid}{\sim} \mathcal{N}(\mu_{nr}, \sigma_{nr}^2) \quad \perp\!\!\!\perp \quad s_i \overset{iid}{\sim} \mathcal{N}(\mu_s, \sigma_s^2) \tag{2.14}$$

where $\mathcal{N}(\mu, \sigma^2)$ denotes the normal distribution with mean μ and standard deviation σ, and all random variables are independent and identically distributed (*iid*). Thus, the mean strength of the retraction forces is μ_s and a single retraction event is sustained for a random duration with mean μ_r. Any subsequent retraction will only start after a random idle duration with mean μ_{nr}. The corresponding variances are σ_s^2, σ_r^2, and σ_{nr}^2, respectively. To ensure that our model incorporates only physically meaningful events, any negative duration or strength values that arise during the simulation are promptly discarded.

In summary, $\Delta r^{\leftrightarrow}$ and $\Delta r^{\updownarrow}$ are designed to model retractions such that cell movement would be governed by a diffusion-advection equation that guides the migrating cells in the retraction region near the wound edge:

$$\frac{\partial \rho}{\partial t} = \nabla \cdot (\boldsymbol{D} \nabla \rho) + \nabla \cdot (\boldsymbol{s}(1-\rho)(1-\alpha\rho)^3 \rho) \quad \text{near wound edge} \tag{2.15}$$

where $\boldsymbol{D}$ is the diffusivity (Eq. 2.5) and $\boldsymbol{s} = (s, s)^T/\sqrt{2}$ where the retraction strength, s, regulates the magnitude of advection velocity. On the other hand, cells far from the wound edge (e.g., interior of the monolayer) migrate following a simple diffusion equation

$$\frac{\partial \rho}{\partial t} = \nabla \cdot (\boldsymbol{D} \nabla \rho) \quad \text{away from wound edge} \tag{2.16}$$

with the same diffusivity (Eq. 2.5). In fact, our model passes retraction information from the discrete to the continuous level. For example, if $r_{i,j}^{\leftarrow} = r_{i,j}^{\rightarrow} = \bar{r}$ then there is no retraction at $x_{i,j}$, e.g., monolayer region far away behind the wound edge. In this case, the governing equation is a pure diffusion equation without advection (Eq. 2.16) since $\Delta r^{\leftrightarrow} = r^{\leftarrow} - r^{\rightarrow} = 0$, which appears in the continuum limit. In the retraction region, $r_{i,j}^{\leftarrow}$ increases and $r_{i,j}^{\rightarrow}$ decreases, so $\Delta r^{\leftrightarrow} = r^{\leftarrow} - r^{\rightarrow} \neq 0$ and the governing equation turns into a diffusion-advection equation (Eq. 2.15).

Note that both Heaviside function $H(\gamma - \rho)$ and characteristic functions $\mathbb{1}_{[\tau_i, \tau_i + \mathcal{T}_i^r)}(t)$ and $\mathbb{1}_{\Omega_i}(\boldsymbol{x})$ are discontinuous. To preserve differentiability, we smooth H using a hyperbolic tangent function $\tilde{H}$ (Eq. 2.28 in Section 2.3.5) and smooth $\mathbb{1}_{[\tau_i, \tau_i + \mathcal{T}_i^r)}(t)$ and $\mathbb{1}_{\Omega_i}(\boldsymbol{x})$ using generalized bell-shaped functions $\tilde{\mathbb{1}}_{[\tau_i, \tau_i + \mathcal{T}_i^r)}(t)$ and $\tilde{\mathbb{1}}_{\Omega_i}(\boldsymbol{x})$ (Eq. 2.29 in Section 2.3.5). In addition to the definition of $\Delta r^{\leftrightarrow}$ and $\Delta r^{\updownarrow}$ (Eq. 2.10) given above, there are alternative choices that can be adapted to interpolate the advection velocity between the retraction and non-retraction regions. However, the qualitative results of the model are not sensitive to the choice of $\Delta r^{\leftrightarrow}$ and $\Delta r^{\updownarrow}$ under assumptions (1) and (2) and the model reduces to Eq. 2.15

near the wound edge and to Eq. 2.16 far from the wound edge.

Since we only model a subset of the observation domain in the experiment, e.g., the region close to the wound edges as opposed to the whole experimental domain, we impose the following conditions at the boundaries of the computational domain:

$$\begin{aligned} \rho(x,0,t) = g_0(x,t), \quad \rho(x,1,t) = g_1(x,t), \\ \frac{\partial \rho(0,y,t)}{\partial x} = \frac{\partial \rho(1,y,t)}{\partial x} = 0. \end{aligned} \tag{2.17}$$

Horizontally on the top and bottom of the domain, time-dependent Dirichlet boundary conditions at $\boldsymbol{x} = (x, 0)$ and $\boldsymbol{x} = (x, 1)$ assign cell densities to the boundary points by functions g_0 and g_1, which mimic the effect of cells that flow into the observation domain area from the monolayer roughly perpendicular to the wound edge. The functions g_0 and g_1 are random functions of space and time (See Section 2.3.1 for the definitions of g_0 and g_1). Whilst vertically on the left and right sides of the domain, no-flux (Neumann) boundary conditions are used to approximate a net balance of cell influx and efflux into the observation domain roughly parallel to the wound edge, as suggested by the experiments.

The initial condition is generated by solving the PDE without retraction events for a short time period, which produces a banded heterogeneous monolayer with a cell-free region in the middle mimicking the initial wound (see Section 2.3.2 for details).

Summarizing, the model depends on the following biological parameters: (1) the mean retraction duration, μ_r, (2) the mean inter-retraction duration, μ_{nr}, (3) the mean retraction strength, μ_s, (4) cell motility, d, in the absence of retraction (pure diffusion context), (5) cell-cell adhesion, α, and (6) the strength of coordinated directionality, w_A. The governing equation (Eq. 2.4) is a nonlinear stochastic PDE, where stochasticity arises from the random

coefficients. We solve the equations numerically using a finite difference method to obtain the cell density $\rho(\boldsymbol{x}, t)$ on the simulation domain over time until wound closure. Multiple simulations are performed under each condition to quantify the variability for the subsequent data analysis (See Methods Section *Numerical scheme* for details), from which we investigate how each model parameter influences collective migration during reepithelialization.

2.2.2 Alternative approach: a fully continuum model

Recall that our model was initially formulated at the discrete level and subsequently upscaled into a continuous PDE. Alternatively, we also present a phenomenological continuum model in which cell-cell adhesion is postulated at the continuum level rather than being obtained by upscaling.

In this new model, the governing equation is still a diffusion-advection equation in the same form as Eq. 2.4, but the hindering effect of cell-cell adhesion on collective migration is modeled by reducing the overall diffusion coefficient as adhesion increases, which is consistent with the approach used by Amereh *et al.* in [1]. While still accounting for coordinated directionality, volume filling effects and the advancing front connecting the wound and the monolayer, the diffusion coefficient in this new continuum model can be specifically expressed as

$$\boldsymbol{D} = d \cdot (w_I \boldsymbol{I} + w_A \boldsymbol{A}) \cdot \hat{D}(\rho), \tag{2.18}$$

where the overall structure mirrors the diffusion coefficient in our original model (Eq. 2.5). However, the scalar diffusion coefficient, denoted as $\hat{D}(\rho)$, becomes a quadratic polynomial of cell density without depending on any additional parameters:

$$\hat{D}(\rho) = 2\rho - \rho^2. \tag{2.19}$$

Compared with the original model, d in Eq. 2.18 now contains the combined effects of cell motility and cell-cell adhesion.

Analogously, we assume that the advection velocity would now model the combined effects of retraction strength and cell-cell adhesion. In particular, the advection term in Eq. 2.4 now becomes

$$\boldsymbol{R} = (1-\rho)\cdot(\Delta r^{\leftrightarrow}, \Delta r^{\updownarrow})^T \tag{2.20}$$

where $\Delta r^{\leftrightarrow}$ and $\Delta r^{\updownarrow}$ are defined in the same way as in Eq. 2.10 but incorporating the combined effects of retraction strength and cell-cell adhesion.

This fully continuum model serves as an alternative framework, primarily designed to test the robustness of the model predictions by examining the sensitivity of the results to different modeling approaches (detailed in Section 3.4.1). Henceforth, unless otherwise specified, the term "model" refers to our primary upscaled model (described in Section 2.2.1) without ambiguity.

2.3 Model components

2.3.1 Boundary conditions of governing equation

On the Dirichlet boundaries $y = 0$ and $y = 1$ (Eq. 2.17), the cell density is determined by functions $g_1(x,t)$ and $g_2(x,t)$ which are continuous on $[0,1]\times[0,+\infty)$. Since both of these are randomly generated from the same approach, without loss of generality, let's say $g(x,t)$. Covering $[0,1]\times[0,+\infty)$ with a grid, taking mesh sizes h_x and h_t and labeling grid nodes $(x,t) = (x_i, t_j) = (ih_x, jh_t)$ by indices (i,j), the function values at grid points $g_{i,j} = g(x_i, t_j)$ are taken to follow a normal distribution

$$g_{i,j} \overset{iid}{\sim} \mathcal{N}(\mu_0, \sigma_0^2) \tag{2.21}$$

with mean μ_0 and standard deviation σ_0 ($\mu_0 = 0.6$ and $\sigma_0 = 0.3$ were adapted in the simulation). This models the variability of the influx of cells from the monolayer moving into the wound region. Thereafter, the function $g(x,t)$ is given by an interpolation on $g_{i,j}$. Specifically, the boundary conditions on $y = 0$ and $y = 1$ are classical Dirichlet boundary conditions with a constant influx μ_0 if σ_0 is set to be 0.

2.3.2 Initial condition of governing equation

Assume $u(x,y,t)$ is a function defined on $[0,1] \times [0,1] \times [0,+\infty)$ and satisfies the following diffusion equation

$$\frac{\partial u}{\partial t} = \nabla \cdot (\boldsymbol{D} \nabla u) \tag{2.22}$$

with the same diffusivity $\boldsymbol{D}$ as in Eq. 2.5 and the same boundary conditions as in Eq. 2.17:

$$\begin{aligned} u(x,0,t) = g_0(x,t), \quad u(x,1,t) = g_1(x,t), \\ \frac{\partial u(0,y,t)}{\partial x} = \frac{\partial u(1,y,t)}{\partial x} = 0, \end{aligned} \tag{2.23}$$

while the initial condition is globally zero:

$$u(x, y, 0) \equiv 0. \tag{2.24}$$

With this setting, the wound region ($u = 0$) is narrowing down from the whole square domain $[0, 1] \times [0, 1]$ to a heterogeneous horizontal banded region in the middle of the domain, before finally shrinking to zero area and disappearing at $t = t_{end}$. At a certain time point $t = t_0 \in (0, t_{end})$ during this process,we set $\rho(x, y, 0) = u(x, y, t_0)$ as the initial condition of our governing equation Eq. 2.4.

In other words, this initial condition is generated by the governing equation (Eq. 2.4) but without retraction, starting from zero initial values and diffusing cells without any retraction for a period of time, until retractions were introduced. At the moment right before the first retraction, cell densities across the domain $[0, 1] \times [0, 1]$ are the initial values for the governing equation. This enables us to start with a variable, and more physiological, initial condition compared to taking a constant values at the wound edge.

2.3.3 Positive definite diffusivity

The matrix $d \cdot (w_I \boldsymbol{I} + w_A \boldsymbol{A})$ is diagonal and has a positive spectrum. Therefore, the diffusivity $\boldsymbol{D} = d \cdot (w_I \boldsymbol{I} + w_A \boldsymbol{A}) \cdot \hat{D}_\alpha(\rho)$ of the governing equation (Eq. 2.4) is positive definite if and only if the scalar diffusion coefficient $\hat{D}_\alpha(\rho) > 0$, which depends on the value of adhesion coefficient α. By inspecting this 5-th degree polynomial, we see that $\hat{D}_\alpha(\rho) > 0$ unconditionally holds for all levels of cell density $\rho \in (0, 1)$ as long as

$$\alpha < \hat{\alpha} := \frac{1}{17 - 4\sqrt{15}} \approx \frac{2}{3} \tag{2.25}$$

with a critical value $\hat{\alpha}$. When $\alpha \geq \hat{\alpha}$, there exists an interval

$$I_\alpha = \left(\frac{1 + 7\alpha - \sqrt{1 - 34\alpha + 49\alpha^2}}{12\alpha}, \frac{1 + 7\alpha + \sqrt{1 - 34\alpha + 49\alpha^2}}{12\alpha} \right) \tag{2.26}$$

such that $\hat{D}_\alpha(\rho) < 0$ if and only if $\rho \in I_\alpha$. That is, the diffusivity is negative definite when cell density $\rho \in I_\alpha$, which results in the ill-posedness of the initial value PDE problem. As $\alpha \to 1$, the interval I_α expands from a single point $17 + 4\sqrt{15} \approx 1.5$ to $I_1 = (1/3,\ 1)$.

2.3.4 Retraction is modeled by advection

Performing a Taylor expansion on the cell density ρ, centered at $\boldsymbol{x} = \boldsymbol{x}_{i,j}$, in the discrete master equation (Eq. 2.1) without specifying $b^{\rightarrow}_{i,j}$, we have

$$\frac{\partial \rho}{\partial t} = \nabla \cdot (\boldsymbol{D} \nabla \rho + h \cdot (1 - \rho)(1 - \alpha\rho)^3 \cdot (b^{\leftarrow} - b^{\rightarrow}, b^{\uparrow} - b^{\downarrow})^T) + \mathcal{O}(h^2) \tag{2.27}$$

where $\boldsymbol{D}$ is the same diffusivity as in Eq. 2.5. By taking $h \to 0$, the continuum limit would be a simple diffusion equation $\partial\rho/\partial t = \nabla \cdot (\boldsymbol{D}\nabla\rho)$ without an advection term, unless both $\Delta b^{\leftrightarrow} = b^{\leftarrow} - b^{\rightarrow}$ and $\Delta b^{\updownarrow} = b^{\uparrow} - b^{\downarrow}$ are $\mathcal{O}(1/h)$, the advection scaling. Therefore, we define $b^{\rightarrow}_{i,j} := r^{\rightarrow}_{i,j}/h$ with $r^{\rightarrow}_{i,j} \in \mathcal{O}(1)$. By taking $h \to 0$ under this setting, Eq. 2.27 turns into our continuum limit (Eq. 2.4), where the retraction is modeled by advection.

2.3.5 Function smoothing

To localize the retraction region (Eq. 2.10), we smooth the Heaviside function $H(\gamma-\rho)$ (Eq. 2.11) using a hyperbolic tangent function

$$\tilde{H}(\gamma-\rho)=\frac{1}{2}\cdot(1+\tanh(k\cdot(\gamma-\rho))), \tag{2.28}$$

where k is the steepness level at transition point $\rho=\gamma$ ($k=10$ was adapted in the simulations). On the other hand, the indicator function $\mathbb{1}_{\Omega_i}(\boldsymbol{x})$ is smoothed using a 2D generalized bell-shaped function:

$$\tilde{\mathbb{1}}_{\Omega_i}(\boldsymbol{x})=\frac{1}{1+(\frac{dist(\boldsymbol{x},\Omega_i)}{k_1})^{2k_2}}, \tag{2.29}$$

where k_1 and k_2 are parameters determining the width and steepness of the transition region in the smoothing process. The distance between a point $\boldsymbol{x}$ and a set Ω_i in 2D Euclidean space is induced by a natural 2-norm $\|\cdot\|$:

$$dist(\boldsymbol{x},\Omega_i):=\inf_{\boldsymbol{y}\in\Omega_i}\|\boldsymbol{x}-\boldsymbol{y}\|. \tag{2.30}$$

Since the region Ω_i is banded, the indicator function $\mathbb{1}_{\Omega_i}(\boldsymbol{x})$ is equivalent to its 1D form $\mathbb{1}_{[c_i-\omega_r/2,c_i+\omega_r/2]}(x)$ (Eq. 2.12). Therefore, the 2D generalized bell-shaped function $\tilde{\mathbb{1}}_{\Omega_i}(\boldsymbol{x})$ (Eq. 2.29) can be simplified into a 1D version:

$$\tilde{\mathbb{1}}_{[c_i-\omega_r/2,c_i+\omega_r/2]}(x) = \frac{1}{1+\left|\frac{x-c_i}{k_1\omega_r}\right|^{2k_2}}. \tag{2.31}$$

By adjusting the center and the width of the characteristic interval, the generalized bell-shaped function given above can be applied to smooth the indicator function in time $\mathbb{1}_{[\tau_i,\tau_i+\mathcal{T}_i)}(t)$ as the following:

$$\tilde{\mathbb{1}}_{[\tau_i,\tau_i+\mathcal{T}_i)}(t) = \frac{1}{1+\left|\frac{t-\tau_i-\frac{1}{2}\mathcal{T}_i}{k_1\mathcal{T}_i}\right|^{2k_2}}. \tag{2.32}$$

Since the spatial regions of retractions decay away before the next retraction event occurs, shifts in the retraction region $c_i \sim \mathcal{U}(0,1)$ do not introduce discontinuities. Note that the selection of width and steepness parameters (k_1 and k_2) for smoothing indicator functions are different for the spatial and temporal localizations of retraction (Fig A.4).

2.3.6 Model dimensionalization

Recall that Eq. 2.1 is our non-dimensional master equation with the transitional probability Eq. 2.2. In order to relate the dimensions in the model to the experiments, we take the dimensional variables to be (1) $\hat{\rho}_{i,j} := \rho_{\max} \cdot \rho_{i,j}$ ($\rho_{\max}$ is the maximal cell density), (2) $\hat{h} := l \cdot h$ (l is the characteristic length) and (3) $\hat{t} := \lambda^{-1} \cdot t$ (λ^{-1} is the characteristic time). Hence, the dimensional transitional probability becomes

$$\hat{T}^{\rightarrow}_{i,j} = (1-\tfrac{\hat{\rho}_{i+1,j}}{\rho_{max}})(1-\alpha\tfrac{\hat{\rho}_{i-1,j}}{\rho_{max}})(1-\alpha\tfrac{\hat{\rho}_{i,j+1}}{\rho_{max}})(1-\alpha\tfrac{\hat{\rho}_{i,j-1}}{\rho_{max}})(d^{\leftrightarrow}\cdot\tfrac{\hat{\rho}_{i,j}}{\rho_{max}}\cdot\tfrac{l^2}{\hat{h}^2}+r^{\rightarrow}_{i,j}\cdot\tfrac{l}{\hat{h}}), \tag{2.33}$$

which can be taken into the master equation (Eq. 2.1) with the dimensional time derivative

$$\frac{\partial \rho}{\partial t} = \frac{\partial(\frac{\hat{\rho}}{\rho_{max}})}{\lambda \hat{t}} = \frac{1}{\lambda \rho_{max}} \cdot \frac{\partial \hat{\rho}}{\partial \hat{t}} \tag{2.34}$$

and obtain the continuum limit by taking $\hat{h} \to 0$:

$$\frac{\partial \hat{\rho}}{\partial \hat{t}} = \nabla \cdot (\tilde{\boldsymbol{D}} \nabla \hat{\rho}) + \nabla \cdot (\tilde{\boldsymbol{R}} \hat{\rho}). \tag{2.35}$$

Here, $\tilde{\boldsymbol{D}}$ is the dimensional diffusivity (diffusion coefficient) given by

$$\tilde{\boldsymbol{D}} = \frac{\lambda l^2}{\rho_{max}^5} \cdot d \cdot (w_I \boldsymbol{I} + w_A \boldsymbol{A}) \cdot \tilde{D}_\alpha(\hat{\rho}) \tag{2.36}$$

with

$$\begin{aligned} \tilde{D}_\alpha(\hat{\rho}) =& 2\rho_{max}^4 \hat{\rho} - (1 + 11\alpha)\rho_{max}^3 \hat{\rho}^2 + (8\alpha + 16\alpha^2)\rho_{max}^2 \hat{\rho}^3 \\ & - (13\alpha^2 + 7\alpha^3)\rho_{max} \hat{\rho}^4 + 6\alpha^3 \hat{\rho}^5, \end{aligned} \tag{2.37}$$

and $\boldsymbol{I} = \boldsymbol{I}_2$, $\boldsymbol{A} = diag(0, 1)$ are defined as before in Eq. 2.5. On the other hand, $\tilde{\boldsymbol{R}}$ is the dimensionalized retraction (advection velocity) given by

$$\tilde{\boldsymbol{R}} = \frac{\lambda l}{\rho_{max}^4} \cdot (\rho_{max} - \hat{\rho})(\rho_{max} - \alpha\hat{\rho})^3 \cdot (\Delta r^{\leftrightarrow}, \Delta r^{\updownarrow})^T \in \mathbb{R}^2 \tag{2.38}$$

where $\Delta r^{\leftrightarrow}$ and $\Delta r^{\updownarrow}$ are defined as in Eq. 2.10.

In order to connect the model with the experiments and to calculate the effective cell diffusion coefficient as well as the advection velocity, we need to know 3 parameters: λ, l and $\rho_{\max}$. We notice that $\lambda l^2 = v \cdot l$, where $v := \lambda l$ is actually the characteristic velocity (length over time). Hence, if we have a measurement of the characteristic velocity and the length scale, we can determine the characteristic time by $\lambda = v/l$. In conclusion, we can connect our theory and numerical parameters with the biological experiments in the following way:

- Maximal cell density $\rho_{\max}$ and dimensional cell density $\hat{\rho}$: here $\hat{\rho}$ is interpreted as a number density, i.e., $\hat{\rho}\ dxdy$ is the number of individuals with the position in the phase area $dxdy$ centered at (x, y). We can quantify this from the experimental results: put down a grid, count the number of cells in each single square and get a spatial representation of the cell density. In the monolayer region away from the front edge, we expect the cell density should be nearly uniform spatially and temporally, and that value could be used for $\rho_{\max}$.

- Characteristic length l: we define the characteristic length scale to be the distance from the wound edge to the region where the cells reach the maximal density in the monolayer. In our numerical tests, we did not simulate the whole experimental domain, instead, our simulation focused on the region of transition, that is, the region in which the cell density transits from the front to the maximum. Hence, our computational domain is a small region

around the wound edge (∼10 cell lengths).

- Characteristic velocity v: the velocity of the moving front can be used for this, by averaging the front advancing speed measured by cell shape analysis.

- Characteristic time λ^{-1}: since we already have the way to determine the characteristic length l and velocity v, the characteristic time can be derived directly by $\lambda^{-1} = l/v$.

With the measurements mentioned above, we are able to calculate $\rho_{\max}$, l, v, λ and hence the diffusion coefficient and retraction velocity. At this point, we do not have a direct measurement for the adhesion coefficient α. A direct measurement for the cell-cell adhesion is being considered in our future work.

2.4 Discussion

We developed our mathematical model to describe the dynamics of a straight scratch assay, which was the type of wound used in our experiments. However, for other wound geometries, the directional components of the model, such as the diffusion anisotropy, would need to be modified. In a circular wound, for example, the diffusion anisotropy would tend to be oriented in the radial direction corresponding to the alignment of cells moving radially inward toward the wound region. Furthermore, as a circular wound heals, the length of the wound would decrease over time. However, the roughness of the wound edge would increase, similar to the linear scratch assay considered here. In such a situation, rather than using the raw wound edge length as we do for simplicity, it would be necessary to normalize it, for instance by the perimeter of the circle.

Chapter 3

Generating model predictions through experimental data calibration

3.1 Introduction

Simulations of wound closure, obtained by numerically solving the nonlinear PDEs from the models presented in the previous chapter, offer a deeper understanding of how each model parameter contributes at both the single-cell and monolayer levels. Additionally, integrating experimental data from these scales allows for precise calibration of the model. In this chapter, we calibrate the model for each PIEZO1 phenotype and derive predictions by comparing the modeling outcomes with experimental observations. We uncover the distinct role that coordinated directionality plays in replicating experimental observations and find that PIEZO1 activity down-regulates this directionality during collective cell migration in wound healing.

To assess the robustness of our model predictions, we conduct a comprehensive sensitivity analysis. We examine the impact of different modeling frameworks on the results by repeating

all simulations using our fully continuum model of adhesion. The outcomes are qualitatively consistent with those obtained from the upscaled adhesion model (see Figs A.14 and A.15), suggesting that the hindering effect of cell-cell adhesion can be effectively modeled in various ways without altering the qualitative results. Furthermore, we test the sensitivity of our conclusions regarding the role of PIEZO1 in coordinated directionality with respect to the details of the mathematical models of cell motility and retraction processes. Our findings confirm the robustness of our predictions.

The subsequent experiments, conducted by Jesse Holt and described in Section 3.5, consistently validate our model predictions, highlighting the robustness and reliability of our theoretical framework.

3.2 Methods

3.2.1 Numerical implementation

In order to solve the governing equation (Eq. 2.4), we firstly carry out a forward time discretization (with size Δt) on the left hand side $\partial\rho/\partial t$ by $(\rho(\boldsymbol{x}_{i,j}, t+\Delta t) - \rho(\boldsymbol{x}_{i,j}, t))/\Delta t$. In terms of space discretization (right hand side), the transitional probability is proved to be separable (Eq. 2.3) in the discrete model, which allows us to work on the diffusion part and advection part separately: for the diffusion part, a natural discretization is directly given by the discrete model (e.g., centered finite differences); for the advection part, we apply a 2nd order weighted essentially non-oscillatory (WENO) method [38, 57] to discretize the equation. Hence, an explicit finite difference scheme was used to update the cell density at the nth time step $\rho^n_{i,j}$ iteratively on the simulation domain $[0,1]\times[0,1]$ until wound closure.

3.2.2 Model parameter study

Through a parameter study with model simulation, we can explore the effects of model parameters on two experimentally-measured phenotypes affected by PIEZO1 activity during keratinocyte reepithelialization: (1) the rate of normalized wound closure and (2) normalized wound edge length, a measurement to characterize the degree of cellular protrusions and retractions during wound healing, which is correlated with leader cell presence (Fig 1.1G and 1.1H; [87]). These metrics were chosen because they can be directly measured and compared to experimental data. The method of our parameter study involves altering individual model parameters one at a time while holding the remaining parameters at their base values (Fig A.4) to observe how such variations affect wound closure and edge roughness.

3.2.3 Model calibration with experimental data

We utilized and expanded upon analyses performed on single migrating keratinocytes in the prior study [35], to compile an experimental dataset characterizing PIEZO1's effect on: cell motility, retraction duration, inter-retraction duration and cell retraction strength (Figs 3.1A and A.5; Table 3.1). Cell motility parameters were calculated by extracting cell speed information from single cell tracking experiments which were previously performed using single *Piezo1*-cKO and *Piezo1*-GoF keratinocytes [35] (Figs 3.1A, *left* and A.5; Table 3.1). We expanded upon this work by also tracking individually migrating Yoda1-treated and DMSO-treated keratinocytes to incorporate the effect of Yoda1 on cell motility into our model predictions. Similar to our observations in *Piezo1*-GoF keratinocytes, Yoda1 treatment had no effect on the motility of single migrating keratinocytes compared to DMSO-treated control cells (Fig A.6). To find the average duration of retractions and intervals between successive retractions for all experimental conditions (*Piezo1*-cKO, *Piezo1*-GoF, Yoda1-treatment and the respective controls), we utilized two analysis methods performed in the prior study

Experimental Observations	Retraction Duration	Inter-retraction Duration	Retraction Strength	Cell Motility
Piezo1-cKO relative to $\text{Control}_{\text{cKO}}$	+	+	+	+
Piezo1-GoF relative to $\text{Control}_{\text{GoF}}$	+	−	+	∼
Yoda1-treated relative to DMSO-treated	−	−	+	∼

Table 3.1: **PIEZO1 activity affects single cell migration.** Summary table presenting experimental results obtained from quantitative analysis of single cell migration experiments (e.g., kymograph, cell protrusion analyses, single cell tracking assays). A "+" indicates an increase, "−" indicates a decrease, and "∼" indicates no statistically significant change between Control and Test condition. All data aside from DMSO-treated and Yoda1-treated cell motility (Fig A.6) was initially published in [35]. Actual data values for each condition can be found listed in Fig A.5.

[35]: (1) kymographs (Fig 3.1A, *right*), which graphically depict the retraction and inter-retraction durations of the leading edge of migrating keratinocytes, and (2) a cell protrusion quantification software, ADAPT [6], which quantifies the strength of retraction events at the leading edge. Thus, from these measurements (Figs 3.1A and A.5; Table 3.1), we can calibrate our model parameters based on experimental measurements, enabling us to make experimentally relevant predictions regarding PIEZO1's influence on wound closure behavior.

To calibrate our model, we created a respective simulation control for each experimental condition (*Piezo1*-cKO, *Piezo1*-GoF and Yoda1-treated) by fixing the values of model parameters to a basecase, where the frequency of retraction was set to be the same as the corresponding experimental control (see Fig A.4 for the full list of model parameters and their base values). For a given experimental condition, the model parameters related to retraction (retraction duration, inter-retraction duration, retraction strength) and cell motility were adjusted from the control condition by the same proportions as their experimentally-measured changes relative to the control condition (Figs 3.1A and A.5; Table 3.1). In particular, the mean retraction and inter-retraction durations μ_r and μ_{nr}, the cell motility d and the mean retraction strength μ_s are changed proportionally in the model.

In our model calibration, the experimentally derived "Single Cell Migration" dataset guides the changes in model parameters of retraction strength, retraction duration, inter-retraction duration and cell motility when PIEZO1 activity is altered. However, cell-cell adhesion and

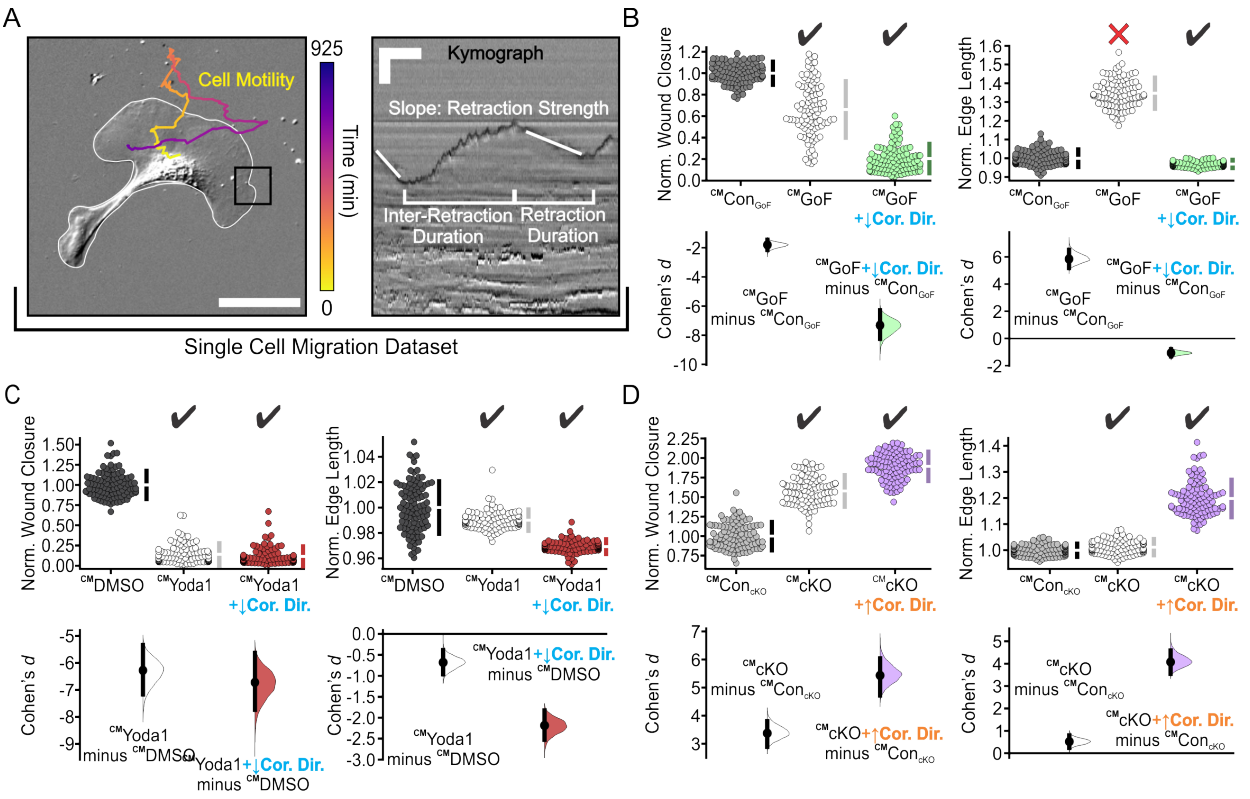

Figure 3.1: **PIEZO1 activity is predicted to regulate wound closure by hindering coordinated directionality**. **(A)** Schematic depicting experimentally measured features used to generate the single cell migration dataset. Left, representative still image of migrating keratinocyte with overlaid cell trajectory. Trajectory is derived from tracking cell motility during time-lapse experiments. Color denotes passage of time such that yellow is the starting position and purple denotes track end position. Cell boundary is in white. Scale bar = 100 μm. Kymographs (*right*) taken at the leading edge of migrating cells (e.g., similar to black box in the left image) are used to obtain information regarding inter-retraction duration and retraction duration. The cell protrusion quantification software, ADAPT [6] was used to gain information regarding retraction strength. Scale bar = 10 μm, Time bar = 5 min. **(B)** Cumming plots showing simulation results using the calibrated model (^{CM}) to predict how PIEZO1 affects normalized wound closure (*left plots*) and wound edge length (*right plots*) in simulated Control$_{GoF}$ monolayers (*dark gray*), *Piezo1*-GoF monolayers without altered coordinated directionality parameters (*white*), and *Piezo1*-GoF monolayers with coordinated directionality decreased (*green*). See Methods Section *Model parameter adjustment* for the details. **(C)** Similar to B but using simulation results from DMSO-treated monolayers (*black*), Yoda1-treated monolayers without altered coordinated directionality parameters (*white*), and Yoda1-treated monolayers with coordinated directionality decreased (*red).* **(D)** Similar to B but using simulation results from Control$_{cKO}$ monolayers (*light gray*), *Piezo1*-cKO monolayers without altered coordinated directionality parameters (*white*), and *Piezo1*-cKO monolayers with coordinated directionality increased (*purple).* In B-D, n = 100 simulation results for each condition, and ^{CM} denotes "Calibrated Model". To account for

Figure 3.1 continued on next page

Figure 3.1 continued
differences between control cases, data are normalized by rescaling to the mean of the corresponding control, while the adhesion coefficient is fixed at the base value 0.2. Larger normalized wound closure indicates faster wound closure, while a smaller normalized wound closure indicates slower wound closure. Similarly, a larger normalized edge length indicates a more featured wound while a smaller normalized edge length indicates a flatter or less featured wound. Black check marks at the top of each plot condition indicate that simulation results match experimental trends while a red cross indicates simulation fails to match the experiment trends. See also Table 3.3, Figs A.7 and A.8. For comparison with experimental data see Fig 1.1B, 1.1G and 1.1H.

coordinated directionality were not measured directly in the experiments and instead are inferred by trying to match model and experimental results. While both cell-cell adhesion and coordinated directionality are designed to range from 0 to 1 in our model, the feasible adhesion coefficient actually needs to be bounded above by 0.66 in order for the diffusivity to be positive definite (see Section 2.3.3 for detailed derivation). Since the dependence of wound closure rate and wound edge length with respect to individual model parameters was already numerically shown to be a monotonic function of these parameters (Figs 2.1G, 2.1H and A.3), it is sufficient to directly use the extrema of the model parameters: 1 for increased coordinated directionality, 0.66 for an increased adhesion, and 0 in the case that coordinated directionality and/or adhesion is decreased. For example, when matching experiments and simulations requires an increased coordinated directionality, we take $w_A = 1$. Because of the dependency of the outcomes (wound closure rate and edge lengths), if increasing a model parameter to its maxima fails to match the experimental trends, it would be impossible to match with smaller values.

3.3 Results

3.3.1 Coordinated directionality is the key model parameter which replicates PIEZO1 reepithelialization phenotypes

Simulations of wound closure provide insight into how individual model parameters affect the wound closure process (Fig 2.1B-E). During simulations we found that wounds would fail to close if parameters exceed a reasonable range (Figs 2.1F and A.2). For instance, when retraction strength is set over a certain critical value, cells are unable to overcome retractions of the wound edge which causes wounds to remain open indefinitely (Fig 2.1F). This model prediction is consistent with experimental results where Yoda1 treatment sometimes resulted in an increase in wound area during wound closure assays (Fig 1.1B; [35]).

By plotting the average rate of wound closure and edge length across multiple simulations we can see how the setting of individual model parameters compares to experimental trends we observe (Figs 2.1G, 2.1H and A.3). We find that increasing the retraction strength parameter hinders wound closure, a result which is in line with the mechanism proposed by Holt *et al.* [35] (Fig 2.1G). However, our parameter study also shows that increased retraction strength results in a longer wound edge length, suggesting an increase in leader cell-like protrusions along the simulated wound margin. This contradicts our experimental observations in which a shorter wound edge length with fewer leader cells accompanies delayed wound closure (Fig 2.1G; Table 3.2). Similarly, we find that lower retraction strength elicited faster wound closure with shorter edge lengths due to fewer leader cell-like protrusions which also contradicts our experimental results (Fig 2.1G). Together, these results indicate that there is more to PIEZO1's role in cell migration than retraction alone.

To identify possible contributors of wound closure regulation influenced by PIEZO1 activity, we performed an extensive parameter study in which we made adjustments to the model

Experimental Observations	Norm. Wound Closure	Norm. Edge Length
Piezo1-cKO relative to $\text{Control}_{\text{cKO}}$	+	+
Piezo1-GoF relative to $\text{Control}_{\text{GoF}}$	−	−
Yoda1-treated relative to DMSO-treated	−	−
Model Parameter	**Norm. Wound Closure**	**Norm. Edge Length**
retraction strength	−	+
retraction duration	−	+
inter-retraction duration	+	−
cell motility	+	−
cell-cell adhesion	−	+
coordinated directionality	**+**	**+**

Table 3.2: **Coordinated directionality is the key model parameter which replicates PIEZO1 reepithelialization phenotypes.** *Top*: Summary table of monolayer experimental results on normalized wound closure and wound edge length. See also Fig 1.1. *Bottom*: Summary table of simulation results, depicting the effect of model parameters on normalized wound closure and wound edge length. For model parameters, single cell parameters (retraction strength, retraction duration, inter-retraction duration and cell motility) are separated from parameters which come from collective cell settings (cell-cell adhesion and coordinated directionality). A "+" indicates the wound feature is positively correlated with the model parameter, e.g., wound edge length increases with increased retraction strength, whereas "−" indicates a negative correlation, e.g., normalized wound closure is reduced with increasing retraction strength. Bolded italicized text denotes model parameters which correspond with experimental trends. See also Figs 2.1G, 2.1H and A.3.

parameters of: cell-cell adhesion, retraction duration, inter-retraction duration, cell motility and coordinated directionality. We found that manipulation of all parameters aside from coordinated directionality fail to replicate the observed experimental results, i.e., faster wound closure accompanying a longer edge length, or conversely, delayed closure occurring with a shorter edge length (Table 3.2; Fig A.3). By increasing the coordinated directionality parameter within our model, wounds close faster with longer edge lengths due to the presence of more leader cell-like protrusions, replicating experimental observations in *Piezo1*-cKO monolayers (Fig 2.1H). On the other hand, under low coordinated directionality parameter conditions cells migrate more aimlessly, with formation of fewer leader-cell like protrusions along the wound edge and with inhibited closure, similar to observations from *Piezo1*-GoF and Yoda1-treated wounds (Fig 2.1H). Taken together, our parameter study predicts that while other model parameters, including retraction strength, affect keratinocyte migration,

coordinated directionality plays a key role in modeling PIEZO1 inhibition of keratinocyte reepithelialization.

3.3.2 PIEZO1 activity is predicted to regulate wound closure by hindering coordinated directionality

Through numerical simulation, our modeling parameter study reveals how altering individual model parameters one at a time while keeping the remaining parameters at their base values (Fig A.4) affects wound closure. However, experimental results reveal that PIEZO1 activity may alter more than one model parameter, which may generate compensating effects that reduce the contribution of coordinated directionality in the experimental setting. Therefore, we sought to further constrain the mathematical model by incorporating model parameters derived from experimental data. To this end, we utilized the experimental dataset (Figs 3.1A and A.5; Table 3.1) to calibrate the model (detailed in Section 3.2.3).

With cell-cell adhesion and coordinated directionality unchanged compared to $\text{Control}_{\text{GoF}}$, we find that while we can replicate simulated monolayers of *Piezo1*-GoF keratinocytes having slower wound closure compared to simulated $\text{Control}_{\text{GoF}}$ monolayers, we fail to observe the expected decreasing change in leader cell-like protrusions as indicated by a smaller simulated monolayer edge length (Fig 3.1B). However, by lowering the collective migration parameter of coordinated directionality, we recapitulate the experimental phenotype of both a shorter edge length and slower wound closure in simulated *Piezo1*-GoF monolayers (Fig 3.1B). On the other hand, we see that model simulations calibrated by the single cell migration dataset for both *Piezo1*-cKO and Yoda1-treated keratinocytes reproduce the expected experimental trends; however, by incorporating changes to coordinated directionality we observe a stronger effect (Fig 3.1C and 3.1D). Notably, we observe that adjustment of cell-cell adhesion parameters, another model parameter integral to collective migration, fails to replicate

Model Parameter Sets	Norm. Wound Closure	Norm. Edge Length	Experimental Match
$^{CM}\text{Control}_{\text{GoF}}$ to ^{CM}GoF	−	+	✗
$^{CM}\text{Control}_{\text{GoF}}$ to ^{CM}GoF + cell-cell adhesion ↑	−−	+	✗
$^{CM}\text{Control}_{\text{GoF}}$ to ^{CM}GoF + cell-cell adhesion ↓	+	+	✗
$^{CM}\text{Control}_{\text{GoF}}$ to ^{CM}GoF + coordinated directionality ↓	−−	−	✓
^{CM}DMSO to ^{CM}Yoda1	−	−	✓
^{CM}DMSO to ^{CM}Yoda1 + cell-cell adhesion ↑	−−	−−	✓
^{CM}DMSO to ^{CM}Yoda1 + cell-cell adhesion ↓	−	−	✓
^{CM}DMSO to ^{CM}Yoda1 + coordinated directionality ↓	−−	−−	✓
$^{CM}\text{Control}_{\text{cKO}}$ to ^{CM}cKO	+	+	✓
$^{CM}\text{Control}_{\text{cKO}}$ to ^{CM}cKO + cell-cell adhesion ↑	−	++	✗
$^{CM}\text{Control}_{\text{cKO}}$ to ^{CM}cKO + cell-cell adhesion ↓	++	+	✓
$^{CM}\text{Control}_{\text{cKO}}$ to ^{CM}cKO + coordinated directionality ↑	++	++	✓

Table 3.3: **Coordinated directionality recovers monolayer closure behavior from single cell data.** Summary table depicting simulation results using the calibrated model ($^{\text{CM}}$) to predict how PIEZO1 affects normalized wound closure and normalized edge length with altered adhesion and coordinated directionality parameters. A "+" indicates a parameter set has a predicted increase upon an experimental measure while a "−" indicates a predicted decrease. Double signs (++/−−) represent a stronger observed effect on the simulated measure than single signs (+/−). Red font and cross mark ✗ indicate that model predictions calibrated by the "Single Cell Migration" dataset do not match experimental trends (Table 3.2), while a check mark ✓indicates that model predictions are consistent with experimental results. See also Figs 3.1, A.7 and A.8.

all experimental results, reinforcing that coordinated directionality plays a primary role in PIEZO1's effect on reepithelialization (Table 3.3; Fig A.7). The more retraction regions generated, the slower the wound healing process and the longer the wound edge length. Matching the experimental results when PIEZO1 signaling is upregulated still required a decrease in coordinated directionality. Taken together, these studies demonstrate that only by including alterations to coordinated directionality are we able to mimic all experimental phenotypes.

In sum, our model predicts that PIEZO1 activity affects coordinated directionality within monolayers such that increased PIEZO1 activity inhibits the cells ability to move cohesively during collective migration, ultimately delaying wound closure. On the other hand, in monolayers which lack PIEZO1 expression, cells are predicted to have stronger directionality signals and recruit more follower cells to close the wound faster.

3.4 Sensitivity analysis of model predictions

3.4.1 Selection of modeling frameworks

To determine whether the effect of higher PIEZO1 activity hindering coordinated directionality is sensitive to the specifics of the mathematical model of cell-cell adhesion, we test our phenomenological continuum modeling framework (presented in Section 2.2.2). In this approach, the diffusion coefficient is assumed to be a decreasing function of cell-cell adhesion, following the methodology of Amereh *et al.*, 2021 [1], rather than being derived from upscaling a discrete model.

We replicated all the previous simulations related to *Piezo1*-cKO, *Piezo1*-GoF, and Yoda1 using this new phenomenological model to compare the predictions with our upscaled model. Similar to the calibration process for the upscaled model, we adjusted model parameters based on experimental data (Fig A.5). This involved varying model parameters from a wild type (e.g., $\text{Control}_{\text{GoF}}$) to a PIEZO1 phenotype (e.g., *Piezo1*-GoF), and measuring changes of wound healing metrics (wound closure and edge length) from repeated simulations. In line with our previous findings, we observed that the simulation results from the $\text{Control}_{\text{GoF}}$ to *Piezo1*-GoF case are only able to replicate experimental observations if coordinated directionality is reduced. That is, by reducing the parameter of coordinated directionality, we recapitulated the experimental phenotype of both a shorter edge length and slower wound closure in simulated *Piezo1*-GoF monolayers (Fig A.14A). Importantly, we noted that changes to the diffusion coefficient, according to changes in cell-cell adhesion, alone failed to replicate all experimental results (Fig A.15), consistent with the results obtained using the upscaled model of adhesion. This underscores the primary role of coordinated directionality in PIEZO1's impact on reepithelialization and reaffirms our main conclusion that PIEZO1 activity hinders coordinated directionality. Because the dependence of the diffusion coefficient and the retraction strength on cell-cell adhesion could be quite

different quantitatively, as suggested by our upscaled model (see Eq. 2.8 and Eq. 2.9), for simplicity, here we focused only on the changes in d and not on $\Delta r^{\leftrightarrow}$ and $\Delta r^{\updownarrow}$. However, we varied the retraction strengths and durations in the context of the original upscaled model (see Section 3.4.2 for details) and reached the same conclusion.

3.4.2 Robustness of model calibration

The experimental data used for model calibration can be categorized into two main components: cell motility and retraction processes (including retraction duration, inter-retraction duration, and retraction strength). In the process of model calibration, we utilized experimental data at the single-cell level from Table 3.1 and Fig A.5. To test whether our conclusions depend on the quantitative single cell data, we varied the magnitudes of the motility and retraction processes.

For cell motility, we used experimental data from the monolayers (Fig A.9), which shows that cell motility within the monolayer increased in *Piezo1*-cKO and decreased in *Piezo1*-GoF and Yoda1-treatment compared to their respective experimental controls. Calibrating our original model using motility measured from monolayers, together with the original magnitudes of the retraction processes, and maintaining cell-cell adhesion and coordinated directionality as observed in $\text{Control}_{\text{GoF}}$, we found that while we could replicate simulated monolayers of *Piezo1*-GoF keratinocytes exhibiting slower wound closure compared to simulated $\text{Control}_{\text{GoF}}$ monolayers, but we failed to observe the decrease in simulated monolayer edge length seen in experiments (Fig A.16A). However, by reducing the parameter of coordinated directionality, we recapitulated the experimental phenotype of both a shorter edge length and slower wound closure in simulated *Piezo1*-GoF monolayers (Fig A.16A). On the other hand, our model simulations, calibrated using the monolayer cell motility dataset along with original retraction processes for both *Piezo1*-cKO and Yoda1-treated keratinocytes, re-

produced the observed experimental trends. However, with adjustments to coordinated directionality, we observed a more pronounced effect (Fig A.16B-C). Importantly, we noted that changes to cell-cell adhesion parameters alone failed to replicate all experimental results, underscoring the primary role of coordinated directionality in PIEZO1's impact on reepithelialization (Fig A.17).

For retraction processes (retraction duration, inter-retraction duration and retraction strength), the prior work [35] indicated qualitative consistency in between single cell data and monolayer experiments. For example, in both single cell and monolayer experiments, retractions in the presence of Yoda1 consistently exhibit shorter durations and larger magnitude retractions compared to DMSO, albeit with variations in the degree of change. Building upon this qualitative observation from experiments, we conducted additional simulations. In these simulations, we recalibrated our original model based on general qualitative trends rather than specific quantitative values for retraction. For instance, Yoda1-treated cells exhibit significantly stronger retraction, with a strength approximately three times (around 2.87) that of its control DMSO-treated cells (Fig A.5). Instead of adhering strictly to this specific ratio of 2.87, we performed simulations using two additional ratios, one larger and and one smaller, while maintaining the qualitative trend in which the retraction strength in Yoda1-treated cells is greater than in DMSO-treated cells. This approach was also applied to the calibration of the retraction duration and the inter-retraction duration, with adjustments made in various ratios rather than relying on specific quantitative values derived from experimental statistics (Fig A.5). Again, two additional values of the durations were used.

Applying this recalibration to simulated monolayers of *Piezo1*-GoF keratinocytes, we observed slower wound closure compared to $\text{Control}_{\text{GoF}}$ monolayers; however, the expected decrease in simulated monolayer edge length was not observed (Fig A.18). Consistent with our previous findings, simulations from the $\text{Control}_{\text{GoF}}$ to *Piezo1*-GoF case could replicate experimental observations only when coordinated directionality was reduced. Specifically,

by lowering the parameter of coordinated directionality, we recapitulated the experimental phenotype of both a shorter edge length and slower wound closure in simulated *Piezo1*-GoF monolayers, while changes to cell-cell adhesion parameters failed to replicate all experimental results (Fig A.18). The results from this recalibrated model reaffirm the role of coordinated directionality, leading to the same fundamental conclusion that PIEZO1 activity hinders coordinated directionality.

3.5 Experimental validation of model predictions

3.5.1 PIEZO1 activity inhibits persistence of direction during keratinocyte collective migration

To test our model's prediction we first utilized a cell tracking assay to examine the motility of individual cells during collective migration. To track the movement of individual cells within monolayers we utilized the live-cell DNA stain SiR-Hoechst to label individual nuclei within monolayers [58]. After imaging collective cell migration over the course of several hours, we tracked the movement of individual nuclei and analyzed the resulting cell trajectories (Fig 3.2A-C). The mean squared displacement (MSD) is a common metric for analyzing cell displacement as a function of time. Replicating our single cell migration observations [35], we observe that individual tracked nuclei within *Piezo1*-cKO monolayers have MSDs that are greater than that of $\text{Control}_{\text{cKO}}$ cells, demonstrating a larger area explored (Fig 3.2D). Measurement of the instantaneous cellular speed reveals that, similar to our previous observations, *Piezo1*-cKO cells migrate faster relative to littermate $\text{Control}_{\text{cKO}}$ cells (Fig A.9A). On the other hand, cells from both *Piezo1*-GoF and Yoda1-treated monolayers have MSDs that are significantly smaller (Fig 3.2E and 3.2F). This effect is distinct from our observation in single migrating cells, where we observed that *Piezo1*-GoF keratinocytes migrate

farther than $\text{Control}_{\text{GoF}}$ cells [35], and that Yoda1-treatment has no difference relative to DMSO-treated control cells (Fig A.6A). Moreover, in both *Piezo1*-GoF and Yoda1-treated monolayers we observe that increased PIEZO1 activity inhibits migration speed (Fig A.9B-C). This observation also differs from our single cell migration observations in which both *Piezo1*-GoF and Yoda1-treated keratinocytes have no difference in migration speed compared to respective control cells. Our observed differences for PIEZO1's effect on speed and MSD between single cell and collective migration results may be attributed to additional mechanical information from cell-cell interactions during collective migration affecting activation of PIEZO1.

Since coordinated directionality can, in part, be inferred by how straight the trajectories of cells in a collectively migrating group are, we measured the directional persistence of individual cell trajectories. While coordinated directionality refers to how cohesively cells migrate in a similar direction, directional persistence refers to the directed migration of individual cells or, more simply, how straight individual cell trajectories are. Notably, these two elements are often seen to co-occur in monolayers which show increased wound closure efficiency [42]. The directional persistence of a cell can be quantified by measuring the velocity autocorrelation of cell trajectories [28]. The randomness in direction of a cell's trajectory is indicated by how rapidly its velocity autocorrelation function decays: autocorrelation curves which decay slower indicate cells that have straighter migration trajectories. Measurement of the velocity autocorrelation shows that *Piezo1*-cKO keratinocytes migrating in cell monolayers move straighter than $\text{Control}_{\text{cKO}}$ cells (Fig 3.2G), similar to the previous findings in single migrating cells. In both *Piezo1*-GoF and Yoda1-treated keratinocytes, cells move less straight than their respective controls (Fig 3.2H and 3.2I). This finding also differs from findings in single cell migration results wherein Yoda1-treatment does not change directional persistence (Fig A.6C) while the *Piezo1*-GoF mutation induces straighter trajectories during single cell migration [35].

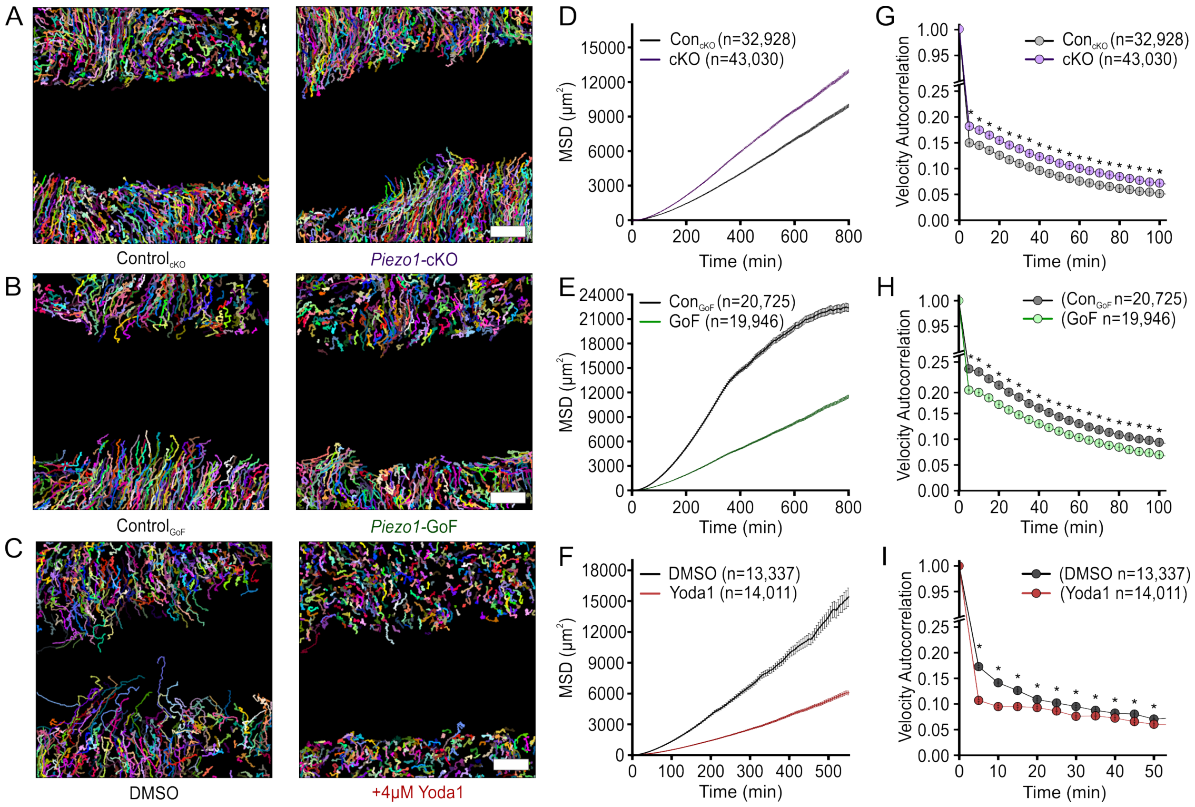

Figure 3.2: **PIEZO1 activity inhibits persistence of direction during keratinocyte collective migration. (A-C)** Representative field of view depicting individual cell trajectories derived from tracking **(A)** Control$_{\text{cKO}}$ (*left*) and *Piezo1*-cKO (*right*) keratinocytes, **(B)** Control$_{\text{GoF}}$ (*left*) and *Piezo1*-GoF (*right*) keratinocytes, and **(C)** DMSO-treated (*left*) and 4 μM Yoda1-treated (*right*) keratinocytes during collective migration experiments. Trajectory color depicts individual cell trajectories. Scale bar=100 μm. **(D-F)** Average mean squared displacement (MSD) plotted as a function of time for: **(D)** Control$_{\text{cKO}}$ (*gray*) and *Piezo1*-cKO (*purple*) keratinocytes, **(E)** Control$_{\text{GoF}}$ (*gray*) and *Piezo1*-GoF (*green*) keratinocytes, and **(F)** DMSO-treated (*gray*) and 4 μM Yoda1-treated (*red*) keratinocytes. All error bars plotted as SEM, in some instances error bars are smaller than symbols. **(G-I)** Average velocity autocorrelation measurement of: **(G)** Control$_{\text{cKO}}$ (*gray*) and *Piezo1*-cKO (*purple*) keratinocytes, **(H)** Control$_{\text{GoF}}$ (*gray*) and *Piezo1*-GoF (*green*) keratinocytes, and **(I)** DMSO-treated (*gray*) and 4 μM Yoda1-treated keratinocytes, plotted as a function of time (* denotes p value<0.0001 as calculated via Kolmogorov–Smirnov test). For Control$_{\text{cKO}}$ (n=66 unique fields of view) and *Piezo1*-cKO (n=85 unique fields of view) data plotted in A, D, G, images taken from three independent experiments. For Control$_{\text{GoF}}$ (n=56 unique fields of view) and *Piezo1*-GoF (n=51 unique fields of view) data plotted in B, E, H, images taken from four independent experiments. For DMSO-treated (n=32 unique fields of view) and 4 μM Yoda1-treated (n=31 unique fields of view) keratinocyte data plotted in C, F, I, images taken from three independent experiments. Plotted n denotes the number of individual cell trajectories. See also Fig A.9.

Taken together, our results show that PIEZO1 activity inversely correlates with both cell speed and the persistence of migration direction during keratinocyte collective migration. Our observation that the directional persistence of individual keratinocytes within a monolayer is inhibited by PIEZO1 activity during collective cell migration provides initial support for our model's prediction that coordinated directionality is affected by PIEZO1 activity.

3.5.2 Increased PIEZO1 activity inhibits the coordination of cellular motion

The coordinated movement of keratinocytes during wound reepithelialization depends on the large-scale interactions of multiple cells as they work together to close wounds. While tracking individual cells in a monolayer provides useful information regarding the locomotion of individual cells, it does not fully describe the dynamics of collectively migrating cells. To further validate our model's prediction that PIEZO1 activity inhibits coordinated directionality and to characterize the effect of PIEZO1 on large scale cellular interactions during wound closure we utilized particle image velocimetry (PIV). PIV is an optical method of flow visualization which allows us to dynamically map the velocity fields of migrating keratinocytes within a monolayer during wound closure [49, 68, 84]. By isolating the individual velocity vectors comprising a monolayer's vector field and mapping the frequency of vector directions for samples from different conditions (e.g., *Piezo1*-cKO, *Piezo1*-GoF, and Yoda1-treatment), we can visualize how PIEZO1 affects the coordinated directionality and overall coordination of motion between cells during wound closure (Fig 3.3A-C). Probability density distributions of velocity directions from Fig 3.3A-C illustrate that *Piezo1*-cKO cells flow towards the wound margin (denoted by 0 degrees) to a greater extent than littermate $\text{Control}_{\text{cKO}}$ cells (Fig 3.3D). Conversely, *Piezo1*-GoF and Yoda1-treated cells flow towards the wound margin to a lesser extent than their corresponding Controls (Fig 3.3E and 3.3F).

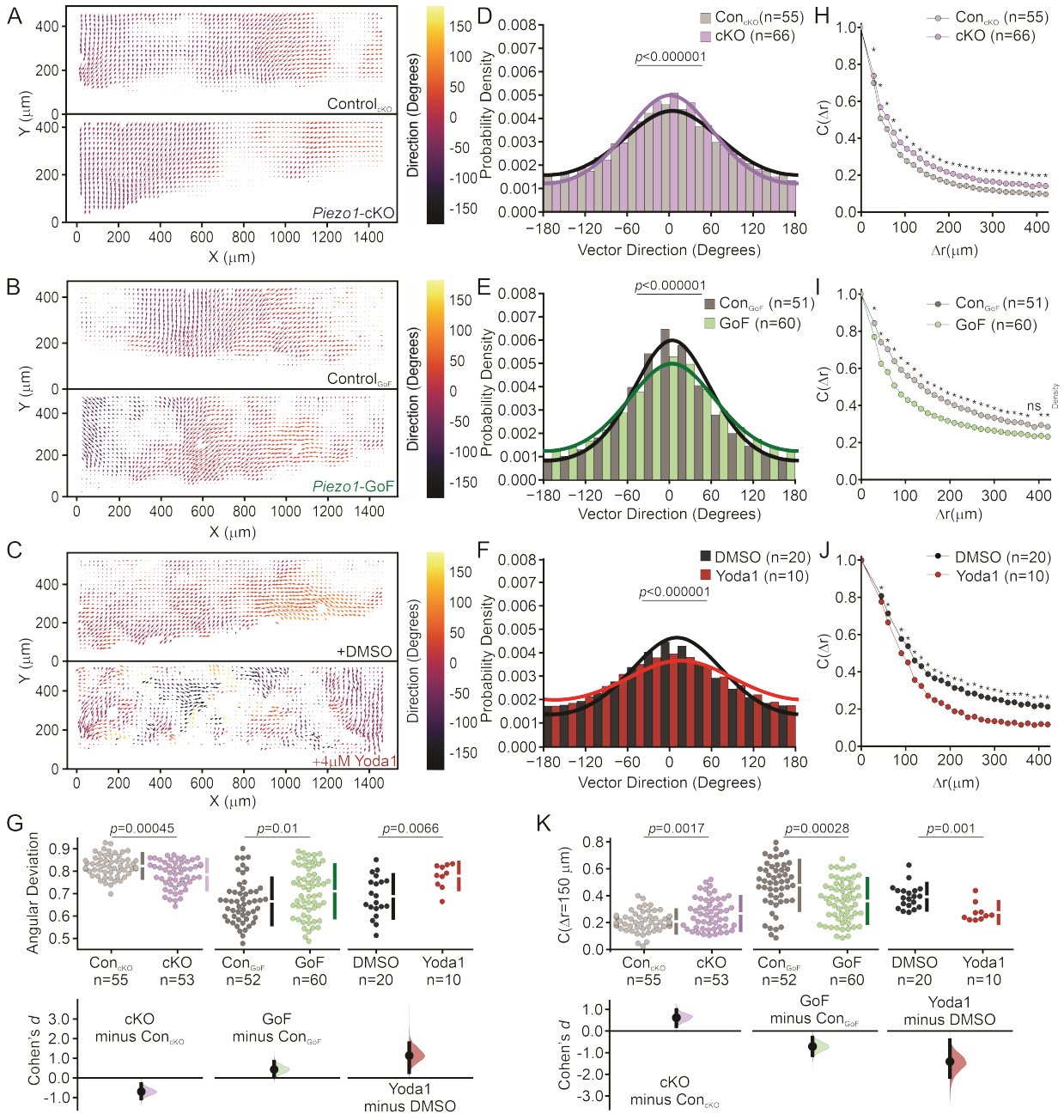

Figure 3.3: **Increased PIEZO1 activity inhibits coordinated cellular motion. (A-C)** Representative mean Particle Image Velocimetry (PIV) flow fields derived from time-lapse images of labeled nuclei from collectively migrating monolayers of: **(A)** Control$_{\text{cKO}}$ (*Top*) and *Piezo1*-cKO (*Bottom*) keratinocytes, **(B)** Control$_{\text{GoF}}$ (*Top*) and *Piezo1*-GoF (*Bottom*) keratinocytes, and **(C)** DMSO-treated (*top*) and 4 μM Yoda1-treated keratinocytes (*Bottom*) during time-lapse scratch assay experiments. An individual flow field comprises either the upper or lower monolayer sheet of a scratch assay. Flow fields are oriented such that for the Y-direction, 0 μm is positioned within the cell free region. **(D-F)** Distribution plots showing the probability density of velocity vector direction for: **(D)** Control$_{\text{cKO}}$ (*gray*; $\kappa = 0.51$) and

Figure 3.3 continued on next page

Figure 3.3 continued
Piezo1-cKO (*purple*; $\kappa = 0.71$) monolayers, **(E)** $\text{Control}_{\text{GoF}}$ (*gray*; $\kappa = 1.01$) and *Piezo1*-GoF (*green*; $\kappa = 0.71$) monolayers, and **(F)** DMSO-treated (*gray*; $\kappa = 0.61$) and Yoda1-treated (*red*; $\kappa = 0.30$) monolayers. The curves depicted in the figure represent the fitting of von Mises distributions, where a smaller reported κ corresponds to less directed migration while a larger κ indicates an increase in directed migration. For D-F, p value calculated by Chi-squared test. **(G)** Cummings plot showing the mean angular deviation, or the variability in velocity direction isolated from PIV flow fields in: $\text{Control}_{\text{cKO}}$ vs. *Piezo1*-cKO monolayers (*left*; p value calculated via two-sample t-test; Cohen's d = -0.7), $\text{Control}_{\text{GoF}}$ vs. *Piezo1*-GoF monolayers (*middle*; p value calculated via two-sample t-test; Cohen's d = 0.43) or DMSO-treated vs. 4 μM Yoda1-treated monolayers (*right*; p value calculated via two-sample t-test; Cohen's $d = 1.14$). Data are normalized such that 1 indicates highly random velocity directions and 0 indicates highly uniform velocity directions. **(H-J)** Spatial autocorrelation, $C(\Delta r)$, of the radial velocity component, which is a measure of the spatial coordination of neighboring cells in monolayers, plotted as a function of increasing length scales of: **(H)** $\text{Control}_{\text{cKO}}$ (*gray*) and *Piezo1*-cKO (*purple*) keratinocytes, **(I)** $\text{Control}_{\text{GoF}}$ (*gray*) and *Piezo1*-GoF (*green*) keratinocytes, and **(J)** DMSO-treated (*gray*) and Yoda1-treated (*red*) keratinocytes. For H, I, J * denotes a statistically significant difference, and ns denotes not statistically significant as determined by one way ANOVA test. Specific p values for plotted points can be found in Fig A.11. See also Fig A.10. (**K**) Local spatial coordination, $C(\Delta r = 150\ \mu m)$, of keratinocytes where the correlation value is set at 150 μm to measure the coordination of motion with neighboring cells in: $\text{Control}_{\text{cKO}}$ vs. *Piezo1*-cKO monolayers (*left*; p value calculated via two-sample t-test; Cohen's $d = 0.62$), $\text{Control}_{\text{GoF}}$ vs. *Piezo1*-GoF monolayers (*middle*; p value calculated via two-sample t-test; Cohen's d = -0.7) or DMSO-treated vs. 4 μM Yoda1-treated monolayers (*right*; p value calculated via Mann-Whitney test; Cohen's d = -1.4). n in B, C, E, F, H, I, J and K denotes the number of monolayer sheets imaged. For $\text{Control}_{\text{cKO}}$ and *Piezo1*-cKO data plotted in A, D, G (*left*), H, and K (*left*), images are taken from three independent experiments. For $\text{Control}_{\text{GoF}}$ and *Piezo1*-GoF data plotted in B, E, H (*middle*), I, and K (*middle*), images are taken from four independent experiments. For DMSO-treated and 4 μM Yoda1-treated keratinocyte data plotted in C, F, H (*right*), J, and K (*right*), images are taken from two independent experiments.

To fit our vector direction datasets, we employed the von Mises distribution by minimizing the mean squared error with the von Mises probability density function (Eq. C.4 in the Methods Section). The resulting fitted curves (Fig 3.3D-F) provide the best approximation of the data by adjusting the distribution parameters, including the mean (μ) and the concentration (κ, indicating the strength of directed migration in our experimental context). A smaller κ value corresponds to a flatter bell curve and a distribution closer to uniform, indicating less directed migration. Conversely, a larger κ value results in a sharper bump in the probability density function, indicating an increase in directed migration. We find that *Piezo1*-cKO cells show a higher κ ($\kappa = 0.71$) than $\text{Control}_{\text{cKO}}$ ($\kappa = 0.51$) indicating that *Piezo1*-cKO cells move with increased coordination relative to $\text{Control}_{\text{cKO}}$ cells (Fig 3.3D). On the other hand, we find that both *Piezo1*-GoF and Yoda1-treated monolayers show a loss in directed migration as illustrated by the broader distribution of isolated vector directions and a lower calculated κ value for experimental conditions ($\kappa = 0.71$ for *Piezo1*-GoF, $\kappa = 0.30$ for Yoda1-treated) relative to the respective control populations ($\kappa = 1.01$ for $\text{Control}_{\text{GoF}}$, $\kappa = 0.61$ for DMSO-treated; Fig 3.3E and 3.3F).

PIEZO1's effect on coordinated directionality can be further parameterized by measuring the angular deviation, or the variability in velocity direction for all vectors within a PIV vector field. Thus, the range of the angular deviation indicates how coordinated the direction of cellular motion is within an entire monolayer field of view such that a higher angular deviation indicates less coordination. We observe that *Piezo1*-cKO monolayers have a lower average angular deviation value relative to $\text{Control}_{\text{cKO}}$ monolayers, indicating a smaller spread in velocity direction (Fig 3.3G, *left*). This is opposed to *Piezo1*-GoF and Yoda1-treated monolayers which both show a higher angular deviation than the respective controls, further signifying that PIEZO1 activity promotes less directional migration (Fig 3.3G, *middle*, *right*). We note that any difference in the angular deviation between control conditions can likely be attributed to different genetic backgrounds between control conditions.

Recognizing that the synchronized movement of groups of cells during collective migration relies upon the coordination of migration direction across individual cells, we next looked at how PIEZO1 activity affects the distance over which cells align, or correlate, their motion within a monolayer. To do this, we determine how alike the velocity of nearby cells is by calculating the average spatial autocorrelation of velocity vectors, ($C(\Delta r)$), which measures the degree of correlation between velocity vectors of cells at increasing length scales within a monolayer (Fig 3.3H-K). If keratinocytes within a monolayer are migrating together with high directional uniformity we expect a higher autocorrelation value, while a lower autocorrelation value indicates that individual keratinocytes are moving more independently of one another. Therefore, the decay rate of the average spatial autocorrelation curve indicates how coordinated a given cell's direction of motion is to that of another cell located at iteratively increasing distances away (Fig 3.3H-J). Measurement of the spatial autocorrelation in *Piezo1*-cKO and $\text{Control}_{\text{cKO}}$ monolayers illustrate that *Piezo1*-cKO cells show an increase in coordination with cells at greater distances relative to $\text{Control}_{\text{cKO}}$ cells, as indicated by a slower decay of the average *Piezo1*-cKO autocorrelation curve (Fig 3.3H). The length constant, or distance at which the spatial autocorrelation reaches a value of 0.37, was estimated by fitting an exponential curve to our experimental dataset. Calculations of the length constant for *Piezo1*-cKO cells show an increase in coordination by 21.47 μm farther than $\text{Control}_{\text{cKO}}$ (Figs 3.3H and A.10). To further quantify the coordination between nearby cells we measure the spatial autocorrelation values at 150 μm, the distance of a few cell-lengths away. Measurement of local autocorrelation values in *Piezo1*-cKO keratinocytes cells show an increased level of coordination of locomotion with neighboring cells compared to cells in $\text{Control}_{\text{cKO}}$ monolayers (Fig 3.3H and 3.3K). In contrast, both *Piezo1*-GoF and Yoda1-treated monolayers exhibit less coordinated movement with neighboring cells when compared to control cells (Fig 3.3I-K). Length constants in Yoda1-treated and *Piezo1*-GoF cells show a 58.560 μm and 85.54 μm decrease, respectively, in their coordination of motion relative to the respective control monolayers (Figs 3.3I, 3.3J and A.10). Therefore, we find

that PIEZO1 activity disrupts the distance over which cells coordinate their motion during wound closure which inhibits the efficiency of collective migration.

Taken together, our experimental findings support our model predictions that PIEZO1 inhibits coordinated directionality during collective migration. Moreover, we identify that PIEZO1 activity negatively contributes to leader cell formation and the distance by which keratinocytes can coordinate their migration during 2D epithelial sheet migration.

3.6 Discussion

When experimentally measuring persistence during single cell migration assays, we found that both *Piezo1*-GoF and *Piezo1*-cKO keratinocytes have increased persistence (Figure 2 & Figure 2—Figure Supplement 3, [35]), while Yoda1-treatment shows no effect on persistence (Fig A.6). On the other hand, measurement of persistence within collectively migrating cells shows that cells within both *Piezo1*-GoF and Yoda1-treated monolayers show less persistence while cells within *Piezo1*-cKO monolayers show an increase in persistence (Fig 3.2). Taken together, our experimental data indicates that PIEZO1's effect on cell migration persistence is impacted by the contribution of neighboring cells on cell motion. Given that coordinated directionality is the result of cell-cell interactions, while persistence is an inherent characteristic of single cell migration it appears that coordinated directionality plays a key role in contributing towards the efficiency of collective migration experimentally.

During collective migration, the multicellular movement and corresponding polarization of cell clusters is dependent on signal transduction from leader cells to the ensuing follower cells [29, 30, 48]. Leader cells located at the front of these collectives transmit directional cues to follower cells through intercellular mechanical forces and biochemical cues which are communicated via cell adhesion molecules such as E-cadherin [9, 11, 31, 41, 54, 65, 78].

Both theoretical [4, 33] and experimental studies [52] have highlighted the role that cell-cell adhesions play in determining polarization dynamics and motility in multicellular systems. Given our finding that PIEZO1 activity inhibits leader cell formation and coordinated directionality it is possible that PIEZO1 coordinates mechanical forces communicated at cell-cell junctions during the collective migration of keratinocytes; however, further studies would be needed to elucidate this relationship. Consistent with this idea, recent work demonstrates interactions between cadherins and PIEZO1 at cell-cell junctions [89, 16].

The prior work identified that PIEZO1 enrichment and activity induces cell retraction in single keratinocytes as well as along the wound edge of monolayers during *in vitro* scratch assays [35]. Building on these findings, we demonstrate here that monolayer conditions with elevated PIEZO1 activity lack leader cell formations and display reduced coordinated movement of cells. Interestingly, retraction forces generated by follower cells have been seen to promote the formation of leader cells along the wound edge [87]. Thus, it appears that collective migration requires carefully-regulated and coordinated levels of retraction. Consistent with this, Vishwakarma *et al.* found that pharmacologically adjusting the level of actomyosin contractility within monolayers affected the length-scale by which leader cells can correlate their forces such that actomyosin contractility levels inversely correlate with the frequency of leader cell formations [87]. We propose that altered patterns of PIEZO1-induced retractions within a monolayer may inhibit normal signal transduction by leader cells and disrupt cells from moving cohesively during collective migration. Given that these contractile forces could be communicated through cell-cell adhesions, patterns of cell contractility within the monolayer could be modeled to explore this by incorporating a variable adhesion coefficient in a PDE model or using a discrete approach such as a Vertex Model [27, 92].

The identity of downstream molecules underlying PIEZO1-mediated inhibition of keratinocyte migration during reepithelialization remains an open question. The Rho family of small GTPases, which includes the small molecules Rac1 and RhoA, play several roles during collective

migration – regulating cell polarization, intercellular coordination of cellular movement, and leader cell initiation [17, 66, 71, 97]. Previous work has linked PIEZO1-mediated Ca^{2+} influx to impacting both focal adhesion dynamics [63, 53, 94] as well as Rac1 and RhoA levels. PIEZO1's effect on small GTPases has been shown to affect migration in both neural crest cells [13] and cancer cells [43], Cadherin remodeling in lymphatic endothelial cells [64], and macrophage mechanotransduction in iron metabolism [59]. We also observed that total levels of Rac1 and RhoA in healing monolayers are reduced in Yoda1-treated compared to DMSO-treated samples (Fig A.12). While the downregulation of Rho GTPases provides an initial insight into the mechanism underlying PIEZO1-mediated inhibition of leader cells in collective migration, a detailed characterization of this relationship surpasses the scope of work covered within this paper. In future work, we can use mathematical modeling to investigate the relationship between PIEZO1 and Rho GTPases in keratinocyte collective migration by incorporating activator-inhibitor systems for Rho GTPase feedback networks [39] and spatial dynamics [34] into our modeling framework.

Since faster wound healing provides several physiological advantages to an organism, the role of PIEZO1 expression in keratinocytes may seem counterintuitive; however, other groups have reported that too many leader cells results in a disorganized epithelial sheet which affects the quality of wound closure [66]. Recent work examining wound healing in *Drosophila* found that knockout of the *Piezo1* orthologue, *Piezo*, resulted in poorer epithelial patterning and although wounds closed faster, they did so at the expense of epidermal integrity [96]. Therefore, it appears that effective wound healing may require a delicate balance of PIEZO1 activity.

PIEZO1 has been found to influence migration in other cell types, but whether channel activity inhibits or promotes cell migration has been seen to vary [15, 36, 51, 60, 61, 63, 95, 98]. Interestingly, recent studies found that PIEZO1 inhibition suppresses collective migration and results in a decrease in the coordinated directionality of migrating *Xenopus* neural crest

cells [13, 61]. We note that the tissue-context of collective migration is known to engage distinct spatiotemporal signal transduction pathways [26, 29, 48]. Therefore, our seemingly contradictory findings to the observations in neural crest cells could reflect the inherent differences between the migration of neural crest cells and that of keratinocytes during reepithelialization. This highlights the need for studying PIEZO1 mechanotransduction under different biological contexts of cell migration.

Chapter 4

Modeling the impact of heterogeneous PIEZO1 on cell mixtures

4.1 Introduction

In the previous chapter, we have uncovered the inhibitory impact of PIEZO1 activity on coordinated cell directionality within a monolayer. This discovery naturally raises additional questions about the consequences of heterogeneous PIEZO1 activity, for instance within monolayers comprising cells with high and low PIEZO1 activity. To explore this, we expanded the mathematical model presented in Section 2.2.1 to explore the influence of PIEZO1 activity in mixed populations.

In this study, we develop a model considering two distinct cell types, each governed by its own set of equations and parameters, while maintaining effective interaction in the collective migration. We refer to the previously introduced upscaled model (the main model in Section 2.2.1) as the "homogeneous model," and the new model developed in this chapter as the "heterogeneous model." This heterogeneous model is calibrated using experimental

data (Figs 3.1A and A.5; Table 3.1) and numerically simulated to answer several primary questions: Does the presence of heterogeneous populations affect wound healing? Do cells with low PIEZO1 activity always become the leader cells in the mixture? Specifically, we are interested in the roles played by mixture heterogeneity and the interaction between different cell types in wound healing and cell representation at the wound edge. We will also explore whether any predictions from the heterogeneous model can be validated by experiments, and conversely, whether experimental data can inform the model to infer information that is challenging to measure experimentally.

4.2 Model

To develop the model, a monolayer within a field of view (experiments in Fig 1.1C-1.1F) is discretized in two dimensions using a uniform grid of size h. This discretization enables the spatial indices (i, j) to be denoted as $\boldsymbol{x} = \boldsymbol{x}_{i,j} = (ih, jh)$. The cell density of the first cell type, denoted as u cells and represented by the function $u = u(\boldsymbol{x}, t) = u(x, y, t)$, where $\boldsymbol{x} = (x, y)^T$, varies in space and time. At a specific time t, the cell density can be expressed as $u_{i,j} = u(\boldsymbol{x}_{i,j}, t)$. Analogously, the cell density of the second cell type, denoted as v cells, is introduced following the same spatial and temporal representation as $v_{i,j} = v(\boldsymbol{x}_{i,j}, t)$. The experimental field of view is dimensionless and corresponds to a unit square domain: $[0, 1] \times [0, 1] \in \mathbb{R}^2$. By incorporating essential biological components related to reepithelialization (Table 3.2, we formulate discrete master equations for both u cells (Eq. 4.1) and v cells (Eq. 4.2). These equations illustrate the rate of change of cell density over time (Eq. 4.1, 4.2; *left hand side*) in response to the net flux of cells (Eq. 4.1, 4.2; *right-hand side*):

$$\begin{aligned}\frac{\partial u_{i,j}}{\partial t} =& T^{\rightarrow}_{u,i-1,j}u_{i-1,j} + T^{\leftarrow}_{u,i+1,j}u_{i+1,j} + T^{\uparrow}_{u,i,j-1}u_{i,j-1} + T^{\downarrow}_{u,i,j+1}u_{i,j+1} \\ & - (T^{\rightarrow}_{u,i,j} + T^{\leftarrow}_{u,i,j} + T^{\uparrow}_{u,i,j} + T^{\downarrow}_{u,i,j}) \cdot u_{i,j},\end{aligned} \tag{4.1}$$

$$\begin{aligned}\frac{\partial v_{i,j}}{\partial t} =& T^{\rightarrow}_{v,i-1,j}v_{i-1,j} + T^{\leftarrow}_{v,i+1,j}v_{i+1,j} + T^{\uparrow}_{v,i,j-1}v_{i,j-1} + T^{\downarrow}_{v,i,j+1}v_{i,j+1} \\ & - (T^{\rightarrow}_{v,i,j} + T^{\leftarrow}_{v,i,j} + T^{\uparrow}_{v,i,j} + T^{\downarrow}_{v,i,j}) \cdot v_{i,j}.\end{aligned} \tag{4.2}$$

The transitional probabilities per unit time (T's) in this context correspond to probabilities associated with specific directions of cell movement. Specifically, we have $T^{\rightarrow}_{u,i,j}$, $T^{\leftarrow}_{u,i,j}$, $T^{\uparrow}_{u,i,j}$, $T^{\downarrow}_{u,i,j}$ for u cells, and similarly, $T^{\rightarrow}_{v,i,j}$, $T^{\leftarrow}_{v,i,j}$, $T^{\uparrow}_{v,i,j}$, $T^{\downarrow}_{v,i,j}$ for v cells. These probabilities are associated with the transition of cells between adjacent grid points, such as moving from $\boldsymbol{x}_{i,j}$ to $\boldsymbol{x}_{i+1,j}$ for $T^{\rightarrow}_{u,i,j}$ or $T^{\rightarrow}_{v,i,j}$. Each transitional probability takes into account various factors influencing cell behavior, including cell motility, cell-cell adhesion, coordinated directionality, retraction events, and volume filling limitations.

In the discrete master equation governing u cells (refer to Eq. 4.1), the specific transitional probability $T^{\rightarrow}_{u,i,j}$, representing the likelihood of u cells transitioning from $\boldsymbol{x}_{i,j}$ to $\boldsymbol{x}_{i+1,j}$, is defined as the following:

$$\begin{aligned}T^{\rightarrow}_{u,i,j} =& (1 - u_{i+1,j} - v_{i+1,j})(1 - \alpha_{uu}u_{i-1,j} - \alpha_{uv}v_{i-1,j}) \\ & \cdot (1 - \alpha_{uu}u_{i,j+1} - \alpha_{uv}v_{i,j+1})(1 - \alpha_{uu}u_{i,j-1} - \alpha_{uv}v_{i,j-1})(f^{\rightarrow}_{u,i,j} + b^{\rightarrow}_{u,i,j}).\end{aligned} \tag{4.3}$$

The term $(1 - u_{i+1,j} - v_{i+1,j})$ accounts for volume filling effects, representing a constraint on further cell movement into $\boldsymbol{x}_{i+1,j}$ when the cell density at that point has reached its maximum

value. Additionally, the term $(1-\alpha_{uu}u_{i-1,j}-\alpha_{uv}v_{i-1,j})(1-\alpha_{uu}u_{i,j+1}-\alpha_{uv}v_{i,j+1})(1-\alpha_{uu}u_{i,j-1}-\alpha_{uv}v_{i,j-1})$ models cell-cell adhesion from three directions that hinder cell migration [3]. Here, α_{uu} and α_{uv} are adhesion coefficients within the range of $[0, 1]$, where α_{uu} represents cell-cell adhesion between u cells, and α_{uv} represents cell-cell adhesion between u cells and v cells.

In the last term $f^{\rightarrow}_{u,i,j} + b^{\rightarrow}_{u,i,j}$, the vector $f^{\rightarrow}_{u,i,j} = d^{\leftrightarrow}_{u}(u_{i,j} + v_{i,j})/h^2$ models diffusive cell motion for u cells, with $d^{\leftrightarrow}_{u}$ representing the magnitude of u cell movement in the horizontal coordinate direction, and h reflecting the diffusive scaling ($\mathcal{O}(1/h^2)$). The term $b^{\rightarrow}_{u,i,j} = r^{\rightarrow}_{u,i,j}/h$ models u cell movement due to retraction, where $r^{\rightarrow}_{u,i,j}$ accounts for cell retraction, and h reflects the advective scaling ($\mathcal{O}(1/h)$). The diffusive component $f^{\rightarrow}_{u,i,j}$ generates a diffusion flux dependent on the gradient of cell densities u and v, while the advective component $b^{\rightarrow}_{u,i,j}$ results in an advection velocity independent of cell densities, mimicking the influence of retraction events (see Section B.1.1 for details). It's important to note that the total cell density term $(u_{i,j} + v_{i,j})$ in $f^{\rightarrow}_{u,i,j}$ represents the moving front connecting a region of zero cell density (wound) to a region of non-zero density (monolayer), e.g., [91]. Thus, the transitional probability for u cells (Eq. 4.3) can be rewritten as:

$$
\begin{aligned}
T^{\rightarrow}_{u,i,j} = \frac{d^{\leftrightarrow}_{u}}{h^2}(u_{i,j} + v_{i,j})(1 - u_{i+1,j} - v_{i+1,j}) \\
\cdot (1 - \alpha_{uu}u_{i-1,j} - \alpha_{uv}v_{i-1,j})(1 - \alpha_{uu}u_{i,j+1} - \alpha_{uv}v_{i,j+1})(1 - \alpha_{uu}u_{i,j-1} - \alpha_{uv}v_{i,j-1}) \\
+\frac{r^{\rightarrow}_{u,i,j}}{h}(1 - u_{i+1,j} - v_{i+1,j}) \\
\cdot (1 - \alpha_{uu}u_{i-1,j} - \alpha_{uv}v_{i-1,j})(1 - \alpha_{uu}u_{i,j+1} - \alpha_{uv}v_{i,j+1})(1 - \alpha_{uu}u_{i,j-1} - \alpha_{uv}v_{i,j-1})
\end{aligned}
\tag{4.4}
$$

and analogously the corresponding transitional probability for v cells is defined as the following:

$$
\begin{aligned}
T^{\rightarrow}_{v,i,j} = \frac{d^{\leftrightarrow}_v}{h^2}(u_{i,j} + v_{i,j})(1 - u_{i+1,j} - v_{i+1,j}) \\
\cdot (1 - \alpha_{vv} v_{i-1,j} - \alpha_{uv} u_{i-1,j})(1 - \alpha_{vv} v_{i,j+1} - \alpha_{uv} u_{i,j+1})(1 - \alpha_{vv} v_{i,j-1} - \alpha_{uv} u_{i,j-1}) \\
+ \frac{r^{\rightarrow}_{v,i,j}}{h}(1 - u_{i+1,j} - v_{i+1,j}) \\
\cdot (1 - \alpha_{vv} v_{i-1,j} - \alpha_{uv} u_{i-1,j})(1 - \alpha_{vv} v_{i,j+1} - \alpha_{uv} u_{i,j+1})(1 - \alpha_{vv} v_{i,j-1} - \alpha_{uv} u_{i,j-1}).
\end{aligned}
\tag{4.5}
$$

The other transitional probabilities for u cells and v cells, namely $T^{\leftarrow}_{u,i,j}$, $T^{\uparrow}_{u,i,j}$, $T^{\downarrow}_{u,i,j}$ and $T^{\leftarrow}_{v,i,j}$, $T^{\uparrow}_{v,i,j}$, $T^{\downarrow}_{v,i,j}$, follow analogous definitions. Consequently, the continuum limits can be derived by letting $h \to 0$ in the discrete master equations (Eq. 4.1, 4.2), leading to the following system of partial differential equations:

$$
\begin{aligned}
\partial_t u &= \nabla \cdot (\boldsymbol{D}_{11} \nabla u + \boldsymbol{D}_{12} \nabla v + \boldsymbol{R}_1 u), \\
\partial_t v &= \nabla \cdot (\boldsymbol{D}_{21} \nabla u + \boldsymbol{D}_{22} \nabla v + \boldsymbol{R}_2 v),
\end{aligned}
\tag{4.6}
$$

which are diffusion-advection equations where the diffusion, represented by the matrices $\boldsymbol{D}_{11}$, $\boldsymbol{D}_{12}$, $\boldsymbol{D}_{21}$ and $\boldsymbol{D}_{22}$, accounts for cellular locomotion and coordinated directionality. Meanwhile, the advection velocities, denoted as $\boldsymbol{R}_1$ and $\boldsymbol{R}_2$, model the retraction of the leading edge. The diffusion coefficients, or diffusivities, are 2×2 positive definite matrices given by

$$
\begin{aligned}
\boldsymbol{D}_{11} &= d_u \cdot (w_{I,u} \boldsymbol{I} + w_{A,u} \boldsymbol{A}) \cdot D_{11}, \\
\boldsymbol{D}_{12} &= d_u \cdot (w_{I,u} \boldsymbol{I} + w_{A,u} \boldsymbol{A}) \cdot D_{12}, \\
\boldsymbol{D}_{21} &= d_v \cdot (w_{I,v} \boldsymbol{I} + w_{A,v} \boldsymbol{A}) \cdot D_{21}, \\
\boldsymbol{D}_{21} &= d_v \cdot (w_{I,v} \boldsymbol{I} + w_{A,v} \boldsymbol{A}) \cdot D_{21},
\end{aligned}
\tag{4.7}
$$

where non-negative parameters d_u and d_v model cell motilities of u cells and v cells during collective migration. The diffusion decomposition for u cells is expressed as $w_{I,u}\boldsymbol{I} + w_{A,u}\boldsymbol{A}$, and for v cells, it is represented as $w_{I,v}\boldsymbol{I} + w_{A,v}\boldsymbol{A}$. This decomposition combines diffusion isotropy and diffusion anisotropy. In this context, the identity matrix $\boldsymbol{I} = \boldsymbol{I}_2$ captures the randomness in cellular migration, while the matrix $\boldsymbol{A}$ models directed cellular migration. The continuous coefficients related to cell motility (d_u for u cells, d_v for v cells), isotropic strength ($w_{I,u}$ for u cells, $w_{I,v}$ for v cells), and anisotropic strength ($w_{A,u}$ for u cells, $w_{A,v}$ for v cells, representing coordinated directionality) are derived from the discrete level in the following way:

$$\begin{aligned} d_u &= d_u^{\updownarrow}, \quad w_{I,u} = \frac{d_u^{\leftrightarrow}}{d_u^{\updownarrow}}, \quad w_{A,u} = \frac{d_u^{\updownarrow} - d_u^{\leftrightarrow}}{d_u^{\updownarrow}}, \\ d_v &= d_v^{\updownarrow}, \quad w_{I,v} = \frac{d_v^{\leftrightarrow}}{d_v^{\updownarrow}}, \quad w_{A,v} = \frac{d_v^{\updownarrow} - d_v^{\leftrightarrow}}{d_v^{\updownarrow}}. \end{aligned} \tag{4.8}$$

During wound closure, directional cues received from leader cells promote the migration of follower cells into the cell-free space, thus enhancing the probability of cells moving into the wound area. This results in anisotropic diffusion, where cells are more likely to migrate towards the wound gap. Given that cells are directed to migrate towards the wound gap, we assume a larger magnitude of movement in the vertical direction ($d_u^{\updownarrow} \geq d_u^{\leftrightarrow}$ and $d_v^{\updownarrow} \geq d_v^{\leftrightarrow}$) based on our experimental setup, where the scratch wound was created horizontally in the middle of the experimental domain (Fig 1.1C-1.1F). Therefore, the coordinated directionalities $w_{A,u}$ and $w_{A,v}$ are guaranteed to be non-negative and bounded by 1, and the convex weighting relation $w_{I,u} + w_{A,u} = w_{I,v} + w_{A,v} = 1$ naturally holds (Eq. 4.8).

The scalar diffusion coefficients D_{11}, D_{12}, D_{21} and D_{22} in Eq. 4.7 are polynomials of cell densities u and v:

$$
\begin{aligned}
D_{11} =&(1-\alpha_{uu}u-\alpha_{uv}v)^2\cdot(2u+v-(2+6\alpha_{uu}+2\alpha_{uv})uv-(1+7\alpha_{uu})u^2-(1+\alpha_{uv})v^2\\
&+(12\alpha_{uu}+\alpha_{uv})u^2v+(6\alpha_{uu}+2\alpha_{uv})uv^2+6\alpha_{uu}u^3+\alpha_{uv}v^3),\\
D_{12} =&(1-\alpha_{uu}u-\alpha_{uv}v)^2\cdot(1-(\alpha_{uu}+5\alpha_{uv})u-6\alpha_{uv}v+10\alpha_{uv}uv+5\alpha_{uv}u^2+5\alpha_{uv}v^2)\cdot u,\\
D_{21} =&(1-\alpha_{uv}u-\alpha_{vv}v)^2\cdot(1-(\alpha_{vv}+5\alpha_{uv})v-6\alpha_{uv}u+10\alpha_{uv}uv+5\alpha_{uv}u^2+5\alpha_{uv}v^2)\cdot v,\\
D_{22} =&(1-\alpha_{uv}u-\alpha_{vv}v)^2\cdot(u+2v-(2+6\alpha_{vv}+2\alpha_{uv})uv-(1+7\alpha_{vv})v^2-(1+\alpha_{uv})u^2\\
&+(12\alpha_{vv}+\alpha_{uv})uv^2+(6\alpha_{vv}+2\alpha_{uv})u^2v+6\alpha_{vv}v^3+\alpha_{uv}u^3),
\end{aligned}
\tag{4.9}
$$

which are derived through a multi-scale modeling process from the scaled cell density $(u_{i,j}+v_{i,j})/h^2$, cell-cell adhesion (e.g., $(1-\alpha_{uu}u_{i-1,j}-\alpha_{uv}v_{i-1,j})(1-\alpha_{uu}u_{i,j+1}-\alpha_{uv}v_{i,j+1})(1-\alpha_{uu}u_{i,j-1}-\alpha_{uv}v_{i,j-1})$ in $T^{\rightarrow}_{u,i,j}$) and volume filling (e.g., $(1-u_{i+1,j}-v_{i+1,j})$ in $T^{\rightarrow}_{u,i,j}$). The adhesion coefficients (α_{uu} and α_{vv}), which lie in the range $[0,1]$, models the adhesion forces between adjacent cells, with a larger value corresponding to larger adhesion forces. In our study, we generalize the parameter α_{uv} to include negative values, thereby accounting for possible repulsive interactions in additional to cell-cell adhesion between different cell types (detailed in Section 4.3.2). Volume-filling limitations to cell movement are also modeled in scalar diffusivities (Eq. 4.9) to hinder cells from migrating into a cell-dense area.

Similar to the derivation of diffusion, the retraction vectors $\boldsymbol{R}_1$ for u cells and $\boldsymbol{R}_2$ for v cells are derived from the $\mathcal{O}(1/h)$ components of the discrete transitional probabilities (Eq. 4.4 for u cells and Eq. 4.5 for v cells) by taking the limit $h\to 0$:

$$
\begin{aligned}
\boldsymbol{R}_1 &= (1-u-v)(1-\alpha_{uu}u-\alpha_{uv}v)^3\cdot(\Delta r_1^{\leftrightarrow},\Delta r_1^{\updownarrow})^T,\\
\boldsymbol{R}_2 &= (1-u-v)(1-\alpha_{uv}u-\alpha_{vv}v)^3\cdot(\Delta r_2^{\leftrightarrow},\Delta r_2^{\updownarrow})^T,
\end{aligned}
\tag{4.10}
$$

where $(1-u-v)$ and $(1-\alpha_{uu}u-\alpha_{uv}v)^3$ represent the effects of volume filling and cell-cell adhesion, respectively. The retraction magnitude and directions are modeled phenomenologically in Δr's ($\Delta r_1^{\leftrightarrow}$, $\Delta r_1^{\updownarrow}$, $\Delta r_2^{\leftrightarrow}$, and $\Delta r_2^{\updownarrow}$) as being localized in space and time, motivated by prior experimental studies [35]. In particular, we assume:

1. Retraction occurs locally along the wound edge. This means only a part of wound edge cells are involved in retraction events at each time, while the rest of the cells on the edge and cells within the monolayer away from the edge just migrate by diffusion.

2. Retraction occurs intermittently in time. This means no retraction event is endless, i.e., no regions retract indefinitely. Hence at a wound edge point, there is a finite interval of duration time for each retraction event, and there is also a finite interval of time between two consecutive retraction events.

Following the localization assumptions (1) and (2), a choice for Δr's is given in the following form to simulate retraction that occurs at random times and locations on each side of the wound edge:

$$\Delta r_1^{\leftrightarrow} = \Delta r_1^{\updownarrow} = \Delta r_2^{\leftrightarrow} = \Delta r_2^{\updownarrow} = \tilde{H}(\gamma-u-v)\cdot\sum_{i=1}^{\infty} s_i\cdot\tilde{\mathbb{1}}_{[\tau_i,\tau_i+\mathcal{T}_i^r)}(t)\cdot\tilde{\mathbb{1}}_{\Omega_i}(\boldsymbol{x}), \tag{4.11}$$

where the smoothed Heaviside function $\tilde{H}$, smoothed indicator function $\tilde{\mathbb{1}}$, strength for the ith retraction s_i, starting moment for the ith retraction τ_i, duration for the ith retraction $\mathcal{T}_i^r$ and region for the ith retraction Ω_i are all inherited from our previous model, defined in the same way as in Eq. 2.10. In such construction, Δr's are designed to model retractions such that cell movement would be governed by a diffusion-advection equation that guides the migrating cells in the retraction region near the wound edge:

$$\begin{aligned}
\partial_t u &= \nabla \cdot (\boldsymbol{D}_{11} \nabla u + \boldsymbol{D}_{12} \nabla v) + \nabla \cdot (\boldsymbol{s}_u (1-u-v)(1-\alpha_{uu} u - \alpha_{uv} v)^3 u), \\
\partial_t v &= \nabla \cdot (\boldsymbol{D}_{21} \nabla u + \boldsymbol{D}_{22} \nabla v) + \nabla \cdot (\boldsymbol{s}_v (1-u-v)(1-\alpha_{uv} u - \alpha_{vv} v)^3 v),
\end{aligned} \tag{4.12}$$

where diffusivities ($\boldsymbol{D}_{11}$, $\boldsymbol{D}_{12}$, $\boldsymbol{D}_{21}$ and $\boldsymbol{D}_{22}$) are given in Eq. 4.7. In $\boldsymbol{s}_u = (s_u, s_u)^T/\sqrt{2}$ and $\boldsymbol{s}_v = (s_v, s_v)^T/\sqrt{2}$, the retraction strengths s_u and s_v regulate the magnitude of advection velocities for u cells and v cells, respectively. On the other hand, cells far from the wound edge (i.e., interior of the monolayer) migrate following a simple diffusion equation

$$\begin{aligned}
\partial_t u &= \nabla \cdot (\boldsymbol{D}_{11} \nabla u + \boldsymbol{D}_{12} \nabla v), \\
\partial_t v &= \nabla \cdot (\boldsymbol{D}_{21} \nabla u + \boldsymbol{D}_{22} \nabla v)
\end{aligned} \tag{4.13}$$

with the same diffusivities (Eq. 4.7). In such construction of $\Delta r_1^{\leftrightarrow}$ and $\Delta r_1^{\updownarrow}$, three key parameters related to retraction are involved: (1) $\mu_{s,u}$ denotes the mean strength of retraction forces on u cells, (2) $\mu_{r,u}$ represents the mean duration for a retraction event to occur on u cells, and (3) $\mu_{nr,u}$ indicates the mean idle duration between two consecutive retraction events on u cells. Similarly, $\mu_{s,v}$, $\mu_{r,v}$, and $\mu_{nr,v}$ are defined analogously in $\Delta r_2^{\leftrightarrow}$ and $\Delta r_2^{\updownarrow}$ to characterize retraction on v cells.

As we focus on modeling a specific subset of the observation domain in the experiment, e.g., the region near the wound edges instead of the entire experimental domain, we establish the following boundary conditions at the computational domain boundaries:

$$
\begin{aligned}
u(x,0,t) &= \tilde{p}_u \cdot g_0(x,t), \quad u(x,1,t) = \tilde{p}_u \cdot g_1(x,t), \\
v(x,0,t) &= \tilde{p}_v \cdot g_0(x,t), \quad v(x,1,t) = \tilde{p}_v \cdot g_1(x,t), \\
\frac{\partial u(0,y,t)}{\partial x} &= \frac{\partial u(1,y,t)}{\partial x} = \frac{\partial v(0,y,t)}{\partial x} = \frac{\partial v(1,y,t)}{\partial x} = 0.
\end{aligned} \tag{4.14}
$$

Horizontally, at the top and bottom of the domain, time-dependent Dirichlet boundary conditions at $\boldsymbol{x} = (x, 0)$ and $\boldsymbol{x} = (x, 1)$ allocate total cell densities to the boundary points based on functions g_0 and g_1 (the same as Eq. 2.17, detailed in Section 2.3.1). These functions simulate the mixing of cells flowing into the observation domain from the monolayer, roughly perpendicular to the wound edge. The random variable $\tilde{p}_v$ represents the percentage of v cells, while $\tilde{p}_u = 1 - \tilde{p}_v$ represents the percentage of u cells. To incorporate randomness, we assume:

$$
\tilde{p}_v \sim \mathcal{N}(p_v, \sigma_v^2), \tag{4.15}
$$

where $\mathcal{N}(p_v, \sigma_v^2)$ denotes a normal distribution with mean p_v and standard deviation σ_v. Vertically, on the left and right sides of the domain, no-flux (Neumann) boundary conditions are employed to approximate a net balance of cell influx and efflux into the observation domain, aligning with the experimental setup. Thereafter, model parameter p_v is referred to as the source cell percentage for v cells.

The initial condition for the governing equations (Eq. 4.6) is generated by setting the total cell density $u + v$ at $t = 0$ to be the same as $\rho(\boldsymbol{x}, 0)$, which is the initial condition from our previous model (detailed in Section 2.3.2). This initial monolayer consists of p_u percentage of u cells and p_v percentage of v cells:

$$u(\boldsymbol{x},0) = p_u \cdot \rho(\boldsymbol{x},0), \quad v(\boldsymbol{x},0) = p_v \cdot \rho(\boldsymbol{x},0). \tag{4.16}$$

Summarizing, this new model builds on parameters inherited from the upscaled model in Section 2.2.1, emphasizing the interactions between different cell types (α_{uv}) and the mixture heterogeneity characterized by the percentage of v source cells (p_v). The derived governing equations (Eq. 4.6) are nonlinear stochastic PDEs, with stochasticity arising from the random coefficients.

4.3 Methods

4.3.1 Numerical implementation

Following the same framework as our previous model with homogeneous cell type (Fig 2.1A, *right*), the heterogeneous collective cell migration is also simulated within a square domain, which is defined by two opposite sides with zero-flux Neumann boundaries (left and right) and two opposite sides with randomized Dirichlet boundaries (up and down). Initially, cells are uniformly mixed within the simulation domain, consisting of a p_v percentage of v cells and consequently, a $p_u = 1 - p_v$ percentage of u cells. When the simulations begin ($t > 0$), source cells migrate into the domain from the randomized Dirichlet boundaries, exhibiting stochastic influx and stochastic proportions of cells (Eq. 4.14).

To solve the governing equations (Eq. 4.6), we first perform a forward time discretization (with size Δt) on the left-hand side of each equation. Here, $\partial_t u$ and $\partial_t v$ are discretized using the schemes $(u(\boldsymbol{x}_{i,j}, t+\Delta t) - u(\boldsymbol{x}_{i,j}, t))/\Delta t$ and $(v(\boldsymbol{x}_{i,j}, t+\Delta t) - v(\boldsymbol{x}_{i,j}, t))/\Delta t$, respectively. For the spatial discretization (right-hand side), the transitional probabilities for u cells and v

cells are shown to be separable in the discrete model (Eq. 4.4 and Eq. 4.5). This allows us to address the diffusion part and advection part separately for each equation. For the diffusion part, a natural discretization is directly given by the discrete model (e.g., centered finite differences). Meanwhile, for the advection part, we employ a 2nd order weighted essentially non-oscillatory (WENO) method [38, 57] to discretize the equation. Therefore, we utilize this explicit finite difference scheme to iteratively update the cell density of u cells and v cells at the nth time step ($u_{i,j}^n$ and $v_{i,j}^n$) over the simulation domain $[0,1] \times [0,1]$ until the total cell mixture $u + v$ closes the wound.

In the numerical implementation, the governing equations for u and v cells (Eq. 4.6) must be solved synchronously at each time step to update the cell density values because of their mutual dependency. In the diffusion part, the volume filling effect for each cell type depends on the total cell density $u + v$, and the interaction between u cells and v cells is determined by their respective counterparts in their own equations. While the mutual dependency in the advection parts of the governing equations for u and v cells may not be as obvious as in the diffusion part, since retraction is modeled to be applied independently to each cell type, it is important to note that the retraction region near the wound edge, where each type of cell experiences retraction, is determined by the total cell density $u + v$ (Eq. 4.11 in Section B.1.1).

4.3.2 Model parameter study

Simulations of wound closure provide insight into how individual model parameters affect the wound closure process. Through a parameter study, we can explore the effects of model parameters on the rate of normalized wound closure, which is influenced by PIEZO1 activity during keratinocyte reepithelialization and can be directly measured and compared to experimental data. Our parameter study involves altering individual model parameters one

at a time while holding the remaining parameters at their base values (Fig B.11) to observe how such variations affect wound closure and edge roughness.

Since the scope of this paper is on heterogeneity, and our previous chapters have extensively explored model parameters among cells of the same type, we primarily focus on two model parameters: interaction coefficient α_{uv}, which captures the interaction between different types of cells, and the source percentage for v cells p_v, which captures the heterogeneity of the mixture. Specifically, while α_{uv} was originally defined alongside α_{uu} and α_{vv} to model the adhesion between u and v cells, we can extend its definition. By allowing α_{uv} to take negative values, it can more broadly represent cell-cell interactions between u and v cells, with $\alpha_{uv} > 0$ indicating adhesion and $\alpha_{uv} < 0$ indicating repulsion. The parameter p_v represents the percentage of v cells in the source cells, indicating that the initial cell population consists of v cells in the proportion of p_v at $t = 0$, and that cells entering the observation domain from the inner monolayer maintain this proportion in average when $t > 0$. Thus, p_v models the heterogeneity of the mixture, where $p_v = 0.5$ results in the most heterogeneous mixture, and higher values of p_v indicate a greater proportion of v cells compared to u cells, and vice versa.

4.3.3 Model calibration with experimental data

By integrating model parameters derived from experimental data, we can calibrate the mathematical model used in simulations. To achieve this, we expanded upon analyses conducted on single migrating keratinocytes in previous studies [35, 37]. This allowed us to compile an experimental dataset characterizing PIEZO1's impact on cell motility and retraction processes, including retraction duration, inter-retraction duration, and cell retraction strength, across all experimental conditions (*Piezo1*-cKO, *Piezo1*-GoF, Yoda1-treatment, and their respective controls). Cell motility parameters were determined by extracting cell speed in-

formation from single-cell tracking experiments conducted previously [35, 37]. On the other hand, parameters related to retraction processes were obtained by combining two experimental analysis methods employed in previous studies [35]: (1) kymographs, which visually represent retraction and inter-retraction durations of the leading edge of migrating keratinocytes, and (2) a cell protrusion quantification software, ADAPT [6], which quantifies the strength of retraction events at the leading edge. This dataset, referred to as the "Single Cell Migration" dataset (Figs 3.1A and A.5; Table 3.1), allowed us to calibrate our model parameters based on experimental measurements, enabling us to make experimentally relevant predictions regarding PIEZO1's influence on wound closure behavior.

To calibrate our model, we established a respective simulation control for each experimental condition (*Piezo1*-cKO, *Piezo1*-GoF, and Yoda1-treated) by setting the values of model parameters to baseline values. This baseline configuration ensured that the frequency of retraction matched that of the corresponding experimental control condition (see Fig B.11 for the full list of model parameters and their baseline values). For each experimental condition, the model parameters related to retraction (retraction duration, inter-retraction duration, and retraction strength) and cell motility were adjusted relative to the control condition based on the same proportions observed experimentally. Specifically, changes in mean retraction and inter-retraction durations ($\mu_{r,u}$, $\mu_{nr,u}$ for u cells or $\mu_{r,v}$, $\mu_{nr,v}$ for v cells), cell motility (d_u or d_v), and mean retraction strength ($\mu_{s,u}$ or $\mu_{s,v}$) were adjusted proportionally in the model based on experimentally observed alterations relative to the control condition. As established in the previous chapter, coordinated directionality in *Piezo1*-GoF cells must be increased compared to $\text{Control}_{\text{GoF}}$ to align with experimental observations. We maintained this essential calibration and kept other parameters fixed at their baseline values (Fig B.11), unless specific further variations were required to study their effects.

In collective cell migration with heterogeneous PIEZO1 activity, mixing scenarios include: (1) $\text{Control}_{\text{cKO}}$ and *Piezo1*-cKO, (2) $\text{Control}_{\text{GoF}}$ and *Piezo1*-GoF, and (3) *Piezo1*-cKO and

Yoda1-treated cells. To simulate the collective migration of cells in each PIEZO1 phenotype, we calibrate model parameters using experimental data correspondingly (detailed in Section 4.3.3). Once the PIEZO1 phenotypes for u and v cells are specified in the model, the values for these parameters are designated and remain unchanged throughout the simulation.

It is legitimate to consider the mixture of *Piezo1*-cKO and Yoda1-treated cells, which does not involve any wild-type control, because their respective control cases ($\text{Control}_{\text{cKO}}$ and DMSO-treated) are exactly the same type of cells in experiments [35]. Moreover, this mixture is experimentally feasible by simply treating Yoda1 on a mixture of $\text{Control}_{\text{cKO}}$ and *Piezo1*-cKO cells. Since *Piezo1*-cKO cells lack PIEZO1 channels, they remain unaffected by Yoda1 treatment, while their wild-type control counterparts in the mixture convert into Yoda1-treated samples. In our study, *Piezo1*-GoF is not considered for mixing with any other cell types except its own control. This is because $\text{Control}_{\text{GoF}}$ utilizes different experimental data for model calibration compared to other controls, as $\text{Control}_{\text{GoF}}$ cells are experimentally distinct from other control cell types. The mixture of DMSO-treated and Yoda1-treated cells is experimentally unattainable, thus we only present the relevant results concerning this mixture in the appendix (Fig B.10).

4.4 Results

4.4.1 The impact of cell-cell interaction on wound closure is amplified by the mixture heterogeneity

When mixing u and v cells, if the interaction coefficient $\alpha_{uv} < 0$, the cell-cell interaction between u and v cells shifts from adhering to expelling, indicating a tendency to avoid attachment. To enforce this repelling interaction between u and v cells, we set $\alpha_{uv} = -0.4$ and observe the simulated wound closure process under equal proportions of u and v cells,

compared to simulations with solely u cells or solely v cells. This adjustment is achieved by varying the source cell percentage for v cells p_v: $p_v = 0$ represents solely u cells, $p_v = 1$ represents solely v cells, and $p_v = 0.5$ represents a roughly equal mixture of both cell types. In the case of mixing $\text{Control}_{\text{cKO}}$ (u cells) and *Piezo1*-cKO (v cells), we observed that solely *Piezo1*-cKO cells ($p_v = 1$) close the wound faster than solely $\text{Control}_{\text{cKO}}$ cells ($p_v = 0$), consistent with experimental results (Fig 4.1A). Interestingly, the wound closure is even faster when these cell types are mixed, surpassing the closure rate of any individual cell type (Fig 4.1A). With the expelling cell-cell interaction ($\alpha_{uv} = -0.4$), this phenomenon persists across other cell type mixtures (Fig 4.1C and 4.1D), where the mixed cell population closes the wound more rapidly than any individual cell type.

To comprehensively investigate the impact of cell-cell interactions on normalized wound closure in cell mixtures, we conducted model simulations across varying proportions of *Piezo1*-cKO source cell percentage p_v and different interaction coefficient values α_{uv}. Subsequently, we plotted the average rate of wound closure obtained from multiple simulations (Fig 4.1B, 4.1D, and 4.1F). Here, we maintained a fixed adhesion between cells of the same type ($\alpha_{uu} = \alpha_{vv} = 0.2$), with further details on the parameter study involving changes in α_{uu} and α_{vv} provided in the appendix (Section B.1.2).

In the mixture of $\text{Control}_{\text{cKO}}$ and *Piezo1*-cKO cells, the plot exhibits a sloped spindle pattern (Fig 4.1B), with the rate of wound closure appearing higher at the right spindle pole ($p_v = 1$) compared to the left spindle pole ($p_v = 0$). This observation aligns with experimental evidence indicating that *Piezo1*-cKO cells demonstrate faster wound closure compared to $\text{Control}_{\text{cKO}}$ cells. The plotted lines can be categorized into three types based on their convexity:

1. When the interaction coefficient is set to $\alpha_{uv} = \alpha_{uu} = \alpha_{vv} = 0.2$, the adhesion effects between any cells are indistinguishable. As a result, the wound closure for mixed cell

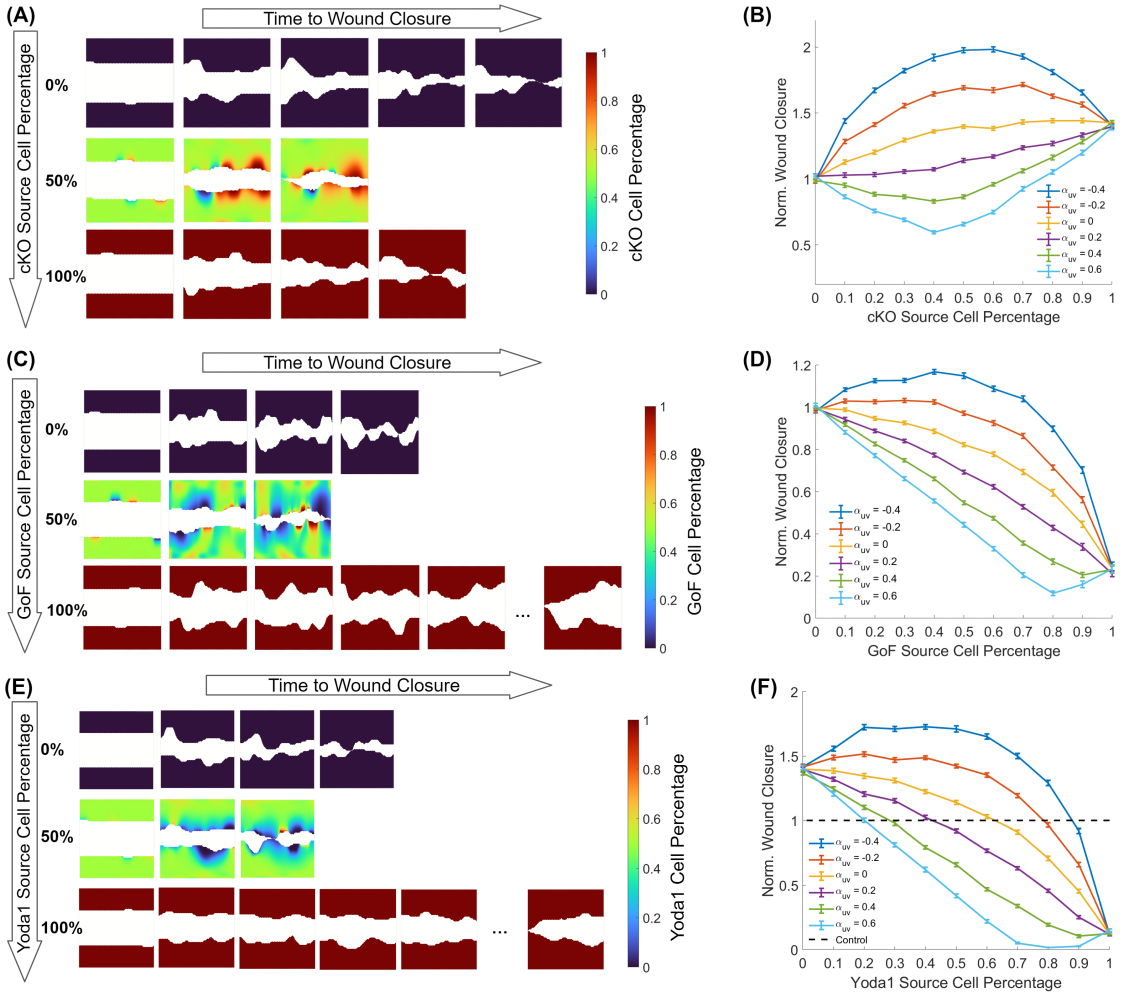

Figure 4.1: **The impact of cell-cell interaction on wound closure is amplified by the mixture heterogeneity.** **(A)** Mixing mutually repulsive cells accelerate wound closure. Snapshot of wound healing progression for a mixture of $\text{Control}_{\text{cKO}}$ (u cells) and *Piezo1*-cKO (v cells) captured at equidistant time intervals, under varied source cell conditions with *Piezo1*-cKO (v cells) percentages of 0% (*top*, i.e., solely $\text{Control}_{\text{cKO}}$), 50% (*middle*), and 100% (*bottom*, i.e., solely *Piezo1*-cKO). Colored areas represent cell monolayers, with colors indicating the spatial distribution of *Piezo1*-cKO (v cells) percentage, while plain white areas denote cell-free space. The interaction coefficient $\alpha_{uv} = -0.4$. **(B)** Line graphs illustrate the mean of 100 simulation results, displaying the normalized wound closure versus the *Piezo1*-cKO source cell percentage. Error bars indicate the standard error of the mean. The various colored lines denote different interaction coefficient values (α_{uv}). **(C) and (D)** Depict similar scenarios to (A) and (B), but involving mixtures of *Piezo1*-GoF (v cells) with their respective wild-type control (u cells). **(E) and (F)** Also akin to (A) and (B), but featuring mixtures of *Piezo1*-cKO (u cells) and Yoda1-treated cells (v cells). The dashed line in (F) denotes the unit normalized wound closure, representing the rate of wound closure of wild-type control.

migration represents a simple interpolation between pure $\text{Control}_{\text{cKO}}$ (left spindle pole in Fig 4.1B) and pure *Piezo1*-cKO (right spindle pole in Fig 4.1B), demonstrating a monotonic increasing trend from slower closure in $\text{Control}_{\text{cKO}}$ to faster closure in *Piezo1*-cKO (the purple line in Fig 4.1B).

2. When the interaction coefficient $\alpha_{uv} > 0.2$, the hindering adhesion effect between different cell types α_{uv} becomes stronger than the adhesion effect within the same cell type (α_{uu} and α_{vv}). In this scenario, when the heterogeneity of the mixture is higher (e.g., 50% $\text{Control}_{\text{cKO}}$ mixed with 50% *Piezo1*-cKO), the role played by interaction coefficient becomes more significant, resulting in slower collective cell migration and displaying a convex "U-shaped" line (e.g., the bottom line in light blue in Fig 4.1B).

3. Conversely, when the interaction coefficient $\alpha_{uv} < 0.2$, cells are more likely to migrate away from the adhesion between different cell types compared to the adhesion between the same cell types. The expelling effect occurs when $\alpha_{uv} < 0$ becomes negative, causing cell-cell interaction between different cell types to propel cells toward cell-free regions. Consequently, the faster wound closure rate in the mixture results in a concave up "bridge-shaped" line (e.g., the top line in dark blue in Fig 4.1B).

We noticed that the influence of cell-cell interaction on wound closure rate is more pronounced in the mixture with higher heterogeneity, i.e., when the proportion of *Piezo1*-cKO cells (p_v) approaches 0.5. This heightened impact arises because the effect of interaction coefficient (α_{uv}) on one cell type cannot act independently; it also relies on the cell density of the other cell type in the mixture. In our model (Eq. 4.9 and Eq. 4.10), u cell migration is impeded by interaction coefficient through the term $1-\alpha_{uu}u-\alpha_{uv}v$, and similarly for v cells through $1-\alpha_{vv}v-\alpha_{uv}u$. Consequently, if the percentage of v cells (p_v) is large, indicating that its counterpart $p_u = 1 - p_v$ is too small to effectively transmit interaction coefficient to influence its migration. Conversely, if the percentage of v cells is small, even though a large number of u cells can influence its migration through interaction coefficient, the proportion

of v cells is too small to significantly impact the overall mixture cell migration. Therefore, when they are mixed in near-equal proportions, the modulation of interaction coefficient α_{uv} in wound closure reaches its maximal effect.

Similarly, the mixture of $\text{Control}_{\text{GoF}}$ and *Piezo1*-GoF also displays an inclined spindle pattern when plotting the normalized wound closure with respect to the *Piezo1*-GoF source cell percentage p_v under different interaction coefficient α_{uv} (Fig 4.1D). However, in this case, the inclination of the spindle is from the higher left spindle pole ($\text{Control}_{\text{GoF}}$) sloping to the lower right spindle pole (*Piezo1*-GoF), consistent with the experimental observation indicating that *Piezo1*-GoF cells close the wound slower than its control. Similarly to Fig 4.1B, the mixture under repulsive cell-cell interaction when $\alpha_{uv} < 0$ also demonstrates an acceleration in wound closure, while a slower rate of wound closure is observed in the mixture under high interaction coefficient (α_{uv}). It's noteworthy that the fastest and slowest rates of wound closure do not necessarily occur in the exact even mixture ($p_v = 0.5$), as the extremes are influenced by both the PIEZO1 phenotype and heterogeneity. By isolating the effect of the PIEZO1 phenotype through mixing cells with the same set of model parameters (e.g., mixing $\text{Control}_{\text{GoF}}$ with $\text{Control}_{\text{GoF}}$ itself), the spindle would exhibit a symmetric pattern where the fastest and slowest rates of wound closure are achieved in the even mixture when $p_v = 0.5$ (Fig B.3A and B.3B, detailed in the appendix in Section B.1.3). The mixture of *Piezo1*-cKO and Yoda1-treated cells resembles the case of mixing $\text{Control}_{\text{GoF}}$ and *Piezo1*-GoF, but the spindle pattern shows a stronger inclination (Fig 4.1F).

4.4.2 PIEZO1 activity down-regulates the edge cell representation

Our study in the preceding chapter revealed PIEZO1's suppression on leader cell formation. Thus, we hypothesized that in cell mixtures with varying levels of PIEZO1 activity, the cell type with lower PIEZO1 activity would more likely constitute the leader cells. To isolate the

influence of cell-cell adhesion, we fix $\alpha_{uv} = \alpha_{uu} = \alpha_{vv} = 0.2$ at this point. In the mixture of $\text{Control}_{\text{cKO}}$ (u cells) and *Piezo1*-cKO (v cells), we varied the *Piezo1*-cKO source cell percentage (p_v), and we observed that cases with a higher *Piezo1*-cKO percentage displayed faster wound closure (Fig 4.2A), consistent with the experiment where homogeneous *Piezo1*-cKO monolayers closed wounds faster. Additionally, *Piezo1*-cKO cells tended to advance to the front and aggregate around the wound edge (Fig 4.2A, red color near the wound), aligning with our hypothesis. Conversely, in mixing *Piezo1*-GoF (v cells) with its control (u cells), a higher percentage of *Piezo1*-GoF cells (p_v) resulted in slower wound closure (Fig 4.2C), consistent with the experimental results showing slower wound closure for *Piezo1*-GoF compared to its control. Importantly, $\text{Control}_{\text{GoF}}$ cells tended to advance to the front and comprise the wound edge cells (Fig 4.2C, blue color near the wound), in line with our hypothesis. Similarly, in the mixture of *Piezo1*-cKO and Yoda1-treated cells, we observed that *Piezo1*-cKO cells, as the component with lower PIEZO1 activity, tended to advance and aggregate near the wound (Fig 4.2E, blue color near the wound).

Quantitatively restating our hypothesis, we anticipate a higher proportion of cells with lower PIEZO1 activity to be located near the wound edge. The term "wound edge cells" pertains to cells situated near the wound edge, where the total density satisfies the condition $0 < u+v < \gamma_{\text{edge}}$. To determine the threshold γ_{edge} for identifying wound edge cells, we conducted simulations by mixing $\text{Control}_{\text{cKO}}$ and $\text{Control}_{\text{cKO}}$ rather than mixing $\text{Control}_{\text{cKO}}$ and *Piezo1*-cKO. That is, both u and v cells have the identical phenotype and parameters drawn from the $\text{Control}_{\text{cKO}}$ experimental data. In this case, for any fraction of v in the entire monolayer, we expect to observe the same fraction of v cells in wound edge cells where $u+v < \gamma_{\text{edge}}$. The minimal γ_{edge} that satisfies this condition is the threshold we sought, and it was determined to be 0.2. For further details regarding this threshold, refer to the appendix in Section B.1.4.

To provide further quantitative evidence supporting our hypothesis, we conducted simulations similar to those in Fig 4.2A, but repeated them 100 times for each p_v value (20%,

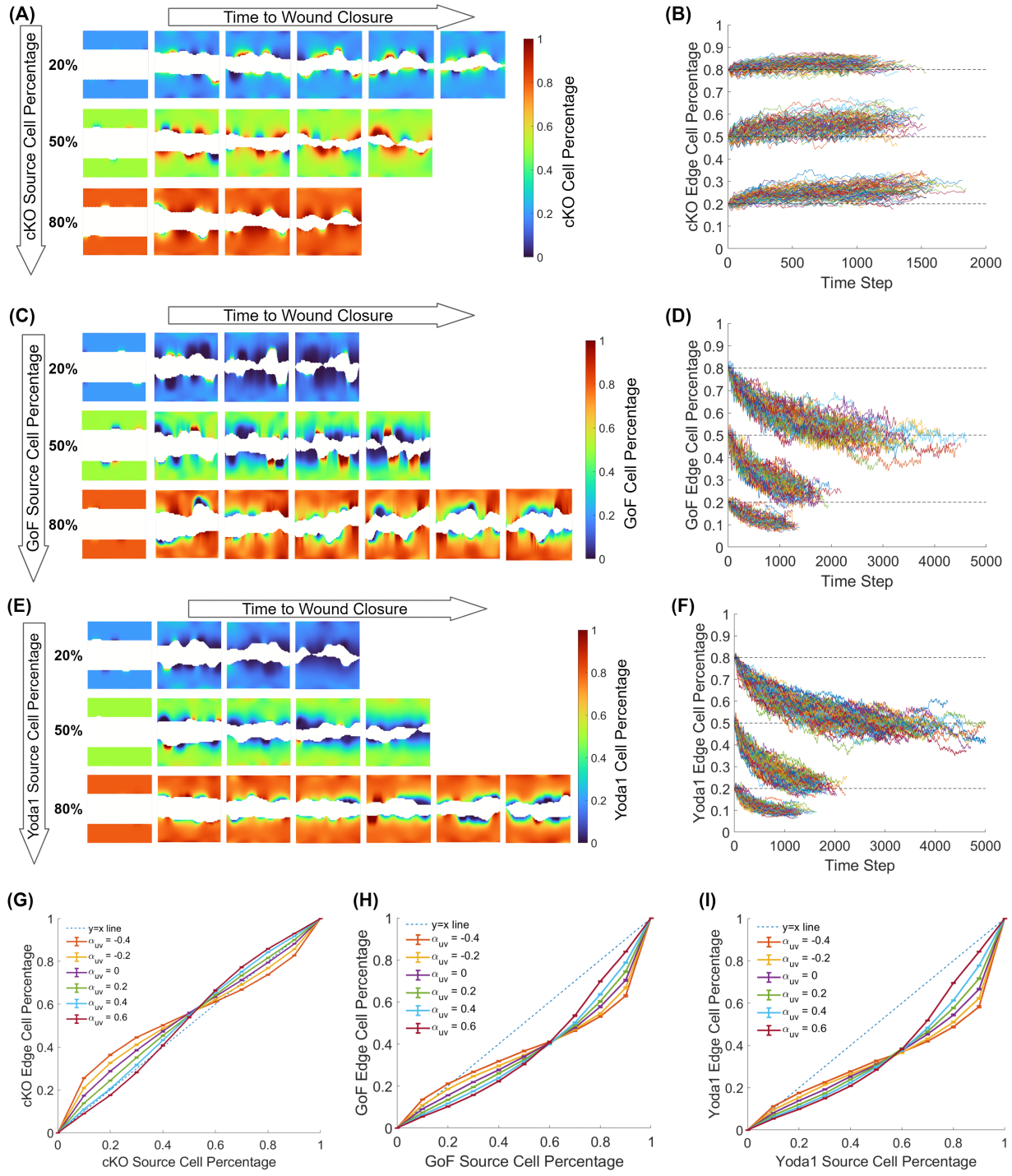

Figure 4.2: **The distribution of edge cells correlates with the level of PIEZO1 activity.**

Figure 4.2 continued on next page

Figure 4.2 continued
(A) Snapshot of wound healing progression for a mixture of $\text{Control}_{\text{cKO}}$ (u cells) and *Piezo1*-cKO (v cells) captured at equidistant time intervals, under varied *Piezo1*-cKO (v cells) source cell percentage of 20% (*top*), 50% (*middle*), and 80% (*bottom*). Colored areas represent cell monolayers, with colors indicating the spatial distribution of *Piezo1*-cKO (v cells) percentage, while plain white areas denote cell-free space. **(B)** Line graphs within each cluster represent 100 individual tracks (300 total trajectories in the figure), demonstrating the evolution of *Piezo1*-cKO (v cells) percentage in edge cells over simulation time steps during wound closure. The clusters correspond to distinct source cell conditions, with *Piezo1*-cKO (v cells) percentages set at 20% (*bottom* cluster), 50% (*middle* cluster), and 80% (*top* cluster), aligning with the respective rows of snapshots in (A). These levels are indicated by black dashed lines. **(C) and (D)** Depict similar scenarios to (A) and (B), but involving mixtures of *Piezo1*-GoF (v cells) with their respective wild-type control (u cells). **(E) and (F)** Also akin to (A) and (B), but featuring mixtures of *Piezo1*-cKO (u cells) and Yoda1-treated cells (v cells). **(G)** Line graphs illustrate the mean of 100 simulation results, displaying the percentage of *Piezo1*-cKO (v cells) cells in edge cells versus the percentage in source cells. The various colored lines denote different interaction coefficient values (α_{uv}), and error bars indicate the standard error of the mean. **(H)** Same as for (G) but for mixing $\text{Control}_{\text{GoF}}$ (u cells) and *Piezo1*-GoF (v cells). **(I)** Also similar to (G), but in the case of mixing *Piezo1*-cKO (u cells) and Yoda1-treated (v cells).

50%, and 80%). We measured the percentage of *Piezo1*-cKO cells in edge cells at every time step during the wound closure process for each simulation, then plotted all trajectories together in a single figure (Fig 4.2B). Each trajectory represents an individual simulation, grouped into three clusters corresponding to $p_v = 0.2$, 0.5, and 0.8. In each cluster, the majority of trajectories are situated above their respective p_v line (black dashed line in Fig 4.2B). This indicates that *Piezo1*-cKO cells, with lower PIEZO1 activity in the mixture, are over-represented at the wound edge. Conversely, when plotting the trajectories of *Piezo1*-GoF cell percentage in edge cells over simulation time steps for mixing with $\text{Control}_{\text{GoF}}$, we observed a downward trend for each cluster, with the majority of trajectories falling below their corresponding p_v value (Fig 4.2D). This suggests that *Piezo1*-GoF cells tend to be under-represented at the wound edge. A similar under-representative trend of cells with higher PIEZO1 activity at the wound edge was observed in the mixture of *Piezo1*-cKO and Yoda1-treated cells (Fig 4.2F).

To gain a more comprehensive understanding of the relationship between the distribution of edge cells and the level of PIEZO1 activity, we calculated the average percentage of v cells among all wound edge cells by varying not only p_v but also the interaction coefficient α_{uv}. We then plotted this average value over p_v under different values of α_{uv}, as depicted in Fig 4.2G, 4.2H, and 4.2I. The results confirm that cells with lower PIEZO1 activity in the mixture (e.g., *Piezo1*-cKO) are over-represented at the wound edge, as most lines are situated above the $y = x$ line (Fig 4.2G). Conversely, cells with higher PIEZO1 activity (e.g., *Piezo1*-GoF and Yoda1-treated) are under-represented at the wound edge, as indicated by most lines falling below the $y = x$ line (Fig 4.2H and 4.2I).

It's worth noting the "double spindle" pattern observed in Fig 4.2G, 4.2H, and 4.2I, which is caused by the combined effect of p_v and α_{uv}, rather than by the PIEZO1 phenotype itself. For example, when $p_v < 0.5$ and $\alpha_{uv} < 0$, the migration of v cells is effectively promoted by the repulsive cell-cell interaction ($\alpha_{uv} < 0$) from a large proportion of u cells ($p_u = 1 - p_v > 0.5$). This leads to an increase in the percentage of v cells at the wound edge, hence resulting in the concave bridge observed in the lower left spindle across all plots (Fig 4.2G, 4.2H, and 4.2I). It's important to note that the effects of the PIEZO1 phenotype do not directly contribute to the formation of this "double spindle" pattern itself; rather, they result in the asymmetry of the double spindle, either by pulling it upward (e.g., Fig 4.2G) or pushing it downward (e.g., Fig 4.2H and 4.2I), thereby causing over-representation or under-representation in edge cell percentage. By mixing wild-type control cells with themselves, we can isolate the impact of the PIEZO1 phenotype and gain a better understanding of the double spindle pattern (Fig B.3C and B.3D). For a detailed analysis of this pattern formation, please refer to the appendix in Section B.1.3.

4.4.3 PIEZO1 activity promotes wound edge retraction

In the collective migration of wild-type keratinocytes, PIEZO1 channels display a heterogeneous spatial distribution (Fig 4.3A). Experimentally, *Piezo1*-cKO cells show complete suppression of PIEZO1 activity, while Yoda1-treated cells demonstrate full activation of PIEZO1 channels. Wild-type control cells, conversely, exhibit PIEZO1 activity levels intermediate between *Piezo1*-cKO and Yoda1-treated cells. Given this context, we assume that wild-type cells (e.g., $\text{Control}_{\text{cKO}}$ and DMSO-treated) function similarly to a mixture of *Piezo1*-cKO cells and Yoda1-treated cells (Fig 4.3B) in collective cell migration. We opt to use Yoda1-treated cells rather than *Piezo1*-GoF to mix with *Piezo1*-cKO due to the substantially higher PIEZO1 activity in Yoda1-treated cells compared to *Piezo1*-GoF, thereby allowing for a broader representation of wild-type control. From a model calibration standpoint, *Piezo1*-cKO and Yoda1-treated are both calibrated from the same control dataset, because $\text{Control}_{\text{cKO}}$ and DMSO-treated cells are experimentally indistinguishable (detailed in Section 4.3.3). Therefore, in this section, we simulate the model of mixing *Piezo1*-cKO and Yoda1-treated cells to study wound closure in wild-type keratinocytes.

In the preceding section, we examined the distribution of cells at the wound edge under different levels of PIEZO1 activity. However, considering that the localization of PIEZO1 channels governs wound edge retraction [35], we aim to delve deeper into the distribution of edge cells in the mixture, taking into account their migrating direction. To achieve this, we tracked the movement of edge cells in our model simulation by identifying the banded region of edge cells (shaded area in Fig 4.3C) and labeling the midpoints within this region (white asterisks in Fig 4.3C). Subsequently, throughout the simulated wound closure process, we were able to monitor the vertical movement direction (the direction to close the wound) of these labeled points (pink arrows in Fig 4.3C).

Through repeated simulations of wound closure involving mixtures of *Piezo1*-cKO and

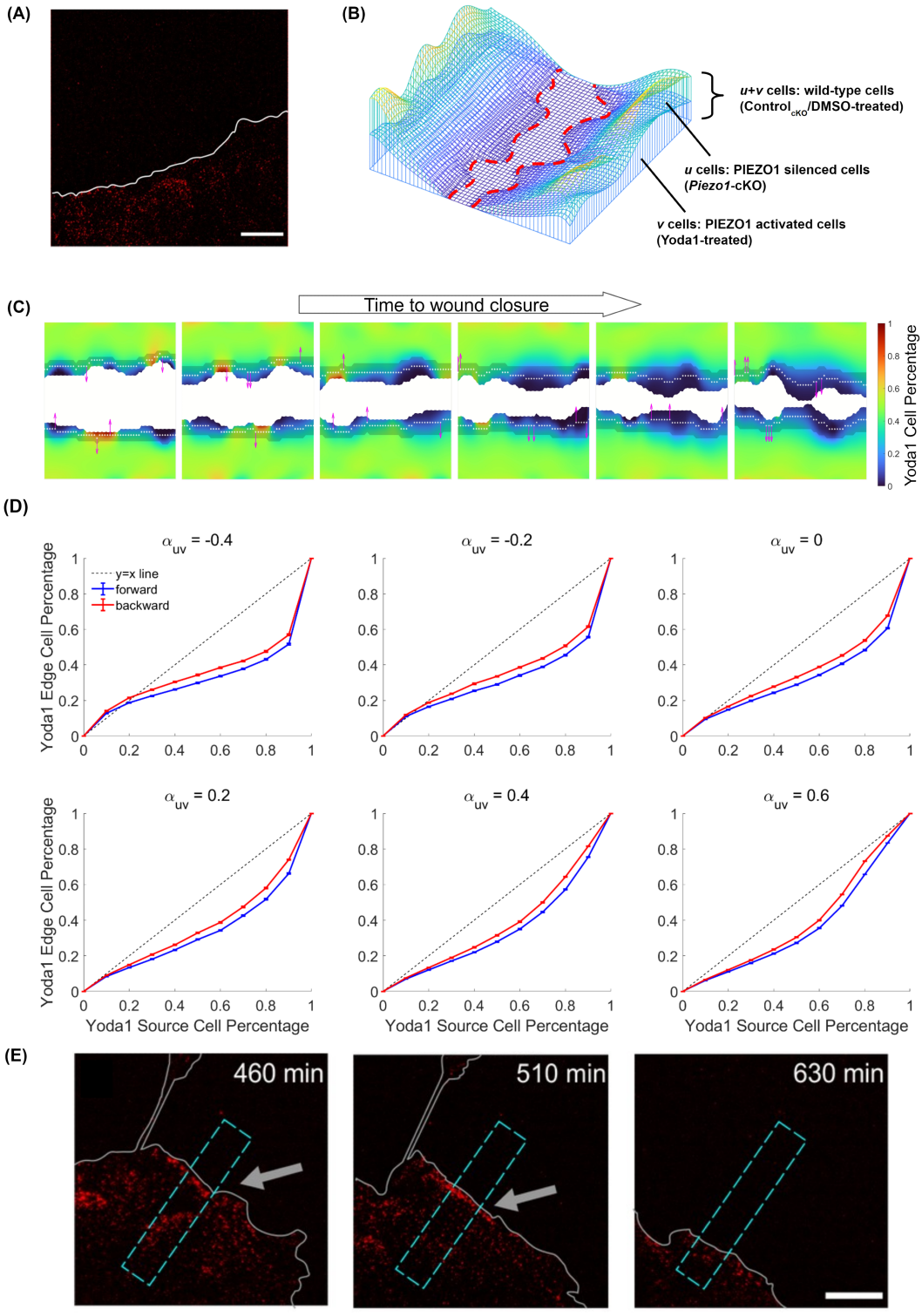

Figure 4.3: **Enrichment of PIEZO1-activated cells promotes wound edge retraction.**

Figure 4.3 continued on next page

Figure 4.3 continued
(A) Total internal reflection fluorescence (TIRF) image illustrating the location of PIEZO1-tdTomato protein immediately after wounding in a keratinocyte monolayer in an in vitro scratch assay. The white line denote the cell boundary. This experimental result was originally presented by Holt *et al.* [35] in Figure 4 - figure supplement 1. Scale bar = 20 μm. **(B)** Schematic showing a visualization of the simulation domain. The red dashed lines demonstrate the wound edges. **(C)** Snapshots depict the progression of wound healing for a mixture of *Piezo1*-cKO (u cells) and Yoda1-treated (v cells), captured at evenly spaced time intervals. Colored areas represent cell monolayers, with colors indicating the spatial distribution of Yoda1-treated (v cells) percentages, while plain white areas denote cell-free space. The shaded area near the wound edge indicates the region of edge cells, where the total cell density is less than 0.2. White asterisks within the shaded area mark midpoints in the wound closing direction (i.e., in the y direction). Magenta arrows originating from the asterisks illustrate the migrating direction of edge cells, either forward or backward. **(D)** The model involves mixing *Piezo*-cKO cells (u cells) and Yoda1-treated cells (v cells). Cells at the wound edge are categorized based on their migrating direction: forward or protrusion (*blue*), and backward or retraction (*red*). The figures depict the mean of 100 simulation results, displaying the percentage of v cells in forward and backward edge cells relative to its percentage in source cells, under various interaction coefficient (α_{uv}). Error bars indicate the standard error of the mean. **(E)** Representative TIRF images from time-lapse series of healing monolayers of PIEZO1-tdTomato keratinocytes, highlighting fields of view, demonstrate an enriched PIEZO1 channel at the monolayer's retracting edge, serving as a necessary condition for the enrichment of PIEZO1-activated cells at the wound edge. This experimental observation was originally presented by Holt *et al.* in [35], Figure 4C. Scale bar = 20 μm.

Yoda1-treated cells, and subsequent averaging, we determine the proportion of Yoda1-treated cells in both forward and backward edge cells relative to Yoda1 heterogeneity p_v under various interaction coefficient α_{uv} conditions (Fig 4.3D). The findings reveal a higher proportion of Yoda1-treated cells among backward edge cells compared to forward edge cells, indicating that Yoda1-treated cell enrichment correlates with backward events at the wound edge. This suggests that a larger fraction of PIEZO1-activated cells participate in wound edge retraction rather than protrusion, aligning with experimental observations where PIEZO1 channels are predominantly enriched in retraction (Fig 4.3E). Remarkably, our results not only support the previous experimental finding that the spatial distribution of PIEZO1 channels regulates wound edge retraction [35], but also predict that these enriched cells associated with wound edge retraction events exhibit higher PIEZO1 activity levels.

By relaxing the assumption that wild-type control functions similarly to a mixture of *Piezo1*-cKO cells and Yoda1-treated cells, we further investigated the impact of PIEZO1 activity on the migration direction of edge cells in general mixture scenarios. Numerical simulations were conducted for different mixtures following the same process as in Fig 4.3D. As anticipated, in mixtures with $\text{Control}_{\text{cKO}}$, *Piezo1*-cKO cells had a higher percentage in forward edge cells than in backward edge cells (Fig B.9). Conversely, Yoda1-treated cells exhibited a higher percentage in backward edge cells compared to forward edge cells, not only when mixed with *Piezo1*-cKO (Fig 4.3D) but also with DMSO-treated cells (Fig B.10D). These findings from model simulation validate our conclusion regarding the positive correlation between PIEZO1 activity and wound edge retraction. However, a noteworthy observation emerged in the mixture of $\text{Control}_{\text{GoF}}$ and *Piezo1*-GoF: under repulsive interactions between u and v cells (i.e., $\alpha_{uv} < 0$), the percentage of *Piezo1*-GoF cells in backward edge cells, which was expected to be lower than in forward edge cells due to the higher PIEZO1 activity of *Piezo1*-GoF compared to $\text{Control}_{\text{GoF}}$, was actually higher than in forward cells (Fig B.7). Further investigation revealed that this phenomenon primarily stemmed from the longer and stronger retraction observed in *Piezo1*-GoF cells compared to its mixture counterparts, $\text{Control}_{\text{GoF}}$ cells. Additional details are provided in the appendix in Section B.1.5.

4.4.4 Interaction coefficient can be inferred from the mixture heterogeneity

While we are interested in the interaction between different cell types, measuring the value of α_{uv} experimentally is challenging. However, the percentage of each cell type in the mixture (p_u and p_v) is relatively accessible from experimental data. Therefore, we aim to use our model to infer the parameter value of α_{uv} through the heterogeneity p_v. Although specific experimental data regarding PIEZO1 activity in keratinocytes is currently unavailable, relevant information from endothelial cells was recently provided by Bertaccini *et al.* using

novel PIEZO1-HaloTag hiPSCs technology [7] (Fig 4.4A). Based on their experiments, the level of PIEZO1 activity can be characterized by the puncta density in JF646-BAPTA HTL labeled PIEZO1-HaloTag cells (activity probe), normalized by the puncta density in JF646 HTL treated PIEZO1-HaloTag cells (location probe). Thus,

$$A_{\text{total}} = p_u A_u + p_v A_v, \tag{4.17}$$

where A_{total} represents the PIEZO1 activity level of the mixture cells, while A_u and A_v denote the activity levels for the u and v cells constituting the mixture, respectively. Following the same model assumption from the preceding section, where wild-type cells function similarly to a mixture of *Piezo1*-cKO cells and Yoda1-treated cells (Fig 4.3B) in collective cell migration, we define A_{total} as the PIEZO1 activity of wild-type control cells, while A_u and A_v represent the PIEZO1 activity of *Piezo1*-cKO cells and Yoda1-treated cells, respectively. Based on the data provided in Fig 4.4A, we can calculate $A_{\text{total}} = 0.212$, $A_u = 0.0564$, and $A_v = 0.652$. Together with the relation $p_u + p_v = 1$, these values can be substituted into Eq. 4.17 to derive that $p_v = 0.261$. Hence, the proportion of PIEZO1-activated cells in the wild type control is estimated to be around 26%.

Once we have $p_v = 0.261$, the cell-cell interaction between different types of cells in the mixture can be inferred using our mathematical model. Returning to the analysis of normalized wound closure (Fig 4.1F), we can more comprehensively visualize the normalized wound closure with respect to p_v and α_{uv} using a colormap (Fig 4.4B). The contour line indicating unit normalized wound closure (white dashed line in Fig 4.4B) represents the wild-type control. This critical line defines the relationship between p_v and α_{uv} in the wild-type control, meaning that the pairs (p_v, α_{uv}) for the wild-type control lie along this line. Therefore, with the value of $p_v = 0.261$, we can determine the corresponding α_{uv} on this line, which is

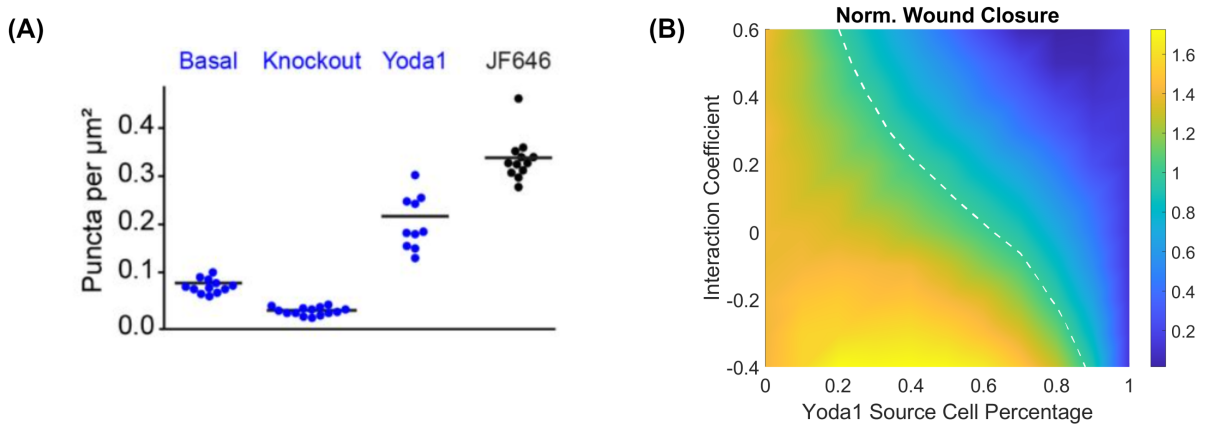

Figure 4.4: **Interaction coefficient can be inferred from the mixture heterogeneity.** **(A)** Reproduced from Figure 3B in [7]. JF646-BAPTA HTL puncta density. All values are expressed as mean ± standard error of the mean. In the unit of puncta per μm^2, Basal (mean = 0.07 ± 0.004), PIEZO1-HaloTag KO (mean = 0.02 ± 0.002), 2 μM Yoda 1 (mean = 0.22 ± 0.02), and JF646 HTL (mean = 0.34 ± 0.01). Data are from 4 independent experiments. All groups were significantly different from one another (p-value Mann-Whitney < 0.005 for all conditions). Cohen's d effect sizes of PIEZO1-HaloTag treated with 2 μM Yoda1 compared to PIEZO1-HaloTag (2.28) and of PIEZO1-HaloTag Knockout compared to PIEZO1-HaloTag (-4.46). **(B)** Colormap illustrating the normalized wound closure from model simulations, under various combinations of Yoda1-treated source cell percentage (p_v, x-axis) and interaction coefficient values (α_{uv}, y-axis). The white dashed line represents the contour of unit normalized wound closure, denoting the wound closure of wild-type control cells.

approximately 0.42. Consequently, the interaction between PIEZO1-activated cells (characterized by Yoda1-treated) and PIEZO1-inactivated cells (characterized by *Piezo1*-cKO) in the wild-type is predicted to have stronger adhering effects ($\alpha_{uv} \approx 0.42$) than the cell-cell adhesion between cells with the same PIEZO1 activity level ($\alpha_{uu} = \alpha_{vv} = 0.2$). Note that this qualitative result still holds true under different values of α_{uu} and α_{vv}, as elaborated in the appendix (Fig B.1H, B.1I, B.2H and B.2I).

4.5 Discussion

In this chapter, we develop a new model that considers the migration of two distinct cell types, each governed by its own set of equations with unique parameters, while interacting through cell-cell adhesion, volume-filling effects and wound edge retraction. Specifically, the cell densities are denoted as u and v. Regarding volume-filling effects, the migration of either u cells or v cells is impeded by the total density of cells $(u + v)$ in their path. The spatial position of wound edges is determined by the interface between the total cell population $(u+v)$ and the cell-free region. However, retractions near wound edges are applied individually to u cells and v cells, each following their respective retraction parameters, including the duration and strength of retraction, as well as the interval between retractions. Regarding model parameters in this study, our primary focus is on the interaction between these two cell types (α_{uv}) and the mixture heterogeneity characterized by the percentage of v source cells (p_v).

Through simulations involving three different mixtures ($\text{Control}_{\text{cKO}}$ & *Piezo1*-cKO, $\text{Control}_{\text{GoF}}$ & *Piezo1*-GoF, and $\text{Control}_{\text{cKO}}$ & Yoda1-treated), we observed that mutually repelling cells, modeled by negative cell-cell interaction ($\alpha_{uv} < 0$), can promote wound closure more effectively than individual PIEZO1 phenotypes. Furthermore, the impact of cell-cell interaction on wound healing—whether hindered by adhesion ($\alpha_{uv} > 0$) or promoted by repulsion

($\alpha_{uv} < 0$)—is amplified by the heterogeneity of the mixture. This implies that wounds in mutually repulsive mixtures can achieve faster closure when u and v cells are present in similar proportions. Investigating the cell distribution near the wound edge, we observed that higher PIEZO1 activity correlates with a lower edge cell percentage compared to the overall source cell percentage, indicating that PIEZO1 down-regulates edge cell representation. Additionally, when we relate wild-type cells to a mixture of *Piezo1*-cKO and Yoda1-treated cells, we find that Yoda1-treated cells have a higher percentage in backward edge cells compared to forward edge cells, suggesting that PIEZO1 activity promotes wound edge retraction. This result is consistent with, and even stronger than, prior experimental findings that wound edge retraction is related to PIEZO1 enrichment [35]. Finally, using endothelial experimental data to inform the PIEZO1 heterogeneity in wild-type cells, our model infers the value of the interaction coefficient α_{uv}, predicting that the interaction between cells with different PIEZO1 activity levels involves stronger adhesion than the cell-cell adhesion between cells with the same PIEZO1 activity.

Currently, experiments involving PIEZO1 location probes for keratinocyte migration are available [35], but PIEZO1 activity probes are not yet feasible. This delay in keratinocyte experiments hinders the validation of our model predictions regarding cell-cell interactions in Section 4.4.4. Additionally, by using single-cell data from endothelial experiments, we assumed that cell-cell interactions do not affect PIEZO1 activity. Under this assumption, the PIEZO1 activity data obtained from single cells (Fig 4.4A) remains applicable in the context of a monolayer.

Chapter 5

Discussion

Mechanical cues have been highlighted to play a prominent role in facilitating the coordinated polarization of individual cells within a collective, regulating the speed and coordinated directionality of collective migration [48]. We recently identified the mechanically activated ion channel PIEZO1 as being a key regulator of wound healing: keratinocytes with increased PIEZO1 activity exhibited delayed wound healing while decreased PIEZO1 activity resulted in faster wound healing [35]. Given PIEZO1's role in wound healing, we explored PIEZO1's effect on leader cell formation and coordinated directionality during collective keratinocyte migration. By taking a combined integrative mathematical modeling and experimental approach we identified that PIEZO1 activity suppresses leader cell formation, limits the coordinated directionality of cells during epithelial sheet migration, and reduces the distance by which keratinocytes can coordinate their directionality (Fig 5.1). This is the first time that PIEZO1 is seen to contribute to the correlation of cellular motions between neighboring cells which underlie the collective movements of cells during epithelial sheet migration. Given that PIEZO1 acts as a key mechanosensor in keratinocytes, this provides further evidence of the channel acting to couple mechanotransduction with correlated migration.

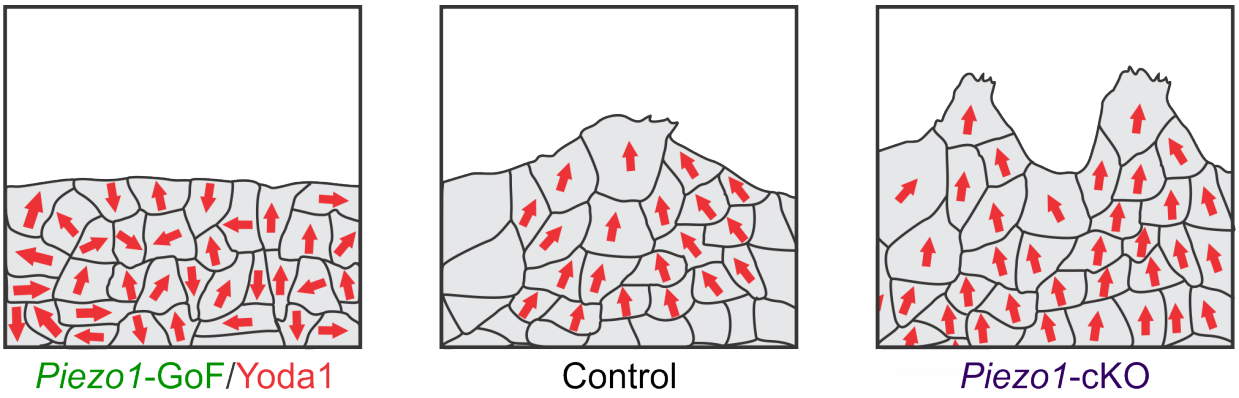

Figure 5.1: **PIEZO1 activity inhibits spatial coordination and leader cell formation during collective migration.** Summary schematic of collectively migrating monolayer of keratinocyte cells (gray) with direction of cellular motion overlaid (red arrows) under *Piezo1*-GoF/Yoda1 (*left*), Control (*middle*) and *Piezo1*-cKO (*right*) conditions. Note how as PIEZO1 activity is decreased, the coordinated direction of cells and number of leader cells increases.

In order to describe the inherent biological complexities underlying keratinocyte reepithelialization we adopted mathematical modeling as a tool to systematically investigate how aspects of collective cell migration affect wound closure. Through the development of a two-dimensional continuum model of wound closure derived through upscaling from a discrete model, we investigated how components of wound closure including cell motility, cell-cell adhesion, cell-edge retraction and the coordination of migration direction between cells, i.e., coordinated directionality, change with manipulation of PIEZO1 activity. Through numerical simulations, we incorporated experimental data to calibrate our model and match keratinocyte monolayer behavior. We examined how model parameters impacted two attributes of wound closure which we experimentally find are affected by PIEZO1 activity: the rate of wound closure and the edge length of simulated monolayers, which served as a measure of leader cell formation. From the modeling studies, the coordinated directionality of cells was identified as a key model parameter predicted to be impaired by PIEZO1 activity during wound closure.

Our model prediction guided the design of validation experiments and subsequent bioimage analyses, in which we confirmed the model prediction and demonstrated that PIEZO1

activity inhibits the ability of local subpopulations of cells to coordinate their movements across distances during collective migration. Altogether, we identified that PIEZO1 activity inversely correlates with the number of leader cells along the wound edge which in turn dictates the directed migration of cell collectives during keratinocyte reepithelialization. Taken together with the prior work demonstrating that enrichment of PIEZO1 at the wound edge triggers local retraction [35], we propose that PIEZO1-mediated retraction inhibits leader cell formation, which disrupts the uniform polarization of groups of cells and underlies the inhibition of collective migration during wound closure. This proposal is consistent with findings by other groups where pharmacologically increasing the contractile forces within monolayers was found to inhibit leader cell formation [18, 72, 87].

The explorations of collective cell migration during wound healing in scenarios where more than one PIEZO1 genotype is present add an intriguing dimension to our study. We extended our mathematical model using an upscaled framework to study heterogeneous PIEZO1 activity, where each cell type operates under its own set of equations and parameters, interacting through cell-cell adhesion, volume-filling effects, and wound edge retraction. Inheriting the parameters from the previous model for individual cell type, this new model also characterizes the interactions between different cell types and the heterogeneity within their mixtures. Simulations with various combinations of cell mixtures reveal that mutually repulsive cells facilitate more efficient wound closure compared to a homogeneous population of a single cell type. The effectiveness of wound closure regulated by cell-cell interaction is positively correlated with the heterogeneity of the cell mixture. Additionally, simulations indicate that cells with higher PIEZO1 activity in the mixture correspond to a reduced representation at wound edge. Under further model assumptions, these cells with higher PIEZO1 activity are predominantly located at the backward edge, rather than the forward edge, implying the possibility that PIEZO1 activity enhances wound edge retraction. This finding is consistent with previous experimental results linking wound edge retraction to PIEZO1 enrichment [35]. Utilizing this extended model, we also delve into parameter inference by integrating

relevant experimental data. This extended work suggests future experiments combining cells of different genotypes to investigate the effects of homotypic and heterotypic interactions on cell migration and wound healing.

Collective cell migration is an emergent phenomenon occuring at the multicellular level and stems from the large-scale coordination of individual cellular motions. Mechanical forces have been highlighted as playing an important role in shaping collective cell behaviors and influencing the formation and dynamics of both leader and follower cells [17, 48, 88]. Through this work, we have provided the first identification that the upregulation of PIEZO1 activity suppresses leader cell formation and inhibits both the coordinated directionality and the distance by which cells coordinate their cellular motion across length scales during epithelial sheet migration. Moreover, we develop a novel mathematical model for PIEZO1 regulated collective cell migration which is generalizable to studying the role of other proteins or cell types during epithelial sheet migration through analogous simulation and analyses. Specifically, while our model was developed to simulate collective cell migration, the influence of PIEZO1 was implemented by calibrating the model parameters with experimental data. Consequently, to study the effects of other proteins on different cell types in collective migration, we can experimentally measure cell edge retraction for the specific scenario and calibrate the model using this data, without requiring any structural changes to the model, either theoretically or numerically. In our work, we propose that elevated PIEZO1-induced cell retraction inhibits the normal long-range coordination between cells during collective migration, disrupting typical mechanochemical activity patterns and the coordinated polarization of neighboring cells. Our findings provide a new biophysical mechanism by which PIEZO1 activity regulates the spatiotemporal dynamics across multiple cells to shape collective migration.

Bibliography

[1] M. Amereh, R. Edwards, M. Akbari, and B. Nadler. In-silico modeling of tumor spheroid formation and growth. *Micromachines*, 12(7):749, June 2021.

[2] T. E. Angelini, E. Hannezo, X. Trepat, M. Marquez, J. J. Fredberg, and D. A. Weitz. Glass-like dynamics of collective cell migration. *Proc. Natl. Acad. Sci. U. S. A.*, 108(12):4714–4719, Mar. 2011.

[3] K. Anguige and C. Schmeiser. A one-dimensional model of cell diffusion and aggregation, incorporating volume filling and cell-to-cell adhesion. *J. Math. Biol.*, 58(3):395–427, June 2008.

[4] S. Bajpai, R. Prabhakar, R. Chelakkot, and M. M. Inamdar. Role of cell polarity dynamics and motility in pattern formation due to contact-dependent signalling. *J. R. Soc. Interface*, 18(175):20200825, Feb. 2021.

[5] S. Banerjee and M. Cristina. Continuum models of collective cell migration. *Cell Migrations: Causes and Functions*, pages 45–66, 2019.

[6] D. J. Barry, C. H. Durkin, J. V. Abella, and M. Way. Open source software for quantification of cell migration, protrusions, and fluorescence intensities. *J. Cell Biol.*, 209(1):163–180, Apr. 2015.

[7] G. A. Bertaccini, E. L. Evans, J. L. Nourse, G. D. Dickinson, G. Liu, I. Casanellas, S. Seal, A. T. Ly, J. R. Holt, S. Yan, E. E. Hui, M. M. Panicker, S. Upadhyayula, I. Parker, and M. M. Pathak. Piezo1-halotag hipscs: Bridging molecular, cellular and tissue imaging. *bioRxiv*, 2023.

[8] A. Bianco, M. Poukkula, A. Cliffe, J. Mathieu, C. M. Luque, T. A. Fulga, and P. Rørth. Two distinct modes of guidance signalling during collective migration of border cells. *Nature*, 448(7151):362–365, July 2007.

[9] D. Boocock, N. Hino, N. Ruzickova, T. Hirashima, and E. Hannezo. Theory of mechanochemical patterning and optimal migration in cell monolayers. *Nat. Phys.*, 17(2):267–274, Sept. 2020.

[10] A. Buttenschön and L. Edelstein-Keshet. Bridging from single to collective cell migration: A review of models and links to experiments. *PLoS Comput. Biol.*, 16(12):e1008411, Dec. 2020.

[11] D. Cai, S.-C. Chen, M. Prasad, L. He, X. Wang, V. Choesmel-Cadamuro, J. K. Sawyer, G. Danuser, and D. J. Montell. Mechanical feedback through e-cadherin promotes direction sensing during collective cell migration. *Cell*, 157(5):1146–1159, May 2014.

[12] V. Calandrini, E. Pellegrini, P. Calligari, K. Hinsen, and G. R. Kneller. nmoldyn - interfacing spectroscopic experiments, molecular dynamics simulations and models for time correlation functions. *Éc. thémat. Soc. Fr. Neutron.*, 12:201–232, 2011.

[13] B. Canales Coutiño and R. Mayor. The mechanosensitive channel piezo1 cooperates with semaphorins to control neural crest migration. *Development*, 148(23), Dec. 2021.

[14] L. Capuana, A. Boström, and S. Etienne-Manneville. Multicellular scale front-to-rear polarity in collective migration. *Curr. Opin. Cell Biol.*, 62:114–122, Feb. 2020.

[15] V. I. Chubinskiy-Nadezhdin, V. Y. Vasileva, I. O. Vassilieva, A. V. Sudarikova, E. A. Morachevskaya, and Y. A. Negulyaev. Agonist-induced piezo1 activation suppresses migration of transformed fibroblasts. *Biochem. Biophys. Res. Commun.*, 514(1):173–179, June 2019.

[16] E. Chuntharpursat-Bon, O. Povstyan, M. Ludlow, D. Carrier, M. Debant, J. Shi, H. Gaunt, C. Bauer, A. Curd, T. Simon Futers, P. Baxter, M. Peckham, S. Muench, A. Adamson, N. Humphreys, S. Tumova, R. Bon, R. Cubbon, L. Lichtenstein, and D. Beech. Piezo1 and pecam1 interact at cell-cell junctions and partner in endothelial force sensing. *Commun Biol*, 6(1):358, Apr. 2023.

[17] T. Das, K. Safferling, S. Rausch, N. Grabe, H. Boehm, and J. P. Spatz. A molecular mechanotransduction pathway regulates collective migration of epithelial cells. *Nat. Cell Biol.*, 17(3):276–287, Mar. 2015.

[18] Z. S. Dean, N. Jamilpour, M. J. Slepian, and P. K. Wong. Decreasing wound edge stress enhances leader cell formation during collective smooth muscle cell migration. *ACS Biomater Sci Eng*, 5(8):3864–3875, Aug. 2019.

[19] M. Deforet, V. Hakim, H. G. Yevick, G. Duclos, and P. Silberzan. Emergence of collective modes and tri-dimensional structures from epithelial confinement. *Nat. Commun.*, 5:3747, May 2014.

[20] K. Doxzen, S. R. K. Vedula, M. C. Leong, H. Hirata, N. S. Gov, A. J. Kabla, B. Ladoux, and C. T. Lim. Guidance of collective cell migration by substrate geometry. *Integr. Biol.*, 5(8):1026–1035, Aug. 2013.

[21] A. Edelstein, N. Amodaj, K. Hoover, R. Vale, and N. Stuurman. Computer control of microscopes using μmanager. *Curr. Protoc. Mol. Biol.*, Chapter 14:Unit14.20, Oct. 2010.

[22] A. D. Edelstein, M. A. Tsuchida, N. Amodaj, H. Pinkard, R. D. Vale, and N. Stuurman. Advanced methods of microscope control using μManager software. *J Biol Methods*, 1(2), 2014.

[23] D. Ershov, M.-S. Phan, J. W. Pylvänäinen, S. U. Rigaud, L. Le Blanc, A. Charles-Orszag, J. R. W. Conway, R. F. Laine, N. H. Roy, D. Bonazzi, G. Duménil, G. Jacquemet, and J.-Y. Tinevez. TrackMate 7: integrating state-of-the-art segmentation algorithms into tracking pipelines. *Nat. Methods*, pages 1–4, June 2022.

[24] E. Fazeli, N. H. Roy, G. Follain, R. F. Laine, L. von Chamier, P. E. Hänninen, J. E. Eriksson, J.-Y. Tinevez, and G. Jacquemet. Automated cell tracking using StarDist and TrackMate. *F1000Res.*, 9:1279, Oct. 2020.

[25] C. M. Franz, G. E. Jones, and A. J. Ridley. Cell migration in development and disease. *Dev. Cell*, 2(2):153–158, Feb. 2002.

[26] P. Friedl and D. Gilmour. Collective cell migration in morphogenesis, regeneration and cancer. *Nat. Rev. Mol. Cell Biol.*, 10(7):445–457, July 2009.

[27] I. González-Valverde and J. M. García-Aznar. Mechanical modeling of collective cell migration: An agent-based and continuum material approach. *Comput. Methods Appl. Mech. Eng.*, 337:246–262, Aug. 2018.

[28] R. Gorelik and A. Gautreau. Quantitative and unbiased analysis of directional persistence in cell migration. *Nat. Protoc.*, 9(8):1931–1943, Aug. 2014.

[29] A. Haeger, K. Wolf, M. M. Zegers, and P. Friedl. Collective cell migration: guidance principles and hierarchies. *Trends Cell Biol.*, 25(9):556–566, Sept. 2015.

[30] V. Hakim and P. Silberzan. Collective cell migration: a physics perspective. *Rep. Prog. Phys.*, 80(7):076601, July 2017.

[31] N. Hino, L. Rossetti, A. Marín-Llauradó, K. Aoki, X. Trepat, M. Matsuda, and T. Hirashima. ERK-Mediated mechanochemical waves direct collective cell polarization. *Dev. Cell*, 53(6):646–660.e8, June 2020.

[32] J. Ho, T. Tumkaya, S. Aryal, H. Choi, and A. Claridge-Chang. Moving beyond P values: data analysis with estimation graphics. *Nat. Methods*, 16(7):565–566, July 2019.

[33] W. R. Holmes, J. Park, A. Levchenko, and L. Edelstein-Keshet. A mathematical model coupling polarity signaling to cell adhesion explains diverse cell migration patterns. *PLoS Comput. Biol.*, 13(5):e1005524, May 2017.

[34] W. R. Holmes, J. Park, A. Levchenko, and L. Edelstein-Keshet. A mathematical model coupling polarity signaling to cell adhesion explains diverse cell migration patterns. *PLoS Comput. Biol.*, 13(5):e1005524, May 2017.

[35] J. R. Holt, W.-Z. Zeng, E. L. Evans, S.-H. Woo, S. Ma, H. Abuwarda, M. Loud, A. Patapoutian, and M. M. Pathak. Spatiotemporal dynamics of PIEZO1 localization controls keratinocyte migration during wound healing. *Elife*, 10, Sept. 2021.

[36] Z. Huang, Z. Sun, X. Zhang, K. Niu, Y. Wang, J. Zheng, H. Li, and Y. Liu. Loss of stretch-activated channels, PIEZOs, accelerates non-small cell lung cancer progression and cell migration. *Biosci. Rep.*, 39(3), Mar. 2019.

[37] C. J, H. JR, E. EL, L. JS, and P. MM. Piezo1 regulates leader cell formation and cellular coordination during collective keratinocyte migration. *PLoS Comput Biol*, 20(4), 2024.

[38] G.-S. Jiang and C.-W. Shu. Efficient implementation of weighted ENO schemes. *J. Comput. Phys.*, 126(1):202–228, June 1996.

[39] V. O. Juma, L. Dehmelt, S. Portet, and A. Madzvamuse. A mathematical analysis of an activator-inhibitor rho GTPase model. *J. comput. dyn.*, 9(2):133, 2022.

[40] E. Khain, M. Katakowski, S. Hopkins, A. Szalad, X. Zheng, F. Jiang, and M. Chopp. Collective behavior of brain tumor cells: The role of hypoxia. *Phys. Rev. E*, 83(3):031920, Mar. 2011.

[41] H. Khataee, A. Czirok, and Z. Neufeld. Multiscale modelling of motility wave propagation in cell migration. *Sci. Rep.*, 10(1):8128, May 2020.

[42] C. S. Kim, X. Yang, S. Jacobsen, K. S. Masters, and P. K. Kreeger. Leader cell PLCγ1 activation during keratinocyte collective migration is induced by EGFR localization and clustering. *Bioeng Transl Med*, 4(3):e10138, Sept. 2019.

[43] H.-S. Kim, J.-S. Suh, Y.-K. Jang, S.-H. Ahn, G.-H. Choi, J.-Y. Yang, G.-H. Lim, Y. Jung, J. Jiang, J. Sun, M. Suk, Y. Wang, and T.-J. Kim. Förster resonance energy Transfer-Based Single-Cell imaging reveals Piezo1-Induced ca2+ flux mediates membrane ruffling and cell survival. *Front Cell Dev Biol*, 10:865056, May 2022.

[44] G. Kirfel and V. Herzog. Migration of epidermal keratinocytes: mechanisms, regulation, and biological significance. *Protoplasma*, 223(2-4):67–78, June 2004.

[45] J. M. Ko and D. Lobo. Continuous dynamic modeling of regulated cell adhesion: Sorting, intercalation, and involution. *Biophys. J.*, 117(11):2166–2179, Dec. 2019.

[46] A. Krull, T.-O. Buchholz, and F. Jug. Noise2Void - learning denoising from single noisy images. *arXiv:1811.10980 [cs]*, Nov. 2018.

[47] J. J. Lacroix, W. M. Botello-Smith, and Y. Luo. Probing the gating mechanism of the mechanosensitive channel piezo1 with the small molecule yoda1. *Nat. Commun.*, 9(1), 2018.

[48] B. Ladoux and R.-M. Mège. Mechanobiology of collective cell behaviours. *Nat. Rev. Mol. Cell Biol.*, 18(12):743–757, Dec. 2017.

[49] R. M. Lee, C. H. Stuelten, C. A. Parent, and W. Losert. Collective cell migration over long time scales reveals distinct phenotypes. *Converg Sci Phys Oncol*, 2(2), June 2016.

[50] R. M. Lee, M. I. Vitolo, W. Losert, and S. S. Martin. Distinct roles of tumor associated mutations in collective cell migration. *Sci. Rep.*, 11(1):10291, May 2021.

[51] C. Li, S. Rezania, S. Kammerer, A. Sokolowski, T. Devaney, A. Gorischek, S. Jahn, H. Hackl, K. Groschner, C. Windpassinger, E. Malle, T. Bauernhofer, and W. Schreibmayer. Piezo1 forms mechanosensitive ion channels in the human MCF-7 breast cancer cell line. *Sci. Rep.*, 5:8364, Feb. 2015.

[52] D. Li and Y.-L. Wang. Coordination of cell migration mediated by site-dependent cell-cell contact. *Proc. Natl. Acad. Sci. U. S. A.*, 115(42):10678–10683, Oct. 2018.

[53] J. Li, B. Hou, S. Tumova, K. Muraki, A. Bruns, M. J. Ludlow, A. Sedo, A. J. Hyman, L. McKeown, R. S. Young, N. Y. Yuldasheva, Y. Majeed, L. A. Wilson, B. Rode, M. A. Bailey, H. R. Kim, Z. Fu, D. A. Carter, J. Bilton, H. Imrie, P. Ajuh, T. N. Dear, R. M. Cubbon, M. T. Kearney, R. K. Prasad, P. C. Evans, J. F. Ainscough, and D. J. Beech. Piezo1 integration of vascular architecture with physiological force. *Nature*, 515(7526):279–282, Nov. 2014.

[54] L. Li, R. Hartley, B. Reiss, Y. Sun, J. Pu, D. Wu, F. Lin, T. Hoang, S. Yamada, J. Jiang, and M. Zhao. E-cadherin plays an essential role in collective directional migration of large epithelial sheets. *Cell. Mol. Life Sci.*, 69(16):2779–2789, Aug. 2012.

[55] C.-C. Liang, A. Y. Park, and J.-L. Guan. In vitro scratch assay: a convenient and inexpensive method for analysis of cell migration in vitro. *Nat. Protoc.*, 2(2):329–333, 2007.

[56] A. Liberzon, D. Lasagna, M. Aubert, P. Bachant, T. Käufer, jakirkham, A. Bauer, B. Vodenicharski, C. Dallas, J. Borg, tomerast, and ranleu. OpenPIV/openpiv-python: OpenPIV - python (v0.22.2) with a new extended search PIV grid option, July 2020.

[57] X.-D. Liu, S. Osher, and T. Chan. Weighted essentially non-oscillatory schemes. *J. Comput. Phys.*, 115(1):200–212, Nov. 1994.

[58] G. Lukinavičius, C. Blaukopf, E. Pershagen, A. Schena, L. Reymond, E. Derivery, M. Gonzalez-Gaitan, E. D'Este, S. W. Hell, D. Wolfram Gerlich, and K. Johnsson. SiR-Hoechst is a far-red DNA stain for live-cell nanoscopy. *Nat. Commun.*, 6:8497, Oct. 2015.

[59] S. Ma, A. E. Dubin, Y. Zhang, S. A. R. Mousavi, Y. Wang, A. M. Coombs, M. Loud, I. Andolfo, and A. Patapoutian. A role of PIEZO1 in iron metabolism in mice and humans. *Cell*, 184(4):969–982.e13, Feb. 2021.

[60] M. M. Maneshi, L. Ziegler, F. Sachs, S. Z. Hua, and P. A. Gottlieb. Enantiomeric Aβ peptides inhibit the fluid shear stress response of PIEZO1. *Sci. Rep.*, 8(1):14267, Sept. 2018.

[61] C. L. Marchant, A. N. Malmi-Kakkada, J. A. Espina, and E. H. Barriga. Cell clusters softening triggers collective cell migration in vivo. *Nat. Mater.*, Aug. 2022.

[62] R. Mayor and S. Etienne-Manneville. The front and rear of collective cell migration. *Nat. Rev. Mol. Cell Biol.*, 17(2):97–109, Feb. 2016.

[63] B. J. McHugh, A. Murdoch, C. Haslett, and T. Sethi. Loss of the Integrin-Activating transmembrane protein Fam38A (piezo1) promotes a switch to a reduced Integrin-Dependent mode of cell migration. *PLoS One*, 7(7):e40346, July 2012.

[64] Y. A. Miroshnikova, S. Manet, X. Li, S. A. Wickström, E. Faurobert, and C. Albiges-Rizo. Calcium signaling mediates a biphasic mechanoadaptive response of endothelial cells to cyclic mechanical stretch. *Mol. Biol. Cell*, 32(18):1724–1736, Aug. 2021.

[65] D. Oelz, H. Khataee, A. Czirok, and Z. Neufeld. Polarization wave at the onset of collective cell migration. *Phys Rev E*, 100(3-1):032403, Sept. 2019.

[66] T. Omelchenko, J. M. Vasiliev, I. M. Gelfand, H. H. Feder, and E. M. Bonder. Rho-dependent formation of epithelial "leader" cells during wound healing. *Proc. Natl. Acad. Sci. U. S. A.*, 100(19):10788–10793, Sept. 2003.

[67] M. M. Pathak, J. L. Nourse, T. Tran, J. Hwe, J. Arulmoli, D. T. T. Le, E. Bernardis, L. A. Flanagan, and F. Tombola. Stretch-activated ion channel piezo1 directs lineage choice in human neural stem cells. *Proc. Natl. Acad. Sci. U. S. A.*, 111(45):16148–16153, Nov. 2014.

[68] L. Petitjean, M. Reffay, E. Grasland-Mongrain, M. Poujade, B. Ladoux, A. Buguin, and P. Silberzan. Velocity fields in a collectively migrating epithelium. *Biophys. J.*, 98(9):1790–1800, May 2010.

[69] M. Poujade, E. Grasland-Mongrain, A. Hertzog, J. Jouanneau, P. Chavrier, B. Ladoux, A. Buguin, and P. Silberzan. Collective migration of an epithelial monolayer in response to a model wound. *Proc. Natl. Acad. Sci. U. S. A.*, 104(41):15988–15993, Oct. 2007.

[70] S. S. Ranade, Z. Qiu, S.-H. Woo, S. S. Hur, S. E. Murthy, S. M. Cahalan, J. Xu, J. Mathur, M. Bandell, B. Coste, Y.-S. J. Li, S. Chien, and A. Patapoutian. Piezo1, a mechanically activated ion channel, is required for vascular development in mice. *Proc. Natl. Acad. Sci. U. S. A.*, 111(28):10347–10352, July 2014.

[71] M. Reffay, M. C. Parrini, O. Cochet-Escartin, B. Ladoux, A. Buguin, S. Coscoy, F. Amblard, J. Camonis, and P. Silberzan. Interplay of RhoA and mechanical forces in collective cell migration driven by leader cells. *Nat. Cell Biol.*, 16(3):217–223, Mar. 2014.

[72] R. Riahi, J. Sun, S. Wang, M. Long, D. D. Zhang, and P. K. Wong. Notch1-Dll4 signalling and mechanical force regulate leader cell formation during collective cell migration. *Nat. Commun.*, 6:6556, Mar. 2015.

[73] A. J. Ridley, M. A. Schwartz, K. Burridge, R. A. Firtel, M. H. Ginsberg, G. Borisy, J. T. Parsons, and A. R. Horwitz. Cell migration: integrating signals from front to back. *Science*, 302(5651):1704–1709, Dec. 2003.

[74] O. Ronneberger, P. Fischer, and T. Brox. U-Net: Convolutional networks for biomedical image segmentation. In *Medical Image Computing and Computer-Assisted Intervention – MICCAI 2015*, pages 234–241. Springer International Publishing, 2015.

[75] J. Schindelin, I. Arganda-Carreras, E. Frise, V. Kaynig, M. Longair, T. Pietzsch, S. Preibisch, C. Rueden, S. Saalfeld, B. Schmid, J.-Y. Tinevez, D. J. White, V. Hartenstein, K. Eliceiri, P. Tomancak, and A. Cardona. Fiji: an open-source platform for biological-image analysis. *Nat. Methods*, 9(7):676–682, June 2012.

[76] S. Seetharaman and S. Etienne-Manneville. Cytoskeletal crosstalk in cell migration. *Trends Cell Biol.*, 30(9):720–735, Sept. 2020.

[77] S. SenGupta, C. A. Parent, and J. E. Bear. The principles of directed cell migration. *Nat. Rev. Mol. Cell Biol.*, 22(8):529–547, Aug. 2021.

[78] X. Serra-Picamal, V. Conte, R. Vincent, E. Anon, D. T. Tambe, E. Bazellieres, J. P. Butler, J. J. Fredberg, and X. Trepat. Mechanical waves during tissue expansion. *Nat. Phys.*, 8(8):628–634, July 2012.

[79] R. Syeda, J. Xu, A. E. Dubin, B. Coste, J. Mathur, T. Huynh, J. Matzen, J. Lao, D. C. Tully, I. H. Engels, H. M. Petrassi, A. M. Schumacher, M. Montal, M. Bandell, and A. Patapoutian. Chemical activation of the mechanotransduction channel piezo1. *eLife Sciences*, 4:e07369, May 2015.

[80] D. T. Tambe, C. C. Hardin, T. E. Angelini, K. Rajendran, C. Y. Park, X. Serra-Picamal, E. H. Zhou, M. H. Zaman, J. P. Butler, D. A. Weitz, J. J. Fredberg, and X. Trepat. Collective cell guidance by cooperative intercellular forces. *Nat. Mater.*, 10(6):469–475, June 2011.

[81] R. N. Thompson, C. A. Yates, and R. E. Baker. Modelling cell migration and adhesion during development. *Bull. Math. Biol.*, 74(12):2793–2809, Oct. 2012.

[82] J.-Y. Tinevez, N. Perry, J. Schindelin, G. M. Hoopes, G. D. Reynolds, E. Laplantine, S. Y. Bednarek, S. L. Shorte, and K. W. Eliceiri. TrackMate: An open and extensible platform for single-particle tracking. *Methods*, 115:80–90, Feb. 2017.

[83] X. Trepat, M. R. Wasserman, T. E. Angelini, E. Millet, D. A. Weitz, J. P. Butler, and J. J. Fredberg. Physical forces during collective cell migration. *Nat. Phys.*, 5(6):426–430, June 2009.

[84] S. R. K. Vedula, M. C. Leong, T. L. Lai, P. Hersen, A. J. Kabla, C. T. Lim, and B. Ladoux. Emerging modes of collective cell migration induced by geometrical constraints. *Proc. Natl. Acad. Sci. U. S. A.*, 109(32):12974–12979, Aug. 2012.

[85] J.-H. Venhuizen and M. M. Zegers. Making heads or tails of it: Cell-Cell adhesion in cellular and supracellular polarity in collective migration. *Cold Spring Harb. Perspect. Biol.*, 9(11), Nov. 2017.

[86] M. Vicente-Manzanares and A. R. Horwitz. Cell migration: an overview. *Methods Mol. Biol.*, 769:1–24, 2011.

[87] M. Vishwakarma, J. Di Russo, D. Probst, U. S. Schwarz, T. Das, and J. P. Spatz. Mechanical interactions among followers determine the emergence of leaders in migrating epithelial cell collectives. *Nat. Commun.*, 9(1):3469, Aug. 2018.

[88] M. Vishwakarma, J. P. Spatz, and T. Das. Mechanobiology of leader-follower dynamics in epithelial cell migration. *Curr. Opin. Cell Biol.*, 66:97–103, Oct. 2020.

[89] J. Wang, J. Jiang, X. Yang, G. Zhou, L. Wang, and B. Xiao. Tethering piezo channels to the actin cytoskeleton for mechanogating via the cadherin-β-catenin mechanotransduction complex. *Cell Rep.*, 38(6):110342, Feb. 2022.

[90] C. J. Weijer. Collective cell migration in development. *J. Cell Sci.*, 122(Pt 18):3215–3223, Sept. 2009.

[91] T. Witelski. Problems in nonlinear diffusion. *Dissertation (Ph.D.), California Institute of Technology*, 1995.

[92] M. L. Wynn, P. Rupp, P. A. Trainor, S. Schnell, and P. M. Kulesa. Follow-the-leader cell migration requires biased cell-cell contact and local microenvironmental signals. *Phys. Biol.*, 10(3):035003, June 2013.

[93] Y. Yang and H. Levine. Leader-cell-driven epithelial sheet fingering. *Phys. Biol.*, 17(4):046003, July 2020.

[94] M. Yao, A. Tijore, D. Cheng, J. V. Li, A. Hariharan, B. Martinac, G. Tran Van Nhieu, C. D. Cox, and M. Sheetz. Force- and cell state-dependent recruitment of piezo1 drives focal adhesion dynamics and calcium entry. *Sci Adv*, 8(45):eabo1461, Nov. 2022.

[95] Y. Yu, X. Wu, S. Liu, H. Zhao, B. Li, H. Zhao, and X. Feng. Piezo1 regulates migration and invasion of breast cancer cells via modulating cell mechanobiological properties. *Acta Biochim. Biophys. Sin.*, 53(1):10–18, Jan. 2021.

[96] L. Zechini, C. Amato, A. Scopelliti, and W. Wood. Piezo acts as a molecular brake on wound closure to ensure effective inflammation and maintenance of epithelial integrity. *Curr. Biol.*, July 2022.

[97] M. M. Zegers and P. Friedl. Rho GTPases in collective cell migration. *Small GTPases*, 5:e28997, May 2014.

[98] J. Zhang, Y. Zhou, T. Huang, F. Wu, L. Liu, J. S. H. Kwan, A. S. L. Cheng, J. Yu, K. F. To, and W. Kang. PIEZO1 functions as a potential oncogene by promoting cell proliferation and migration in gastric carcinogenesis. *Mol. Carcinog.*, 57(9):1144–1155, 2018.

Appendix A

Supplementary materials for the homogeneous model

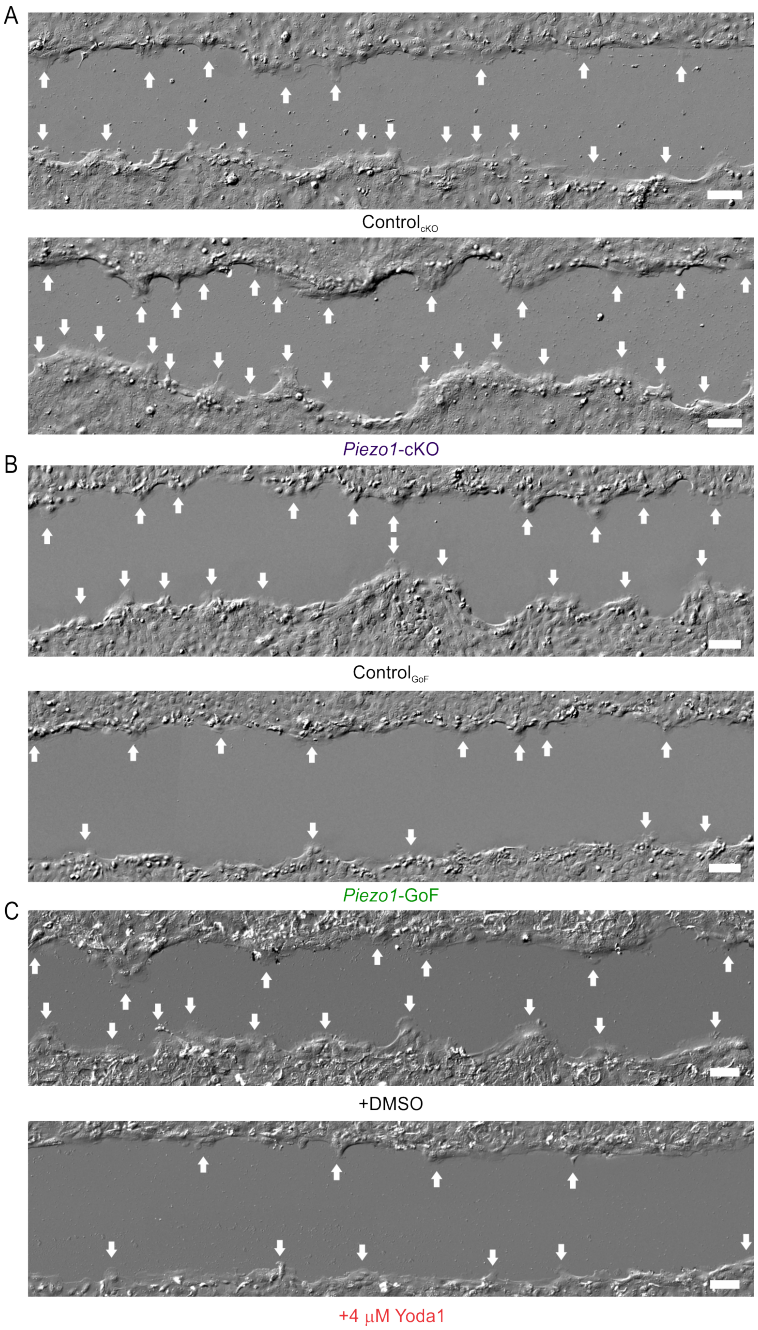

Figure A.1: **PIEZO1 inhibits leader cell formation at wound margins.** Representative DIC images of wounds generated in (**A***; top*) Control$_{\mathrm{cKO}}$, (**A***; bottom*) *Piezo1*-cKO, (**B***; top*) Control$_{\mathrm{GoF}}$, (**B***; bottom*) *Piezo1*-GoF, (**C***; top*) DMSO-treated and (**C***; bottom*) 4 μM Yoda1-treated monolayers. White arrows indicate leader cell protrusions. Representative images were taken at the same time point as the respective control field of view. Scale bar = 100 μm. Related to Fig 1.1.

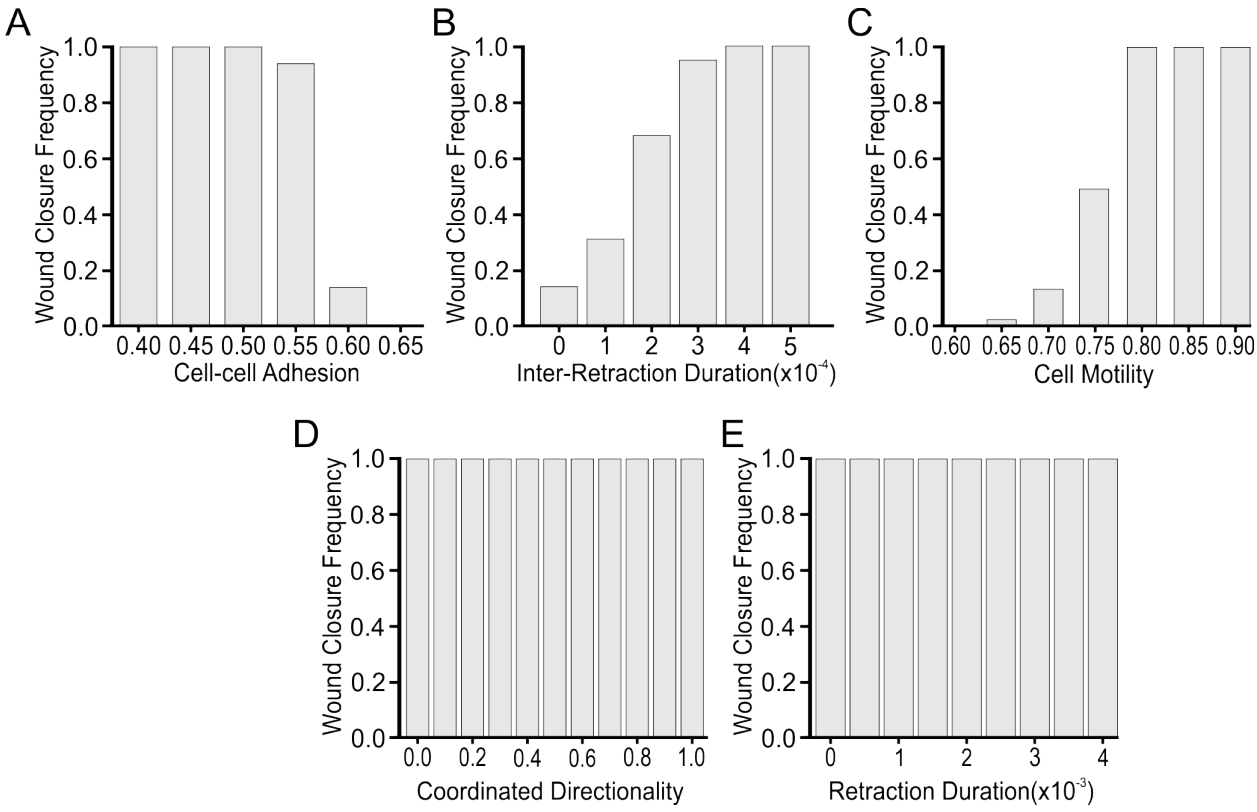

Figure A.2: **Wounds fail to reach closure if parameter values exceed reasonable ranges. (A)** The percentage of wound closure cases under different levels of cell-cell adhesion. **(B, C, D, E)** Similar to (A) but for inter-retraction duration, cell motility, coordinated directionality and retraction duration respectively. Related to Fig 2.1F.

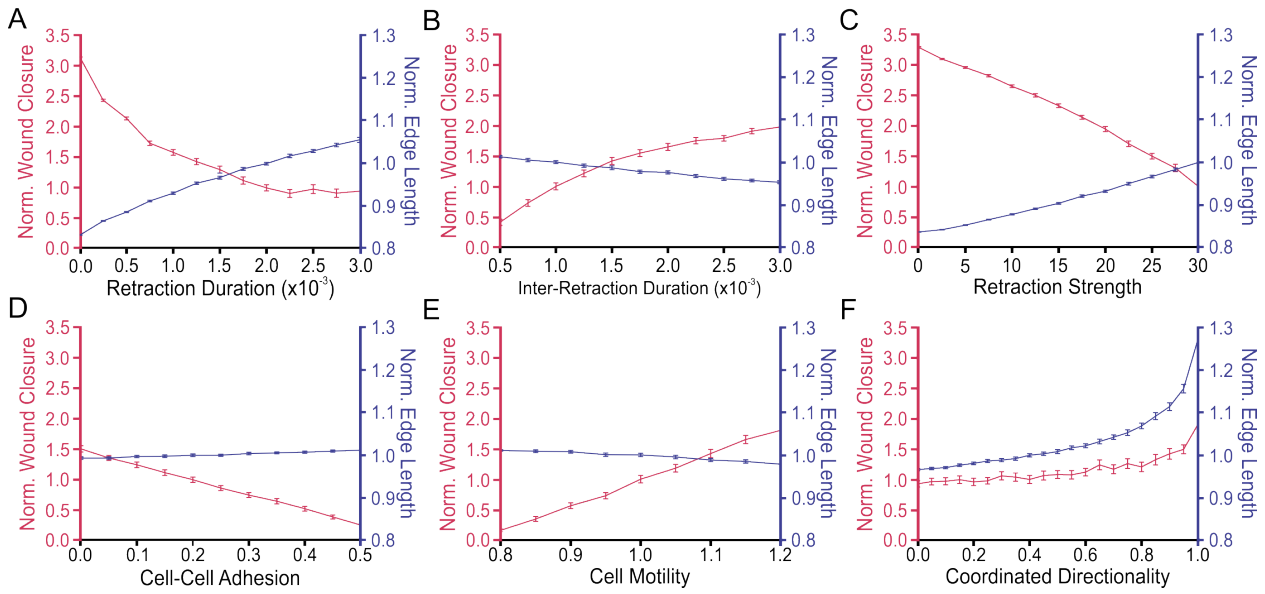

Figure A.3: **Coordinated directionality is the only parameter which replicates all experimental results.** **(A)** The mean of 100 simulation results showing the effect of retraction duration on normalized wound closure (*red; left axes*) and edge length (*blue; right axes*). Error bars depict the standard error of mean. **(B-F)** Similar to (A) but for inter-retraction duration, retraction strength, cell-cell adhesion, cell motility and coordinated directionality, respectively. The data in C and F are also shown in Fig 2.1G and Fig 2.1H but are reproduced here for ease of comparison.

parameter	notation	base value
retraction strength	μ_s	30
retraction duration	μ_r	2×10^{-3}
inter-retraction duration	μ_{nr}	1×10^{-3}
cell motility	d	1
cell-cell adhesion	α	0.2
coordinated directionality	w_A	0.4
grid size	h	0.01
retraction width	ω_r	0.2
boundary mean	μ_0	0.6
boundary standard deviation	σ_0	0.3
Heaviside smoothing steepness	k	10
spatial smoothing width	k_1^s	0.3
spatial smoothing steepness	k_2^s	3
temporal smoothing width	k_1^t	0.5
temporal smoothing steepness	k_2^t	10

Figure A.4: **List of model parameters and their base values.**

	retraction duration (min)	inter-retraction duration (min)	retraction strength ($\mu m/min$)
	mean, sem	mean, sem	mean, sem
$\text{Control}_{\text{cKO}}$/ DMSO-treated	4.63, 2.16	2.19, 0.81	1.85, 0.47
Piezo1-cKO	6.00, 1.77	6.45, 2.74	0.88, 0.14
Yoda1-treated	0.76, 0.07	0.90, 0.08	5.31, 0.93
$\text{Control}_{\text{GoF}}$	0.91, 0.11	1.86, 0.50	0.99, 0.10
Piezo1-GoF	1.07, 0.17	0.94, 0.14	1.62, 0.19

	cell motility ($\mu m/min$)
	mean, sem
$\text{Control}_{\text{cKO}}$	0.56, 0.04
Piezo1-cKO	0.78, 0.08
DMSO-treated	0.46, 0.03
Yoda1-treated	0.48, 0.03
$\text{Control}_{\text{GoF}}$	1.28, 0.08
Piezo1-GoF	1.09, 0.06

Figure A.5: **PIEZO1 activity affects single cell migration.** Mean and standard error of mean (sem) of single cell migration dataset (retraction duration, inter-retraction duration, retraction strength and cell motility) under different experimental conditions. Retraction duration data was derived by kymograph measurements, retraction strength derived from cell shape analysis and cell motility data from tracking cells during single cell migration assays [35].

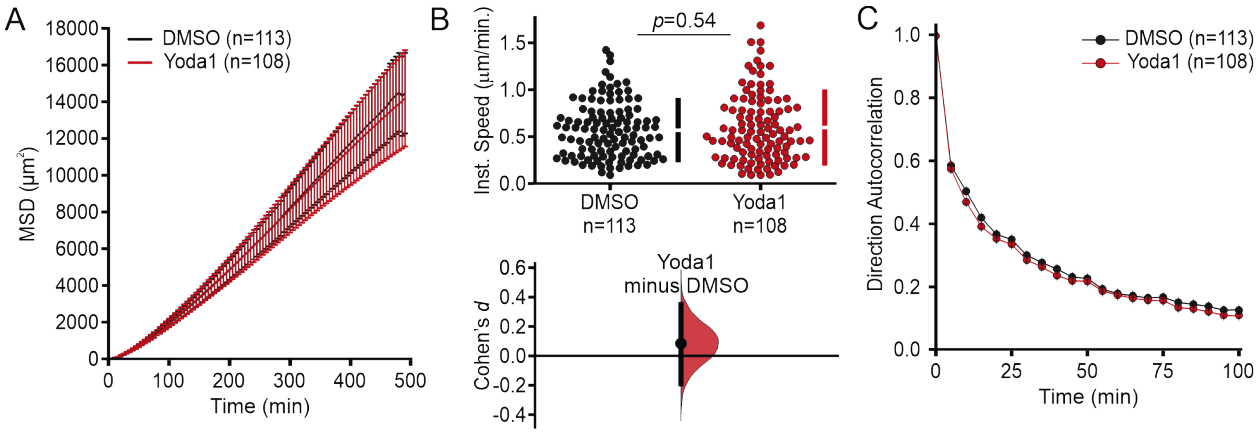

Figure A.6: **Yoda1 has no effect on single cell migration.** **(A)** Mean Squared Displacement (MSD) analysis of Yoda1-treated keratinocytes. Average MSD plotted as a function of time. **(B)** Cumming plot illustrating quantification of the average instantaneous speed from individual Yoda1-treated keratinocytes plotted against DMSO-treated Control (Cohen's d = 0.08; p value calculated via two-sample t-test). **(C)** Average direction autocorrelation of Yoda1-treated keratinocytes relative to DMSO-treated control cells plotted as a function of time. n in A-C denotes the number of tracked individually migrating keratinocytes for each condition. Related to Table 3.1; S5 Fig.

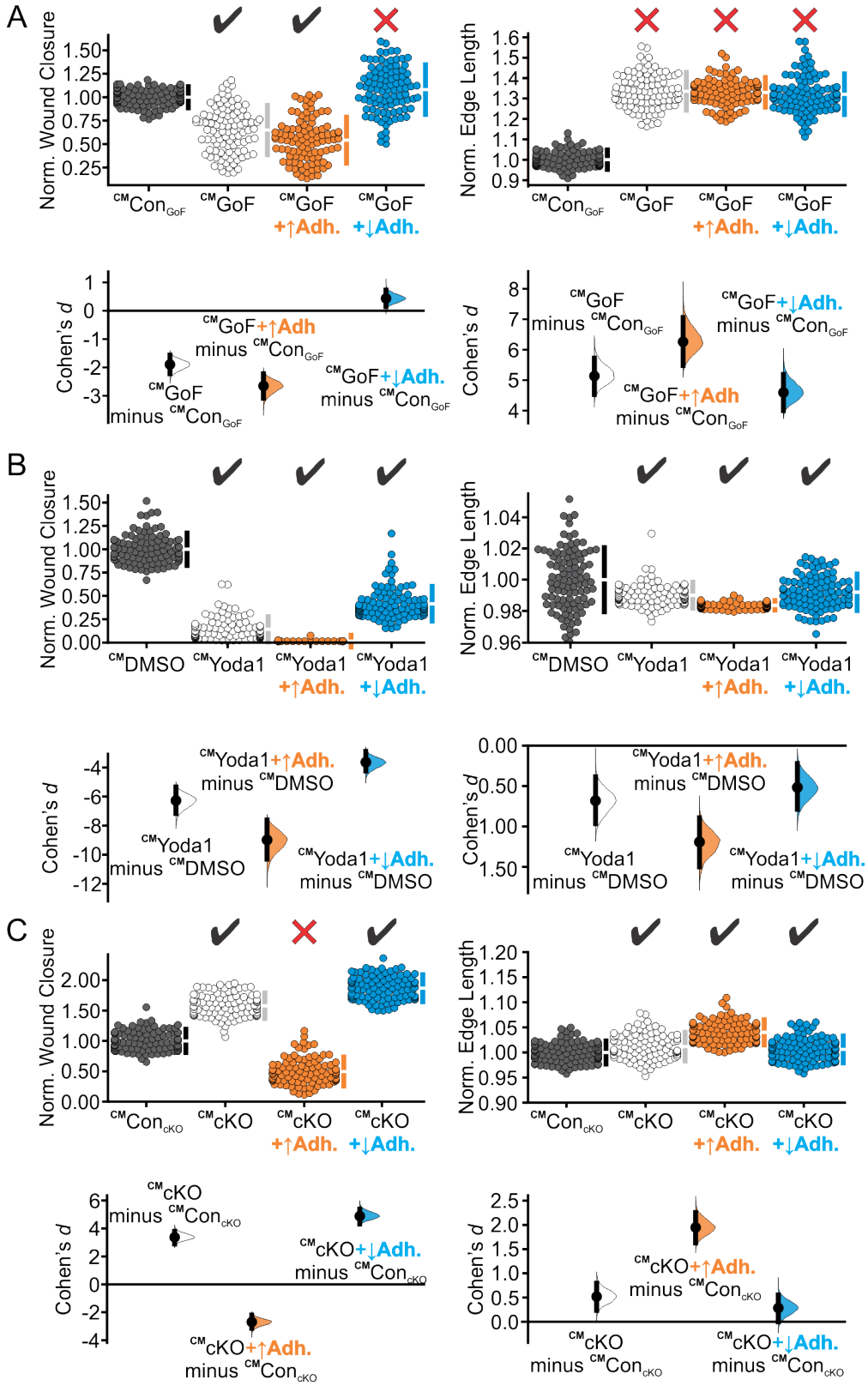

Figure A.7: **Varying cell-cell adhesion fails to match all the experimental trends.**
Figure A.7 continued on next page

Figure A.7 continued
(A) Cumming plots showing simulation results in which we use our calibrated model (^{CM}) to predict how PIEZO1 affects wound closure (*left column*) and wound edge length (*right column*) in simulated $Control_{GoF}$ monolayers (*gray*), *Piezo1*-GoF monolayers without altered adhesion parameters (*white*), *Piezo1*-GoF monolayers with increased cell-cell adhesion (*orange)* and decreased cell-cell adhesion (*blue).* **(B)** Similar to A but using simulation results from DMSO-treated monolayers (*gray*), Yoda1-treated monolayers without altered adhesion parameters (*white*), Yoda1-treated monolayers with increased cell-cell adhesion (*orange)* and decreased cell-cell adhesion (*blue).* **(C)** Similar to C but using simulation results from $Control_{cKO}$ monolayers (*gray*), *Piezo1*-cKO monolayers without altered adhesion parameters (*white*), and *Piezo1*-cKO monolayers with increased cell-cell adhesion (*orange)* and decreased cell-cell adhesion (*blue).* In A-C, n = 100 simulation results for each condition. To account for differences between control cases, data are normalized by rescaling to the mean of the corresponding control. Larger normalized wound closure indicates faster wound closure, while a smaller normalized wound closure indicates slower wound closure. Similarly, a larger normalized edge length indicates a more featured wound while a smaller normalized edge length indicates a flatter or less featured wound. Black check marks at the top of each plot condition indicate that simulation results match experimental trends while a red cross indicates the simulations fail to match the experiment results. Related to Table 3.3. For comparison with experimental data see Fig 1.1B, 1.1G and 1.1H.

Experimental/Simulation Conditions	Norm. Wound Closure	Norm. Edge Length	Experimental Match
$Control_{GoF}$ to GoF	0.718	0.885	
$^{CM}Control_{GoF}$ to ^{CM}GoF	0.650	1.335	✗
$^{CM}Control_{GoF}$ to ^{CM}GoF + cell-cell adhesion ↑	0.541	1.330	✗
$^{CM}Control_{GoF}$ to ^{CM}GoF + cell-cell adhesion ↓	1.081	1.321	✗
$^{CM}Control_{GoF}$ to ^{CM}GoF + coordinated directionality ↓	0.205	0.969	✓
DMSO to Yoda1	0.142	0.879	
^{CM}DMSO to ^{CM}Yoda1	0.142	0.990	✓
^{CM}DMSO to ^{CM}Yoda1 + cell-cell adhesion ↑	0.015	0.984	✓
^{CM}DMSO to ^{CM}Yoda1 + cell-cell adhesion ↓	0.415	0.992	✓
^{CM}DMSO to ^{CM}Yoda1 + coordinated directionality ↓	0.116	0.969	✓
$Control_{cKO}$ to cKO	1.356	1.074	
$^{CM}Control_{cKO}$ to ^{CM}cKO	1.579	1.012	✓
$^{CM}Control_{cKO}$ to ^{CM}cKO + cell-cell adhesion ↑	0.495	1.040	✗
$^{CM}Control_{cKO}$ to ^{CM}cKO + cell-cell adhesion ↓	1.867	1.006	✓
$^{CM}Control_{cKO}$ to ^{CM}cKO + coordinated directionality ↑	1.894	1.198	✓

Figure A.8: **Numerical comparisons between simulations and experiments on wound closure and edge length.** The table presents simulation results (in black, see Table 3.3 for qualitative results) obtained using the calibrated model (^{CM}) to predict the impact of PIEZO1 on normalized wound closure and normalized edge length, altering adhesion and coordinated directionality parameters. The simulation results are quantitatively compared with the corresponding experimental results (in blue, see Table 3.2 for qualitative results). Model predictions are indicated in red font with a cross mark (✗) when they do not align with the experimental trends of increasing or decreasing values. Conversely, a check mark (✓) indicates that model predictions are consistent with the experimental trends.

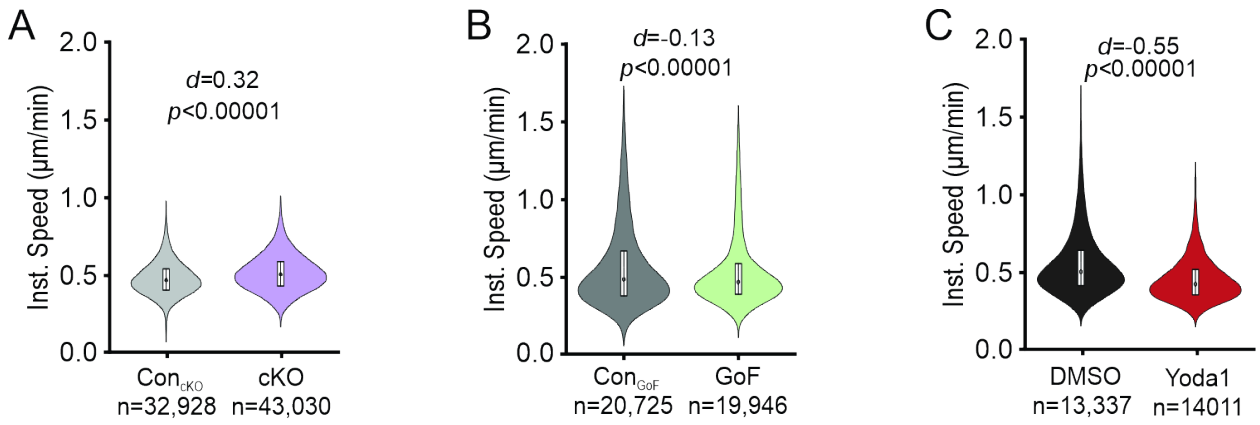

Figure A.9: **PIEZO1 inhibits keratinocyte speed during collective cell migration.** Violin plots quantifying the average instantaneous cell speed of tracked cells in **(A)** $\text{Control}_{\text{cKO}}$ vs. *Piezo1*-cKO, **(B)** $\text{Control}_{\text{GoF}}$ vs. *Piezo1*-GoF, and **(C)** DMSO-treated and 4 μM Yoda1-treated keratinocytes monolayers. For A-C, p value calculated via Mann-Whitney Test. For A-C, plotted n denotes the number of individual cell trajectories. See also Fig 3.2.

	$\text{Control}_{\text{cKO}}$	*Piezo1*-cKO	$\text{Control}_{\text{GoF}}$	*Piezo1*-GoF	DMSO	Yoda1
Length Constant	81.20 μm	102.67 μm	235.14 μm	149.60 μm	174.78 μm	116.22 μm

Figure A.10: **PIEZO1 reduces the length scale of spatial autocorrelation in keratinocytes.** Summary table showing the length constant, or the distance at which the spatial autocorrelation value is estimated to reach 0.37, for each experimental condition. Length constants were calculated by fitting a curve to the respective experimental dataset. See also Fig 3.3.

Δr (μm)	p values in Fig 5H	p values in Fig 5I	p values in Fig 5J
30	4.44×10^{-4}	8.67×10^{-6}	-
45	6.66×10^{-4}	1.13×10^{-5}	0.004
60	8.2×10^{-4}	1.23×10^{-5}	0.0021
75	0.0012	1.68×10^{-5}	-
90	0.0017	2.76×10^{-5}	0.0015
105	0.0022	4.78×10^{-5}	0.0012
120	0.0028	7.18×10^{-5}	0.0009
135	0.0032	1.39×10^{-4}	0.0012
150	0.0033	2.8×10^{-4}	0.001
165	0.004	4.55×10^{-4}	0.0015
180	0.0033	7.98×10^{-4}	0.0013
195	0.0038	0.0014	0.0013
210	0.0043	0.0023	0.0016
225	0.0044	0.0044	0.0018
240	0.0039	0.0046	0.0016
255	0.0039	0.0076	0.0027
270	0.0042	0.0132	0.0025
285	0.0037	0.0162	0.0029
300	0.0029	0.0177	0.0047
315	0.003	0.0234	0.0052
330	0.0039	0.0325	0.0063
345	0.0023	0.033	0.0087
360	0.0026	0.0291	0.0078
375	0.0025	0.0413	0.0133
390	0.0032	0.0723	0.0126
405	0.0027	0.0351	0.0151
420	0.0029	0.0479	0.0198

Figure A.11: **Specific p values for plotted points seen in Fig 3.3 H-J.**

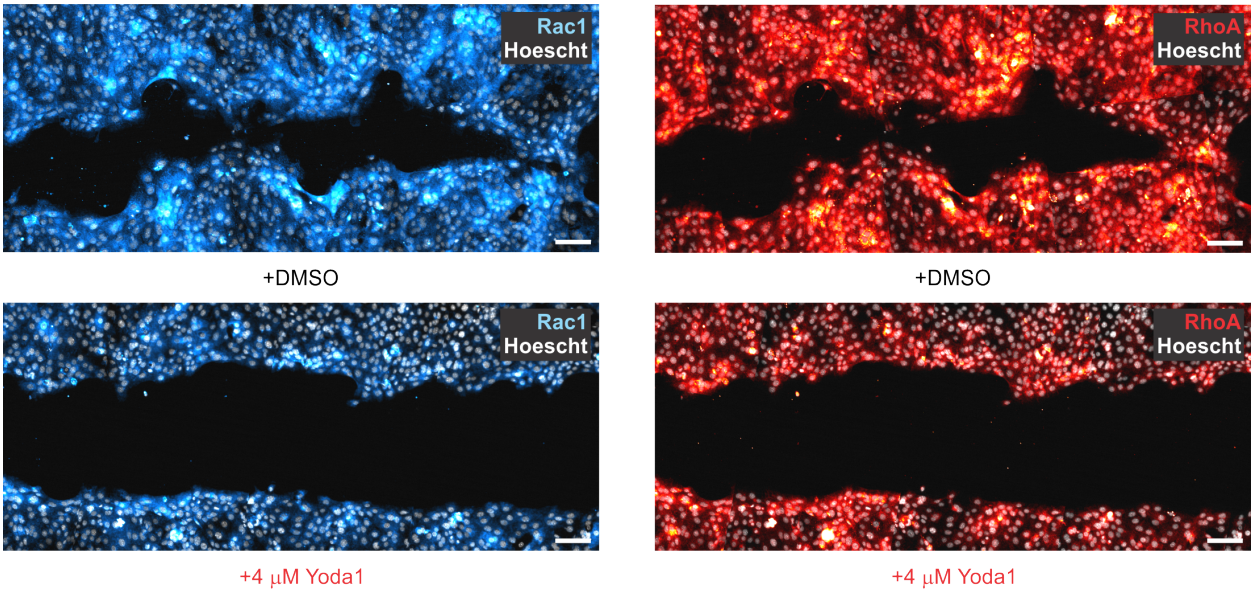

Figure A.12: **Increased PIEZO1 activity regulates Rho GTPase levels within collectively migrating monolayers.** To explore a possible relationship between PIEZO1 and Rho GTPases we performed immunocytochemistry experiments for the Rho GTPases RhoA and Rac1 within healing monolayers. Scratch wounds were generated in keratinocyte monolayers and then immediately treated with either 4 μM Yoda1, or the equivalent amount of solvent DMSO. Keratinocyte monolayers were allowed to collectively migrate for 24 hours with the respective drug in the bath media before fixing and labeling monolayers. Shown above, representative images of healing keratinocyte monolayers immuno-labeled with antibodies against Rac1 (*blue, left panels*), and RhoA (*red, right panels*) 24 hours after wounding and treating monolayers with DMSO (*top*) and 4 μM Yoda1 (*bottom*). Increasing PIEZO1 activity through Yoda1-treatment decreases Rac1 and RhoA staining suggesting that PIEZO1 activity regulates Rho GTPase expression during keratinocyte collective migration. Scale bar=100 μm.

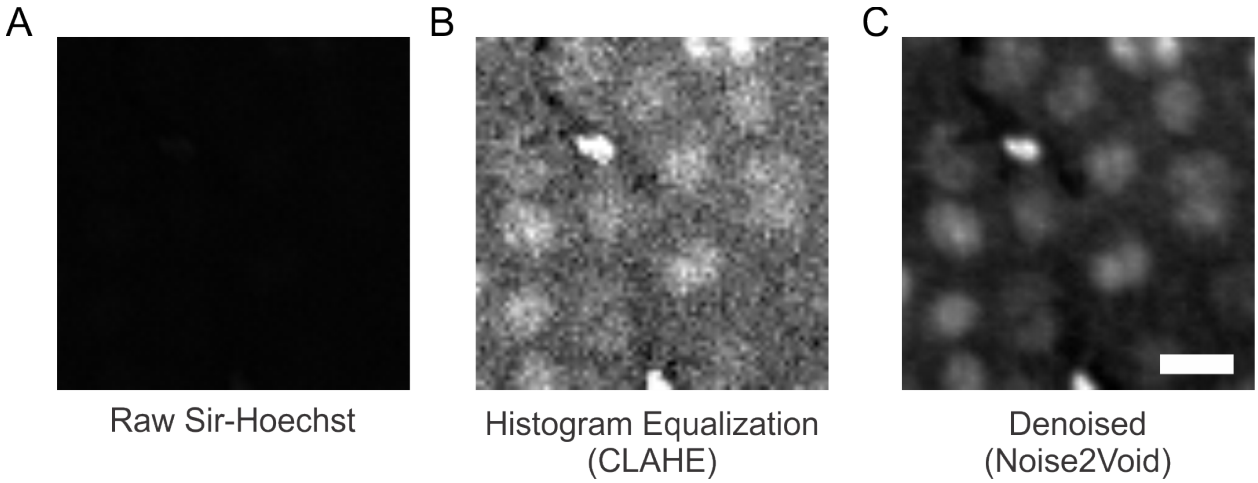

Figure A.13: **Image processing pipeline for nuclei images.** Representative images of processing steps to boost signal-to-noise ratio of **(A)** raw SiR-Hoechst images by first performing **(B)** histogram equalization using Contrast Limited Adaptive Histogram Equalization (CLAHE). **(C)** For some images, the denoising algorithm Noise2Void was used to further increase the signal-to-noise ratio of nuclei. Note: all images adjusted to the same brightness and contrast settings. Scale bar = 20 µm.

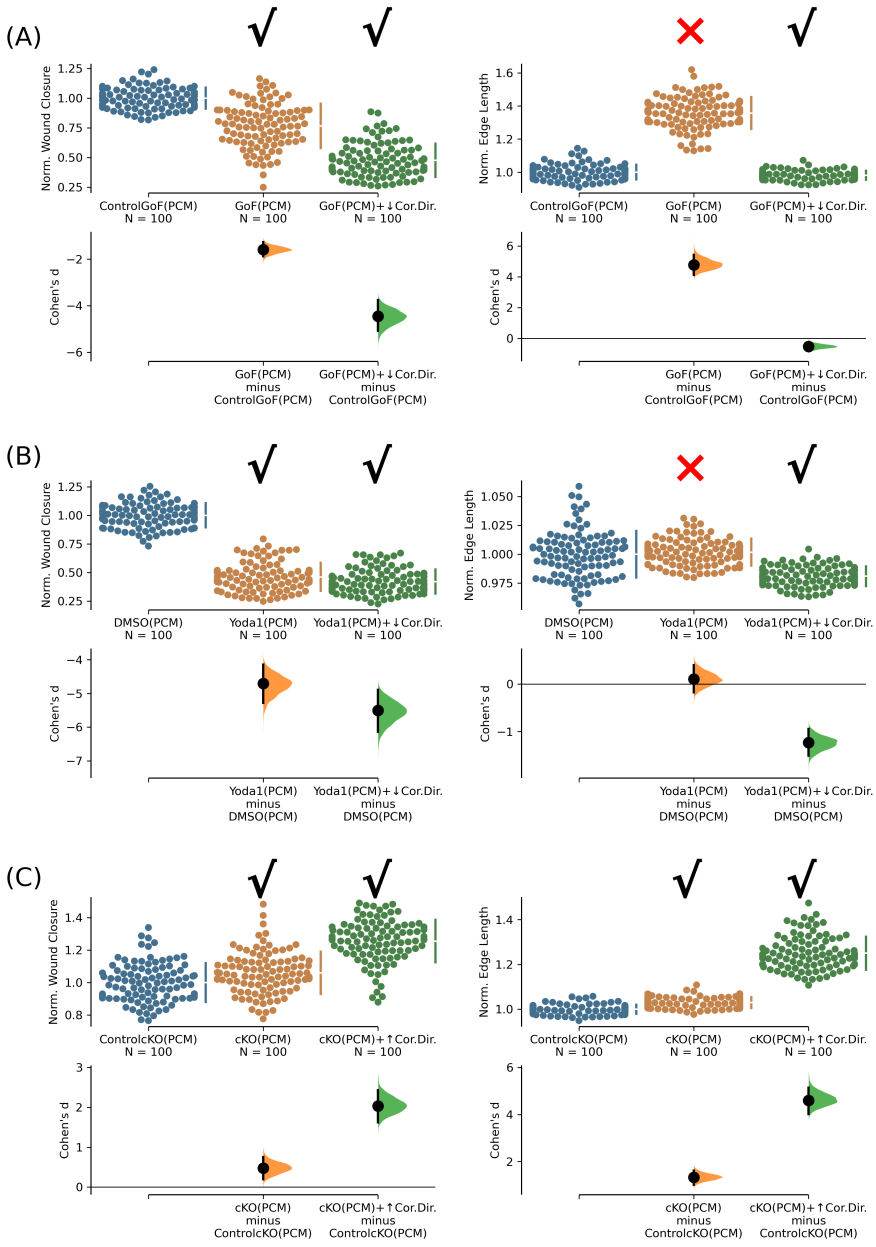

Figure A.14: **The phenomenological continuum model is consistent with the original prediction that PIEZO1 hinders coordinated directionality in wound closure.**
Figure A.14 continued on next page

Figure A.14 continued
(A) Cumming plots showing simulation results using the calibrated phenomenological continuum model (denoted as PCM, see Section 2.2.2) to predict how PIEZO1 affects normalized wound closure (*left*) and wound edge length (*right*) in simulated $\text{Control}_{\text{GoF}}$ monolayers (*blue*), *Piezo1*-GoF monolayers without altered coordinated directionality parameters (*orange*), and *Piezo1*-GoF monolayers with cell coordinated directionality decreased (*green*). See Methods Section for the details on model parameters adjustment. **(B)** Similar to A but using simulation results from DMSO-treated monolayers (*blue*), Yoda1-treated monolayers without altered coordinated directionality parameters (*orange*), and Yoda1-treated monolayers with coordinated directionality decreased (*green*). **(C)** Similar to A but using simulation results from $\text{Control}_{\text{cKO}}$ monolayers (*blue*), *Piezo1*-cKO monolayers without altered coordinated directionality parameters (*orange*), and *Piezo1*-cKO monolayers with coordinated directionality increased (*green*). In A-C, n = 100 simulation results for each condition, and CM denotes "Calibrated Model", specifically using the phenomenological continuum model in Section 2.2.2. To account for differences between control cases, data are normalized by rescaling to the mean of the corresponding control. Larger normalized wound closure indicates faster wound closure, while a smaller normalized wound closure indicates slower wound closure. Similarly, a larger normalized edge length indicates a more featured wound edge while a smaller normalized edge length indicates a flatter or less featured wound edge. Black check marks at the top of each plot condition indicate that simulation results match experimental trends while a red cross indicates simulation fails to match the experiment trends. For comparison with experimental data see Fig 1.1B, 1.1G and 1.1H.

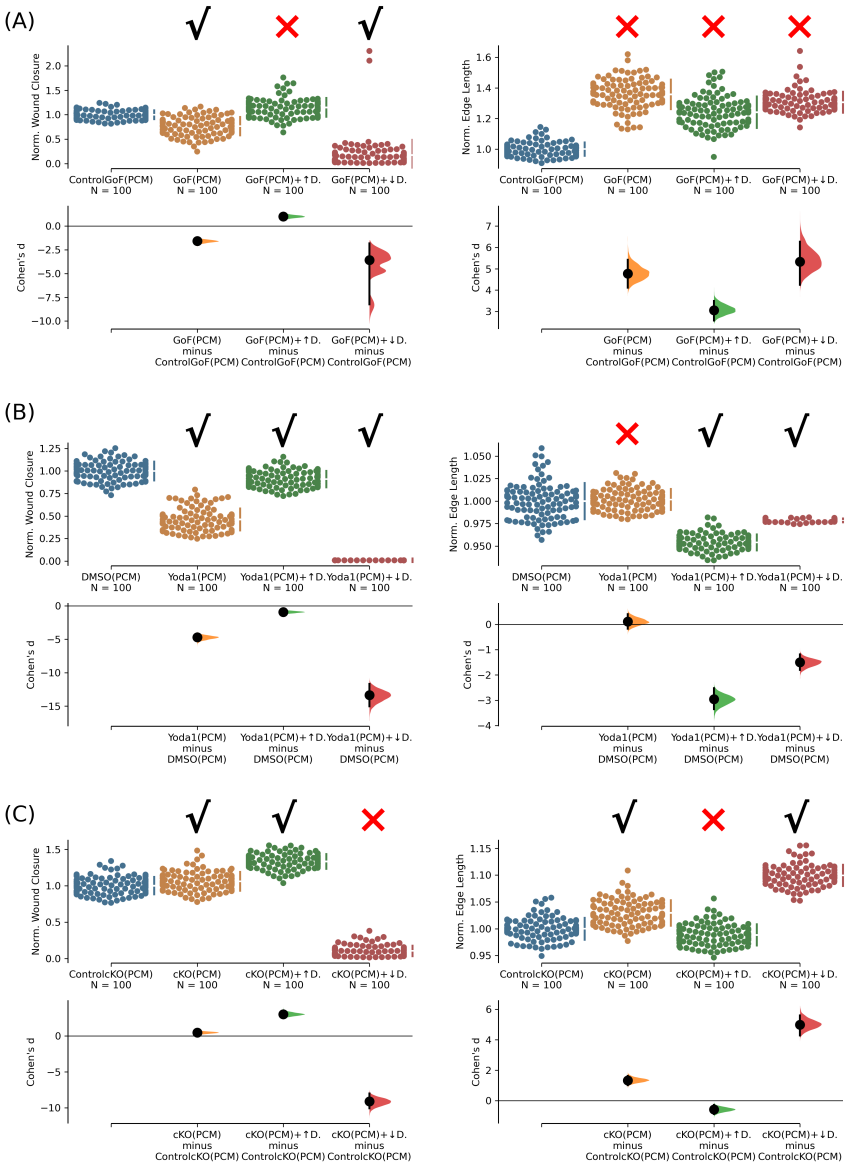

Figure A.15: **Varying the diffusion coefficient in response to changes in cell-cell adhesion fails to match all the experimental trends.**

Figure A.15 continued on next page

Figure A.15 continued
(A) Cumming plots showing simulation results in which we use the phenomenological continuum model (denoted as PCM, see Section 2.2.2) to predict how PIEZO1 affects wound closure (*left*) and wound edge length (*right*) in simulated $\text{Control}_{\text{GoF}}$ monolayers (*blue*), *Piezo1*-GoF monolayers without altered the diffusion coefficient (*orange*), *Piezo1*-GoF monolayers with increased diffusion coefficient (*green*) and decreased diffusion coefficient (*red*). The magnitude of diffusion coefficient models the combined effects of cell motility and cell-cell adhesion. **(B)** Similar to A but using simulation results from DMSO-treated monolayers (*blue*), Yoda1-treated monolayers without altered the diffusion coefficient (*orange*), Yoda1-treated monolayers with increased diffusion coefficient (*green*) and decreased diffusion coefficient (*red*). **(C)** Similar to C but using simulation results from $\text{Control}_{\text{cKO}}$ monolayers (*blue*), *Piezo1*-cKO monolayers without altered the diffusion coefficient (*orange*), and *Piezo1*-cKO monolayers with increased diffusion coefficient (*green*) and decreased diffusion coefficient (*red*). In A-C, n = 100 simulation results for each condition. To account for differences between control cases, data are normalized by rescaling to the mean of the corresponding control. Larger normalized wound closure indicates faster wound closure, while a smaller normalized wound closure indicates slower wound closure. Similarly, a larger normalized edge length indicates a more featured wound while a smaller normalized edge length indicates a flatter or less featured wound. Black check marks at the top of each plot condition indicate that simulation results match experimental trends while a red cross indicates simulation fails to match the experiment result. Related to Fig A.14. For comparison with experimental data see Fig 1.1B, 1.1G and 1.1H.

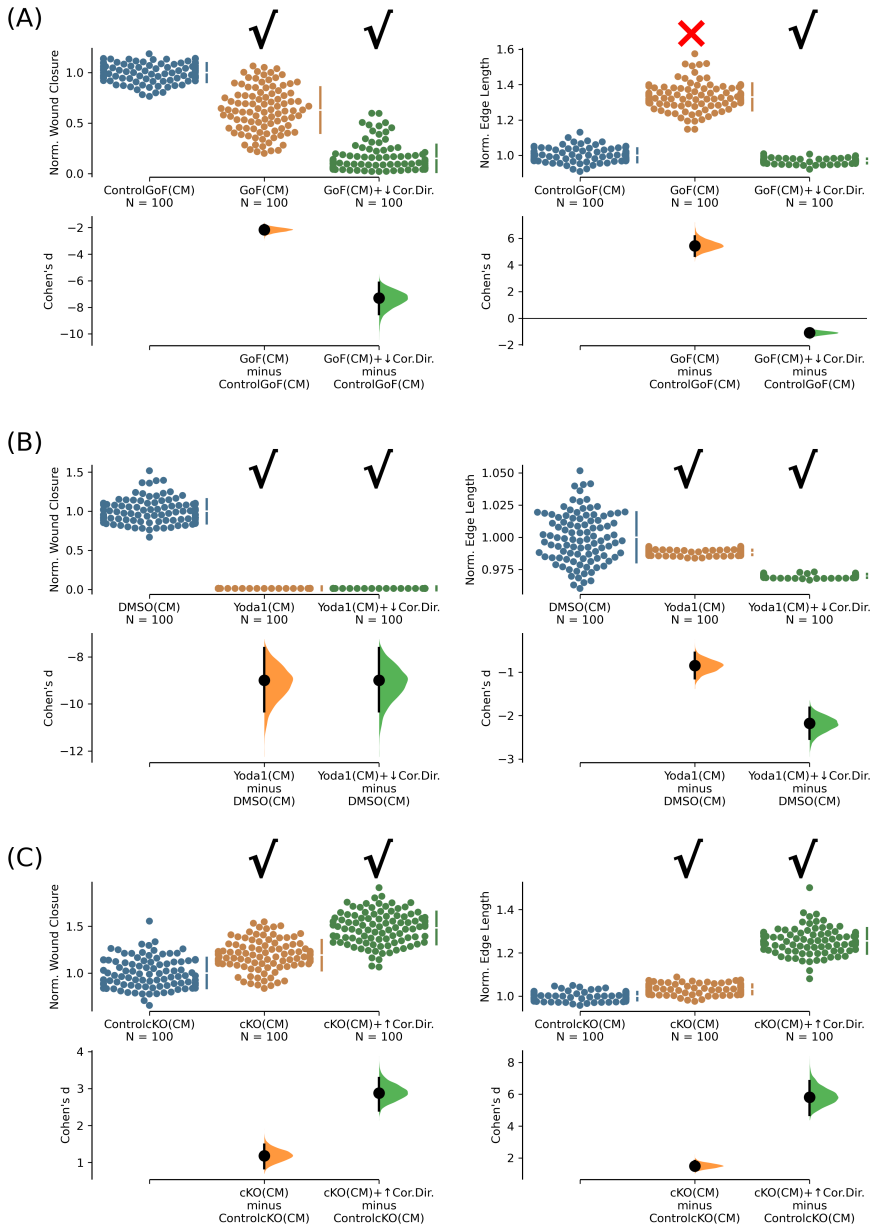

Figure A.16: **Original model calibrated by monolayer cell motilities is consistent with the original prediction that PIEZO1 hinders coordinated directionality in wound closure.**

Figure A.16 continued on next page

Figure A.16 continued
(A) Cumming plots showing simulation results from the calibrated model (CM) using cell motilities from monolayer experiments (for data see S9 Fig, for detailed model calibration see Section 3.4.2) to predict how PIEZO1 affects normalized wound closure (*left*) and wound edge length (*right*) in simulated $\text{Control}_{\text{GoF}}$ monolayers (*blue*), *Piezo1*-GoF monolayers without altered coordinated directionality parameters (*orange*), and *Piezo1*-GoF monolayers with coordinated directionality decreased (*green*). See Methods Section for the details on model parameters adjustment. **(B)** Similar to A but using simulation results from DMSO-treated monolayers (*blue*), Yoda1-treated monolayers without altered coordinated directionality parameters (*orange*), and Yoda1-treated monolayers with coordinated directionality decreased (*green*). **(C)** Similar to A but using simulation results from $\text{Control}_{\text{cKO}}$ monolayers (*blue*), *Piezo1*-cKO monolayers without altered coordinated directionality parameters (*orange*), and *Piezo1*-cKO monolayers with coordinated directionality increased (*green*). In A-C, n = 100 simulation results for each condition, and CM denotes "Calibrated Model", specifically our original model using cell motilities from monolayer experiments (Section 3.4.2). To account for differences between control cases, data are normalized by rescaling to the mean of the corresponding control. Larger normalized wound closure indicates faster wound closure, while a smaller normalized wound closure indicates slower wound closure. Similarly, a larger normalized edge length indicates a more featured wound while a smaller normalized edge length indicates a flatter or less featured wound. Black check marks at the top of each plot condition indicate that simulation results match experimental trends while a red cross indicates simulation fails to match the experiment trends. For comparison with experimental data see Fig 1.1B, 1.1G and 1.1H.

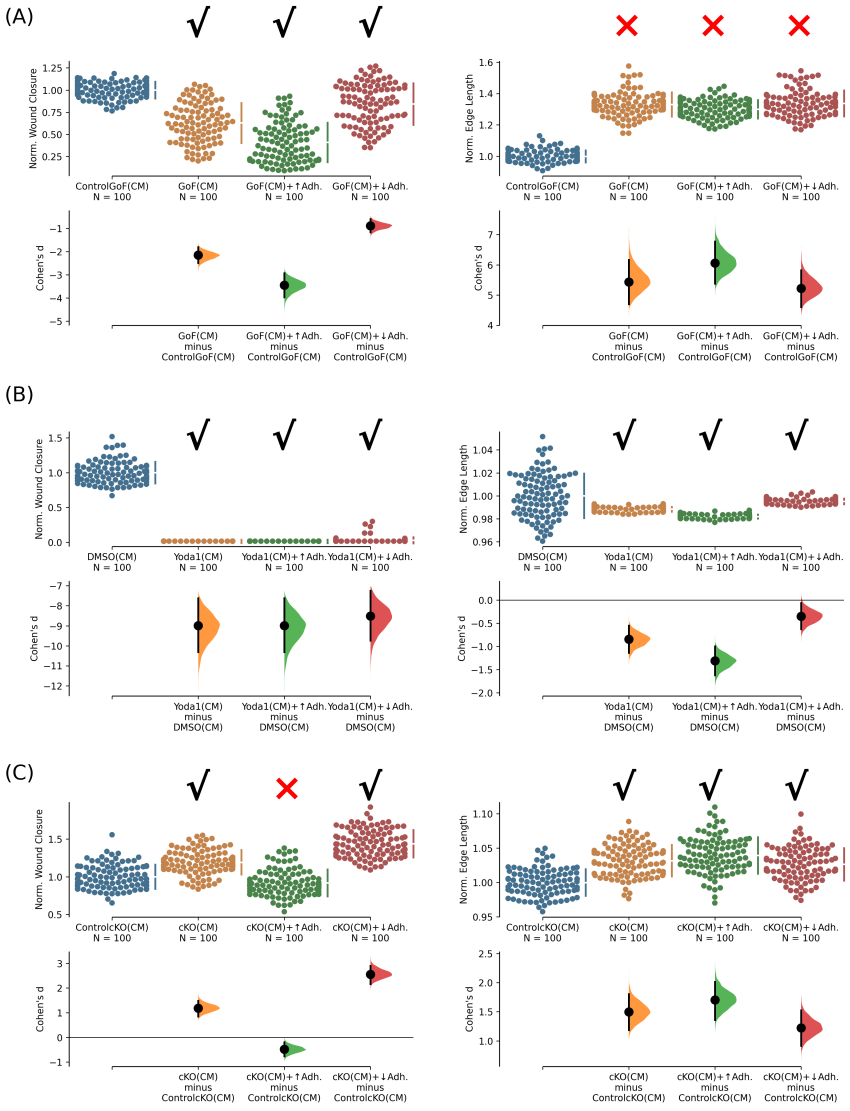

Figure A.17: **Varying cell-cell adhesion in the original model, calibrated by the monolayer cell motilities, fails to match some experimental trends.**
Figure A.17 continued on next page

Figure A.17 continued
(A) Cumming plots showing simulation results in which we use our calibrated model using cell motilities from monolayer experiments (denoted as CM, see Section 3.4.2) to predict how PIEZO1 affects wound closure (*left*) and wound edge length (*right*) in simulated $\text{Control}_{\text{GoF}}$ monolayers (*blue*), *Piezo1*-GoF monolayers without altered the cell-cell adhesion parameter (*orange*), *Piezo1*-GoF monolayers with increased cell-cell adhesion (*green*) and decreased cell-cell adhesion (*red*). **(B)** Similar to A but using simulation results from DMSO-treated monolayers (*blue*), Yoda1-treated monolayers without altered the cell-cell adhesion parameter (*orange*), Yoda1-treated monolayers with increased cell-cell adhesion (*green*) and decreased cell-cell adhesion (*red*). **(C)** Similar to C but using simulation results from $\text{Control}_{\text{cKO}}$ monolayers (*blue*), *Piezo1*-cKO monolayers without altered the cell-cell adhesion parameter (*orange*), and *Piezo1*-cKO monolayers with increased cell-cell adhesion (*green*) and decreased cell-cell adhesion (*red*). In A-C, n = 100 simulation results for each condition. To account for differences between control cases, data are normalized by rescaling to the mean of the corresponding control. Larger normalized wound closure indicates faster wound closure, while a smaller normalized wound closure indicates slower wound closure. Similarly, a larger normalized edge length indicates a more featured wound while a smaller normalized edge length indicates a flatter or less featured wound. Black check marks at the top of each plot condition indicate that simulation results match experimental trend while a red cross indicates simulation fails to match the experiment result. Related to Fig A.16. For comparison with experimental data see Fig 1.1B, 1.1G and 1.1H.

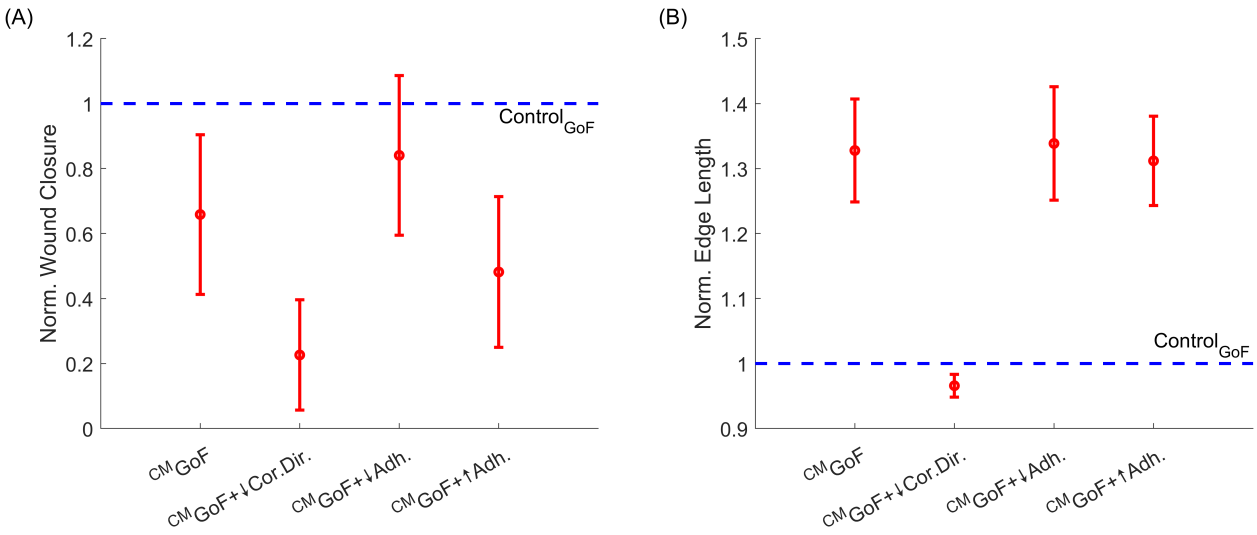

Figure A.18: **Varying the magnitudes of the retraction processes in the original model (see text) yields results that are consistent with the original prediction that PIEZO1 hinders coordinated directionality in wound closure. (A)** Dot plots illustrate the mean of 2700 simulation results from the model using three values of the magnitudes of the retraction processes. They depict how PIEZO1 influences normalized wound closure in *Piezo1*-GoF monolayers compared to simulated $\text{Control}_{\text{GoF}}$ monolayers (*blue dashed line*). The scenarios include *Piezo1*-GoF monolayers without altered coordinated directionality and cell-cell adhesion parameters (*first column*), *Piezo1*-GoF monolayers with decreased coordinated directionality (*second column*), *Piezo1*-GoF monolayers with decreased cell-cell adhesion (*third column*), and *Piezo1*-GoF monolayers with increased cell-cell adhesion (*fourth column*). See Section 3.4.2 for the details on the model parameters. Error bars indicate the standard deviation. **(B)** Similar to A but measuring the changes in normalized edge length instead of normalized wound closure.

Appendix B

Supplementary materials for the heterogeneous model

B.1 Heterogeneous Model

B.1.1 Retraction is modeled by advection

Performing a Taylor expansion on the cell densities u and v, centered at $\boldsymbol{x} = \boldsymbol{x}_{i,j}$, in the discrete master equation for u cells (Eq. 4.1) without specifying $b^{\rightarrow}_{u,i,j}$, we obtain:

$$\partial_t u = \nabla \cdot \left(\boldsymbol{D}_{11} \nabla u + \boldsymbol{D}_{12} \nabla v + h \cdot (1-u-v)(1-\alpha_{uu}u - \alpha_{uv}v)^3 \cdot (b_u^{\leftarrow} - b_u^{\rightarrow}, b_u^{\uparrow} - b_u^{\downarrow})^T \right) + \mathcal{O}(h^2) \tag{B.1}$$

where $\boldsymbol{D}_{11}$ and $\boldsymbol{D}_{12}$ are the same diffusivities as in Eq. 4.7. By taking $h \to 0$, the continuum limit would be derived to be a simple diffusion equation as in Eq. 4.13 without an advection term, unless both $\Delta b_u^{\leftrightarrow} = b_u^{\leftarrow} - b_u^{\rightarrow}$ and $\Delta b_u^{\updownarrow} = b_u^{\uparrow} - b_u^{\downarrow}$ are $\mathcal{O}(1/h)$, indicating advection

scaling. Therefore, we define $b^{\rightarrow}_{u,i,j} := r^{\rightarrow}_{u,i,j}/h$ with $r^{\rightarrow}_{u,i,j} \in \mathcal{O}(1)$. By taking $h \to 0$ under this setting, Eq. B.1 turns into our continuum limit for u cells in Eq. 4.6, where the retraction is modeled by advection. Analogous steps can be applied for v cells, emphasizing the role of advection in representing cell retraction dynamics.

B.1.2 The effect of cell-cell adhesion between same cell types on wound closure

In the context of increased adhesion between $\text{Control}_{\text{cKO}}$ cells (Fig. B.1B, $\alpha_{uu} = 0.3$) compared to the baseline value (Fig. B.1A, $\alpha_{uu} = 0.2$), there is a reduction in wound closure (Fig. B.1B, left endpoint) compared to the base case (Fig. B.1A, left endpoint), reflecting the hindering effect of cell-cell adhesion on the wound closure [35, 37]. The mixture (where $0 < p_v < 1$) is also impacted by the increased α_{uu}, exhibiting varying degrees of reduction in normalized wound closure (Fig. B.1B) compared to the base case (Fig. B.1A). A smaller p_v, indicating a larger proportion of u cells, results in a greater reduction in normalized wound closure attributed to u cells (Fig. B.1B) compared to the base case (Fig. B.1A). Based on Fig. B.1B, we subsequently decrease the adhesion between *Piezo1*-cKO cells from $\alpha_{vv} = 0.2$ to $\alpha_{vv} = 0.1$, leading to faster wound closure in Fig. B.1C (right endpoint) compared to the scenario in Fig. B.1B (right endpoint). The higher proportion of v cells (close to the right endpoint in Fig. B.1C) corresponds to a greater enhancement in the wound closure rate compared to Fig. B.1B. Similar adjustments to α_{uu} and α_{vv} were applied in other mixtures (Fig. B.1D-B.1F for mixing $\text{Control}_{\text{GoF}}$ and *Piezo1*-GoF, and Fig. B.1G-B.1I for mixing *Piezo1*-cKO and Yoda1-treated cells). Consequently, the spindle pattern for normalized wound closure in these mixtures exhibits similar changes to those observed in the mixture of $\text{Control}_{\text{cKO}}$ and *Piezo1*-cKO (Fig. B.1A-B.1C).

Conversely, we also adjusted the cell-cell adhesion by decreasing α_{uu} and increasing α_{vv} in

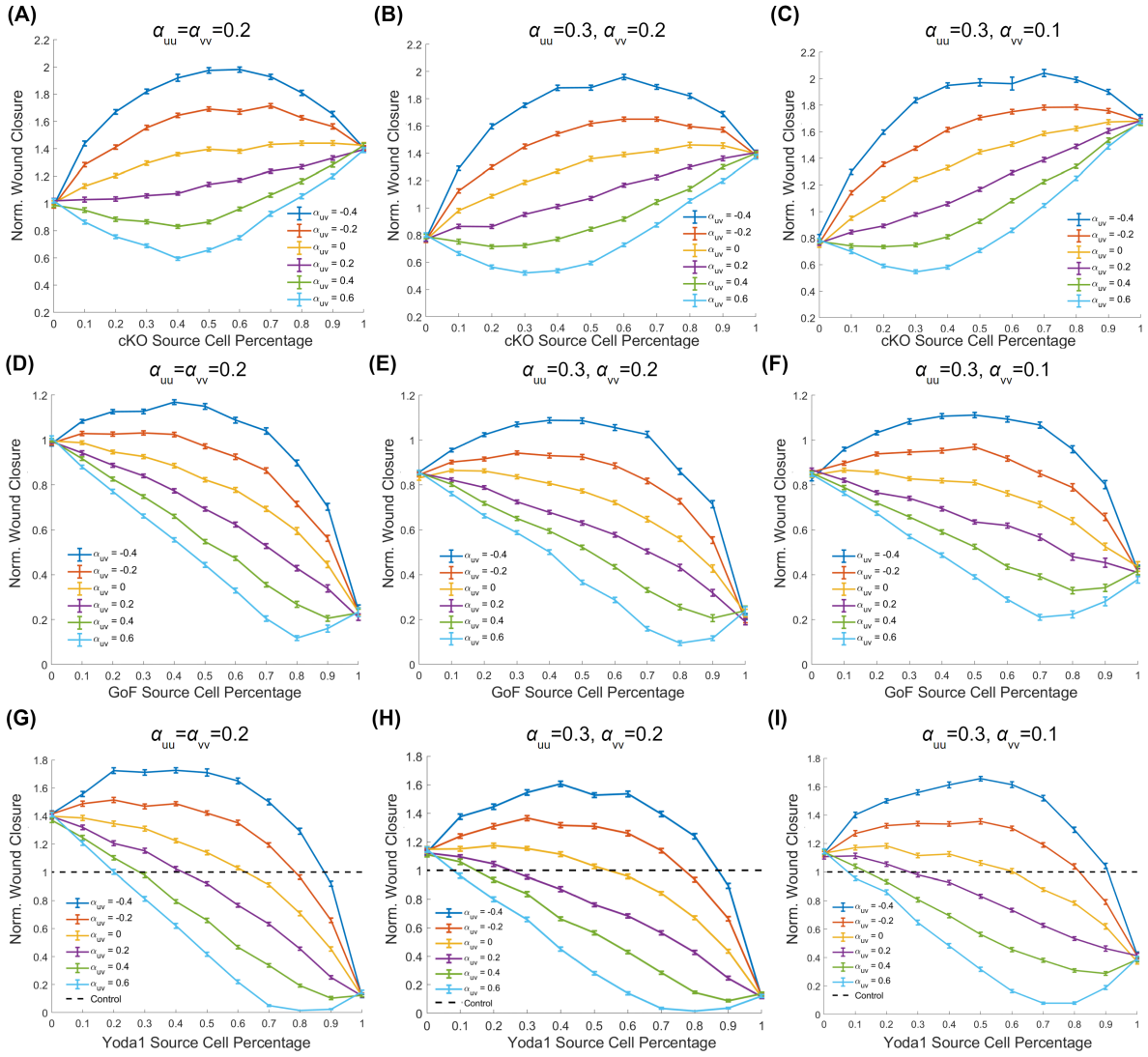

Figure B.1: **The impact of increased α_{uu} and decreased α_{vv} on wound closure rate.** **(A)** Line graphs illustrate the mean of 100 simulation results involving mixtures of $\text{Control}_{\text{cKO}}$ (u cells) and *Piezo1*-cKO (v cells), displaying the normalized wound closure versus the *Piezo1*-cKO source cell percentage under $\alpha_{uu} = \alpha_{vv} = 0.2$. Error bars indicate the standard error of the mean. The various colored lines denote different interaction coefficient values (α_{uv}). The data are also shown in Fig. 4.1B but are reproduced here for ease of comparison. **(B)** Similar to (A) but $\alpha_{uu} = 0.3$ and $\alpha_{vv} = 0.2$. **(C)** Similar to (A) but $\alpha_{uu} = 0.3$ and $\alpha_{vv} = 0.1$. **(D-F)** Depict similar scenarios to (A-C), but involving mixtures of *Piezo1*-GoF (v cells) with their respective wild-type control (u cells). The data in (D) are also presented in Fig. 4.1D but are replicated here for ease of comparison. **(G-I)** Also akin to (A-C), but featuring mixtures of *Piezo1*-cKO (u cells) and Yoda1-treated cells (v cells). The black dashed lines denote the unit normalized wound closure, representing the rate of wound closure of wild-type control. The data in (G) are also shown in Fig. 4.1F but are reproduced here for ease of comparison.

various mixtures (Fig. B.2). As a result, the normalized wound closure for mixtures with a higher proportion of u cells slowed down, whereas mixtures with a higher proportion of v cells closed the wound faster.

B.1.3 Self-mixture of wild-type control cells

To investigate the influence of model parameters (e.g., α_{uv} and p_v) on wound closure rate and wound edge cell distribution, it is beneficial to mix one cell type with another type that shares the same set of model parameters. For instance, mixing $\text{Control}_{\text{cKO}}$ with itself allows the effects of model parameters to be isolated from PIEZO1 phenotypes, providing a clearer understanding of their regulation on wound closure. When mixing $\text{Control}_{\text{cKO}}$ with itself in the model simulation and observing the rate of wound closure over p_v under various α_{uv} conditions, we observed a roughly symmetrical horizontal spindle pattern (Fig. B.3A). Similar to Fig. 4.1B, but more clearly, the lines can be categorized into three groups based on their convexity:

1. When the interaction coefficient is set to $\alpha_{uv} = \alpha_{uu} = \alpha_{vv} = 0.2$, the adhesion effects between any cells are indistinguishable. As a result, the wound closure for mixed cell migration represents a simple interpolation between solely u cells (left spindle pole in Fig. B.3A) and solely v cells (right spindle pole in Fig. B.3A), demonstrating a horizontal line (the purple line in Fig. B.3A).

2. When the interaction coefficient $\alpha_{uv} > 0.2$, the hindering adhesion effect between different u and v cells becomes stronger than the adhesion effect within the same cell types ($\alpha_{uu} = \alpha_{vv} = 0.2$). In this scenario, when cells are more evenly mixed (e.g., 50% u cells mixed with 50% v cells), the role played by interaction coefficient becomes more significant, resulting in slower collective cell migration and displaying a convex "U-shaped" line (e.g., the bottom line in light blue in Fig. B.3A).

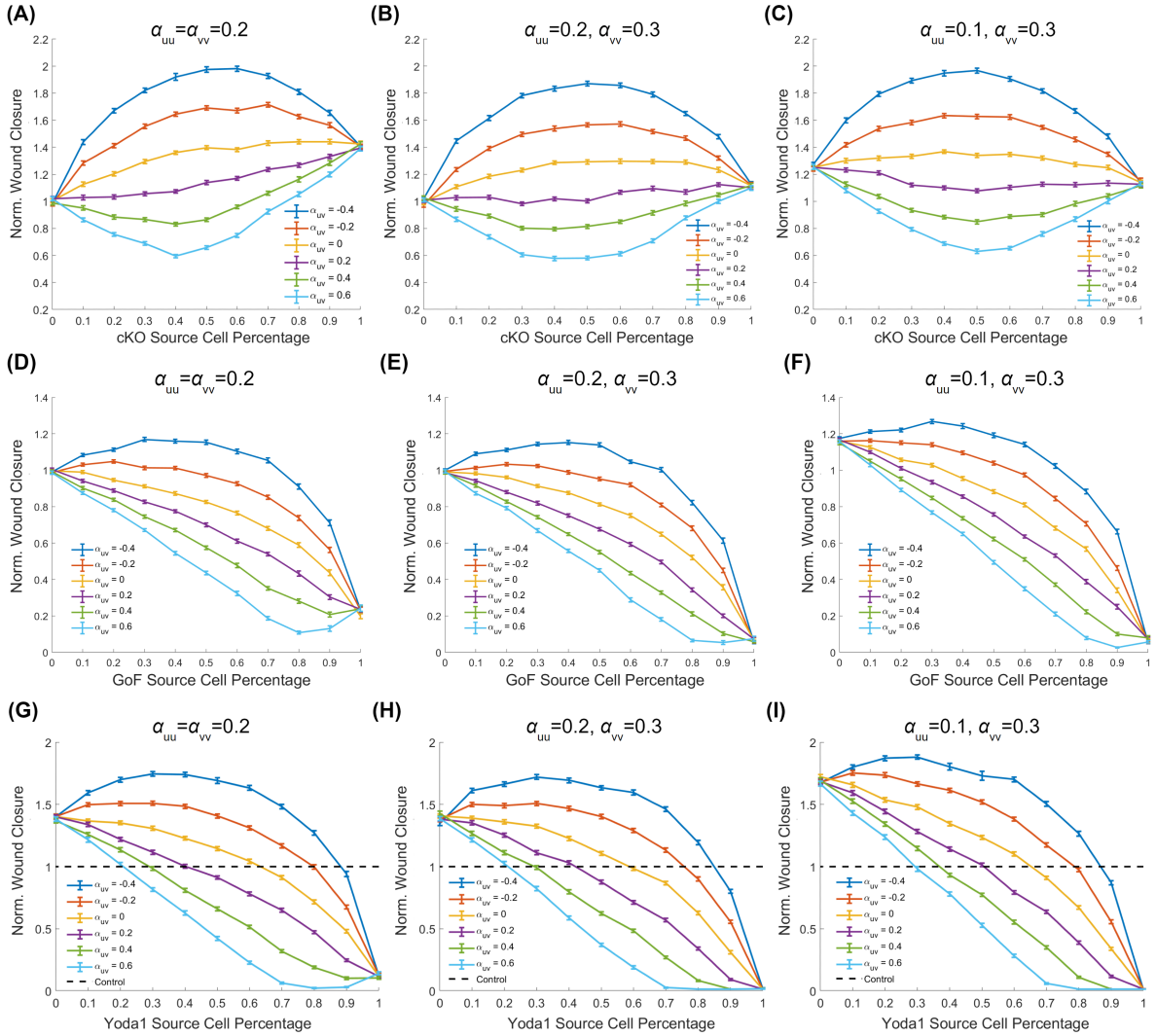

Figure B.2: **The impact of decreased α_{uu} and increased α_{vv} on wound closure rate.** **(A)** Line graphs illustrate the mean of 100 simulation results involving mixtures of $\text{Control}_{\text{cKO}}$ (u cells) and *Piezo1*-cKO (v cells), displaying the normalized wound closure versus the *Piezo1*-cKO source cell percentage under $\alpha_{uu} = \alpha_{vv} = 0.2$. Error bars indicate the standard error of the mean. The various colored lines denote different interaction coefficient values (α_{uv}). The data are also presented in Fig. 4.1B but are replicated here for comparison convenience. **(B)** Similar to (A) but $\alpha_{uu} = 0.2$ and $\alpha_{vv} = 0.3$. **(C)** Similar to (A) but $\alpha_{uu} = 0.1$ and $\alpha_{vv} = 0.3$. **(D-F)** Depict similar scenarios to (A-C), but involving mixtures of *Piezo1*-GoF (v cells) with their respective wild-type control (u cells). The data in (D) are also shown in Fig. 4.1D but are replicated here for ease of comparison. **(G-I)** Also akin to (A-C), but featuring mixtures of *Piezo1*-cKO (u cells) and Yoda1-treated cells (v cells). The black dashed lines denote the unit normalized wound closure, representing the rate of wound closure of wild-type control. The data in (G) are also shown in Fig. 4.1F but are reproduced here for ease of comparison.

3. Conversely, when the interaction coefficient $\alpha_{uv} < 0.2$, cells are more likely to migrate away from the adhesion between different cell types compared to the adhesion between the same cell types. The expelling effect occurs when $\alpha_{uv} < 0$ becomes negative, causing cell-cell interaction between u and v cells to propel cells toward cell-free regions. Consequently, the faster wound closure rate in the mixture results in a concave up "bridge-shaped" line (e.g., the top line in dark blue in Fig. B.3A).

A similar pattern was observed when mixing $\text{Control}_{\text{GoF}}$ with itself, albeit with variations in the scale of changes in normalized wound closure (Fig. B.3B).

Mixing wild-type control cells to isolate the impact of the PIEZO1 phenotype also facilitates the investigation of cell distribution near wound edges. This approach yields a symmetric "double spindle" pattern when plotting the edge cell percentage of v cells over p_v under various α_{uv} conditions (Fig. B.3C and B.3D). In this pattern, lines are roughly symmetrically distributed around the line representing $\alpha_{uv} = 0.2$, which approximately overlaps with $y = x$. This symmetry arises because the indistinguishable cell-cell interaction ($\alpha_{uu} = \alpha_{vv} = \alpha_{uv} = 0.2$) ensures that u cells and v cells perform identical roles in the mixture, differing only in notation. Consequently, we do not anticipate any over- or under-representation of one cell type over the other.

Upon closer examination of the double spindle patterns in Fig. B.3C and B.3D, it becomes evident that higher interaction coefficient tends to impede the migration of v cells toward the wound edge when the proportion of v cells is lower than that of u cells. Conversely, it facilitates the migration of v cells toward the wound edge when the proportion of v cells exceeds that of u cells. In contrast, lower interaction coefficient, especially negative α_{uv}, exhibits the opposite effect. It accelerates v cells' migration toward the edge when the proportion of v cells is lower than u cells and slows down v cells' movement toward the wound edge when the proportion of v cells is higher than u cells (see Table B.1 for a summary).

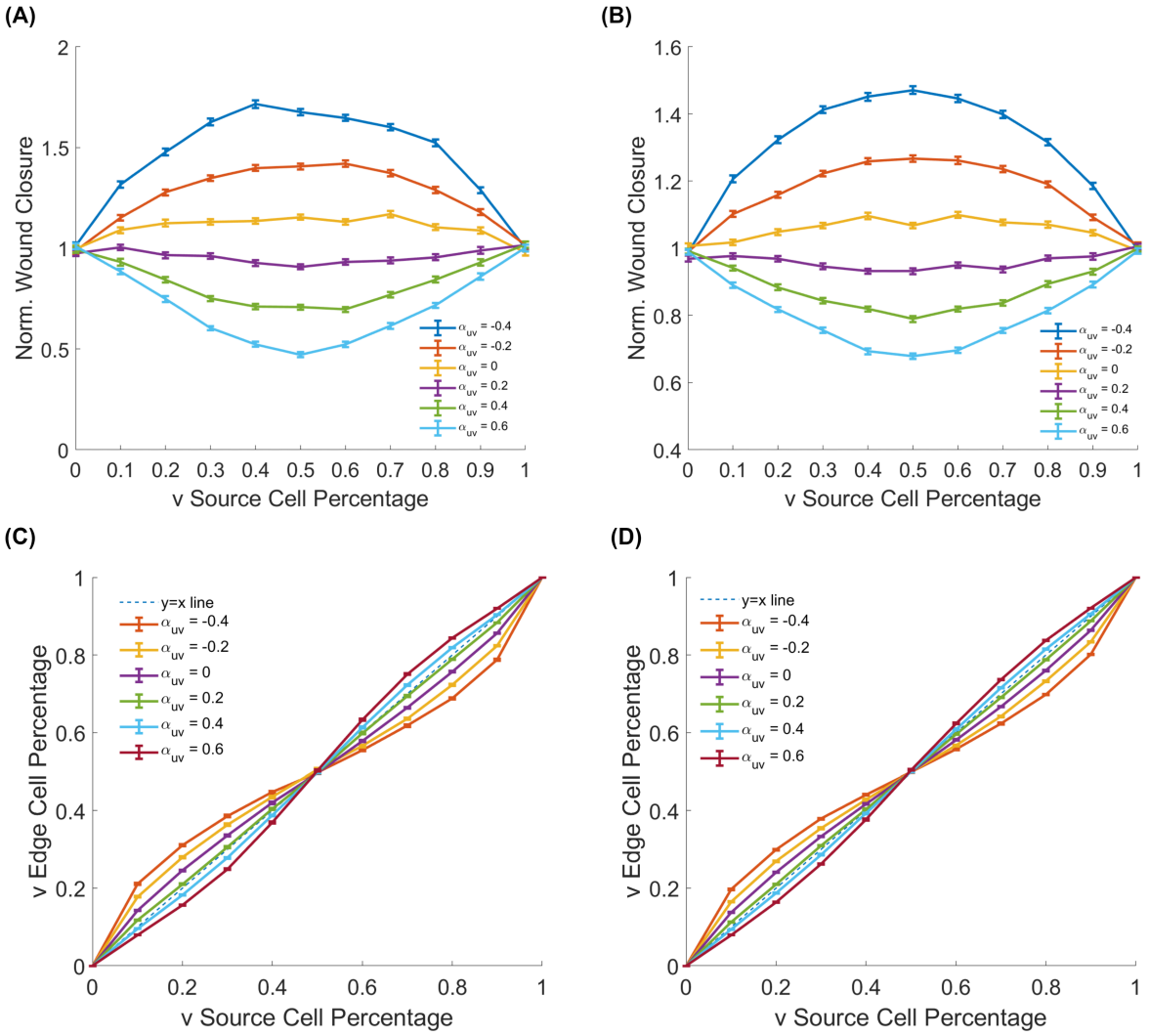

Figure B.3: **The self-mixture of wild-type control cells.** **(A)** Line graphs illustrate the mean of 100 simulation results involving mixtures of $\text{Control}_{\text{cKO}}$ (u cells) and $\text{Control}_{\text{cKO}}$ (v cells), displaying the normalized wound closure versus the source cell percentage for v cells under $\alpha_{uu} = \alpha_{vv} = 0.2$. Error bars indicate the standard error of the mean. The various colored lines denote different interaction coefficient values (α_{uv}). **(B)** Similar to (A) but for mixing $\text{Control}_{\text{GoF}}$ (u cells) and $\text{Control}_{\text{GoF}}$ (v cells). **(C)** Line graphs illustrate the mean of 100 simulation results from modeling the mixtures of $\text{Control}_{\text{cKO}}$ (u cells) and $\text{Control}_{\text{cKO}}$ (v cells), displaying the percentage of v cells in edge cells versus the percentage in source cells. The various colored lines denote different interaction coefficient values (α_{uv}), and error bars indicate the standard error of the mean. **(D)** Depict similar scenarios to (C), but involving the mixture of $\text{Control}_{\text{GoF}}$ (u cells) and $\text{Control}_{\text{GoF}}$ (v cells).

	$p_u < p_v$	$p_u > p_v$
$\alpha_{uv} < \alpha_{uu} = \alpha_{vv}$	u cells $(+)$ v cells $(-)$	u cells $(-)$ v cells $(+)$
$\alpha_{uv} > \alpha_{uu} = \alpha_{vv}$	u cells $(-)$ v cells $(+)$	u cells $(+)$ v cells $(-)$

Table B.1: **Edge cell representation in the self mixture.** Summary table presenting the edge cell representation in the self mixture, i.e., u and v model the same type of cells. In this table, a "+" indicates an over-representation of u (or v) cells in wound edge cells, indicating that the percentage of u (or v) cells near the wound edge is higher than its percentage in source cells p_u (or p_v). Conversely, a "−" indicates an under-representation of u (or v) cells in wound edge cells, implying that the percentage of u (or v) cells near the wound edge is lower than the percentage in source cells p_u (or p_v). A "+" for v cells corresponds to a concave upward trend in lines, while a "−" for v cells corresponds to a concave downward trend in lines (Fig. B.3C and B.3D).

The explanation for these observations is as follows:

When the interaction coefficient exceeds 0.2, the cell type that constitutes a larger proportion tends to move faster. This is because their migration is minimally influenced by the substantial interaction coefficient due to the small proportion of their interacting counterpart, which has a limited effect in impeding their movement. For instance, if u cells dominate over v cells, the diffusion part of the governing equation for u cells contains the term $1-\alpha_{uu}u-\alpha_{uv}v$ (Eq. 4.9). Here, a large value of α_{uv} has little hindering effect on the migration of u because v is small. In contrast, the diffusivity of v cells contains the term $1-\alpha_{vv}v-\alpha_{uv}u$, indicating that the migration of v cells is significantly hindered by a large interaction coefficient α_{uv} because the cell density of u cells is high, amplifying the hindering effect of the substantial interaction coefficient. A similar rationale applies when the interaction coefficient is below 0.2, where the cell type constituting a smaller proportion moves faster since they contact with a larger portion of the different cell type with lower interaction coefficient. In conclusion, the presence of the "double spindle" pattern arises from the fact that both the hindering effect of high cell-cell adhesion and the promoting effect of repulsive cell-cell interaction exert a larger impact on cells with a smaller proportion in the mixture compared to those with a larger proportion.

By comparing the "double spindle" pattern observed earlier (Fig. 4.2G-4.2I) with the self-

mixture results (Fig. B.3C and B.3D), the down-regulation impact of PIEZO1 activity on the edge cell representation becomes evident. It's important to note that if u and v represent the same type of cell for mixing, the mixture will not regress to a homogeneous single type of cell scenario. This is because our mathematical model assumes that u cells and v cells have independent stochastic retractions. Therefore, even if u and v cells share the same set of model parameters (e.g., $\mu_{s,u} = \mu_{s,v}$, $\mu_{r,u} = \mu_{r,v}$, etc.), it only means that their retraction events are generated from the same distribution. However, the same distribution can produce different random values for u and v cells. Only when individual retraction events applied to u and v cells are identical, rather than just their random distributions being the same, will the heterogeneous case converge to the homogeneous case.

B.1.4 The cell density threshold for wound edge cells

In the self-mixture of wild-type control cells, we expect to observe the same fraction of v cells in wound edge cells (where $u + v < \gamma_{\text{edge}}$) for any fraction of v in the entire monolayer. This expectation implies that plotting the relationship between the percentage of v cells in $u + v < \gamma_{\text{edge}}$ and the percentage of v cells everywhere (p_v) should result in an overlap with the $y = x$ line. However, this alignment does not hold when γ_{edge} is too small (e.g., $\gamma_{\text{edge}} = 0.05$ in Fig. B.4). Therefore, we gradually increase the value of γ_{edge} from a relatively small value until the curve roughly aligns with the $y = x$ line and ceases to change noticeably with further increases in γ_{edge}. The minimal γ_{edge} that satisfies this condition serves as the threshold we sought, and it was determined to be 0.2 (Fig. B.4 and B.5).

When γ_{edge} is too small to define the "wound edge cells," it leads to an overestimation of the "edge percentage" of cells with a small fraction in the mixture, consequently underestimating the "edge percentage" of cells with a large fraction in the mixture. For instance, setting $\gamma_{\text{edge}} = 0.05$ for wound edge cells in the self-mixture of $\text{Control}_{\text{cKO}}$ (as shown in Fig. B.4),

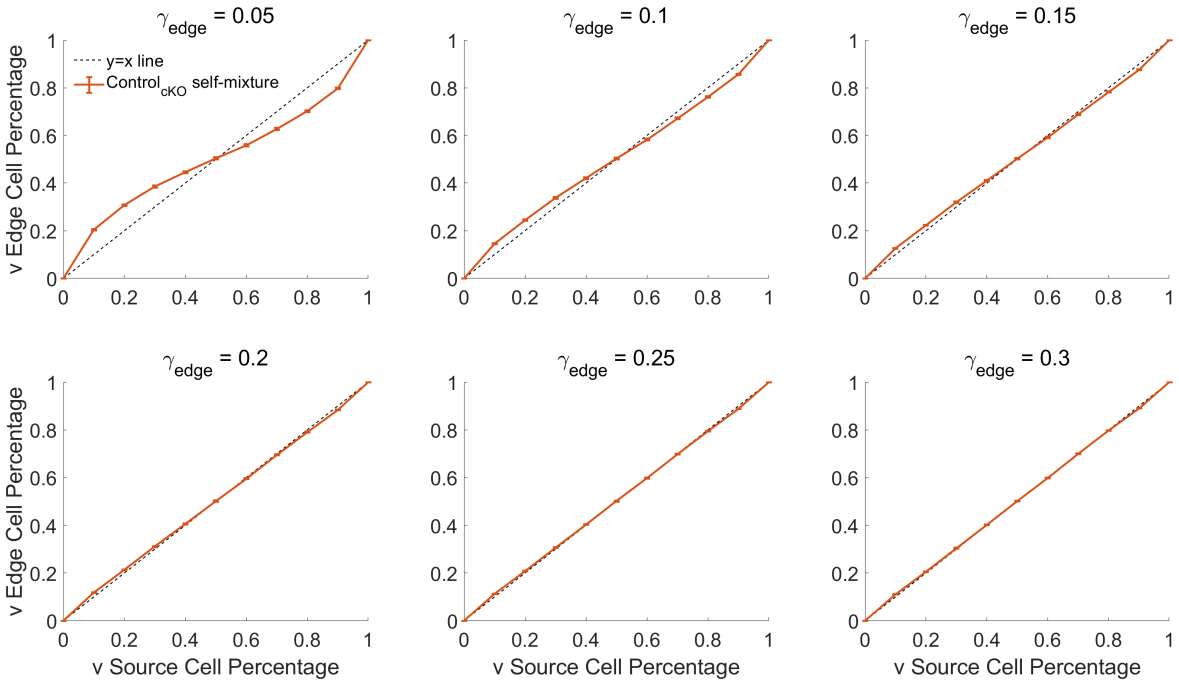

Figure B.4: **The threshold tests in the self-mixture of Control$_{cKO}$ cells.** The model involves self-mixing of Control$_{cKO}$ cells. The figures depict the mean of 100 simulation results, displaying the percentage of v cells in edge cells relative to its source cell percentage, under various edge cell thresholds (γ_{edge}). Error bars indicate the standard error of the mean.

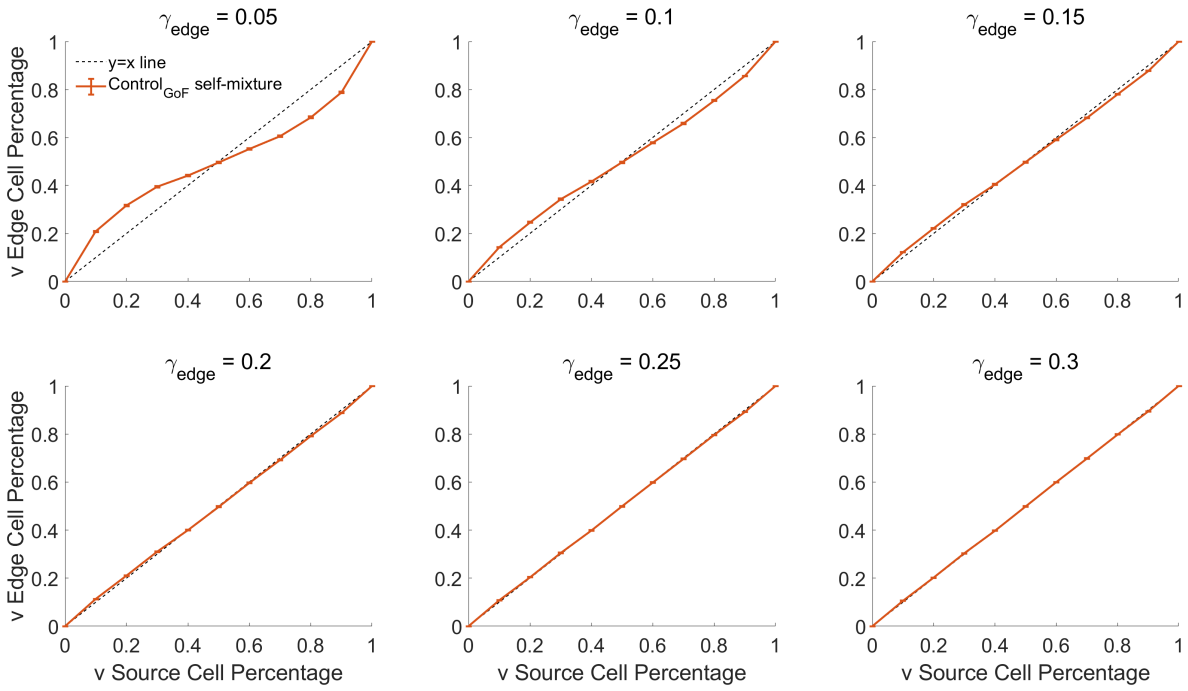

Figure B.5: **The threshold tests in the self-mixture of Control$_{\mathbf{GoF}}$ cells.** The model incorporates self-mixing of Control$_{\mathrm{GoF}}$ cells. The figures illustrate the mean of 100 simulation results, showing the percentage of v cells in edge cells relative to its percentage in source cells, across different edge cell thresholds (γ_{edge}). Error bars represent the standard error of the mean.

results in around 20% of v cells in edge cells when p_v is only 0.1, and approximately 80% of v cells in edge cells when p_v is 0.9. This discrepancy is induced by retraction at the wound edge. In an uneven mixture of u and v cells, for example $p_u > p_v$, the dynamics of the region $u + v < \gamma_{\text{edge}}$ are primarily determined by u cells due to their larger percentage. Consequently, when u cells retract while v cells do not, a substantial portion of v cells are exposed to the region considered as "wound edge cells" expanded by the retraction of u cells, resulting in an overestimation. Conversely, when v cells retract while u cells do not, the impact on u cells is limited due to the small fraction of v cells. This asymmetric mutual impact contributes to the observed pattern under small γ_{edge} (Fig. B.4 and B.5).

While this discrepancy is minor in nature, it gets amplified to a non-negligible extent due to the choice of an excessively small γ_{edge}. Such noise can introduce unexpected bias to our investigation of cell representation near the wound edge. Therefore, to eliminate this bias, we must calibrate the definition of "edge cells" by avoiding the use of overly small γ_{edge}. It's important to note that if we remove the wound edge retraction, which is responsible for this pattern, the percentage of v cells in edge cells exactly matches its percentage in source cells p_v under such pure diffusion (Fig. B.6).

B.1.5 Investigation into counter-intuitive edge cell distribution

In the simulation, when $\text{Control}_{\text{GoF}}$ and *Piezo1*-GoF cells interact repulsively ($\alpha_{uv} < 0$), the percentage of *Piezo1*-GoF cells in backward edge cells was unexpectedly higher than in forward edge cells. This edge cell distribution was counter-intuitive, as the higher PIEZO1 activity in *Piezo1*-GoF cells compared to $\text{Control}_{\text{GoF}}$ cells suggested it would be lower (Fig. B.7).

To elucidate this phenomenon, a series of further simulations were conducted on different mixtures (Table B.2). Test #1 involved mixing $\text{Control}_{\text{GoF}}$ (u cells) and *Piezo1*-GoF (v

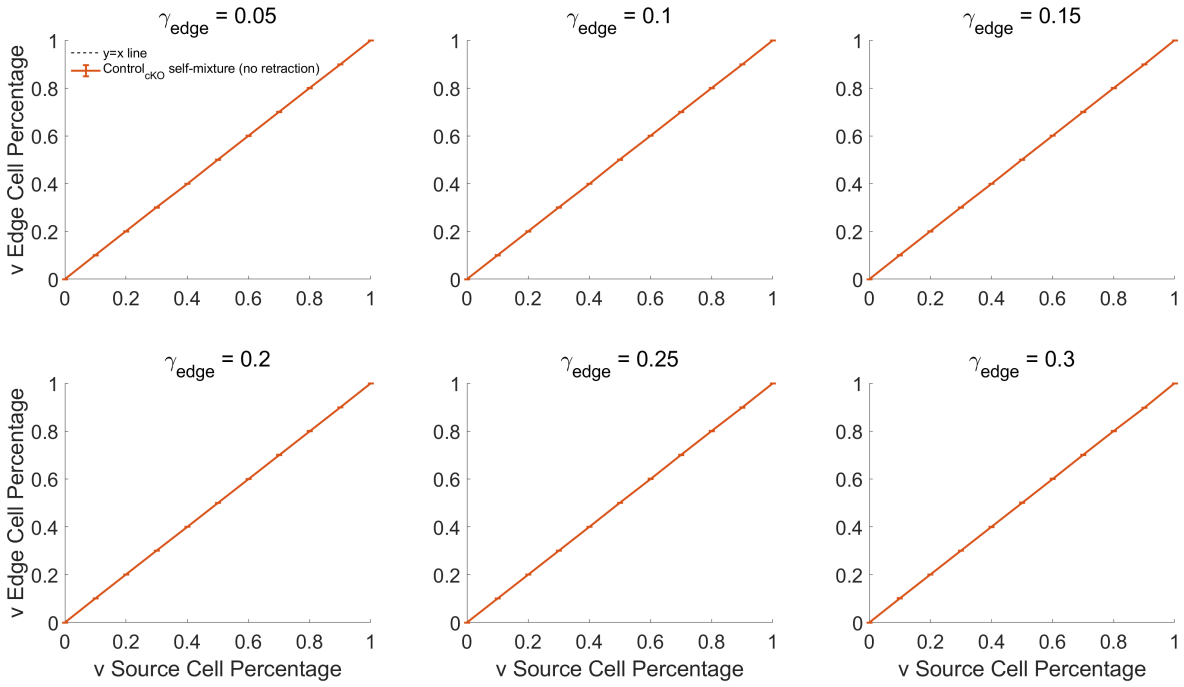

Figure B.6: **The threshold tests in the self-mixture of $\text{Control}_{\text{cKO}}$ cells without retraction.** The model integrates self-mixing of a specific cell type derived from $\text{Control}_{\text{cKO}}$ cells, with retraction removed. The figures illustrate the mean of 100 simulation results, showing the percentage of v cells in edge cells relative to the source cell percentage for v cells, across different edge cell thresholds (γ_{edge}). Error bars represent the standard error of the mean.

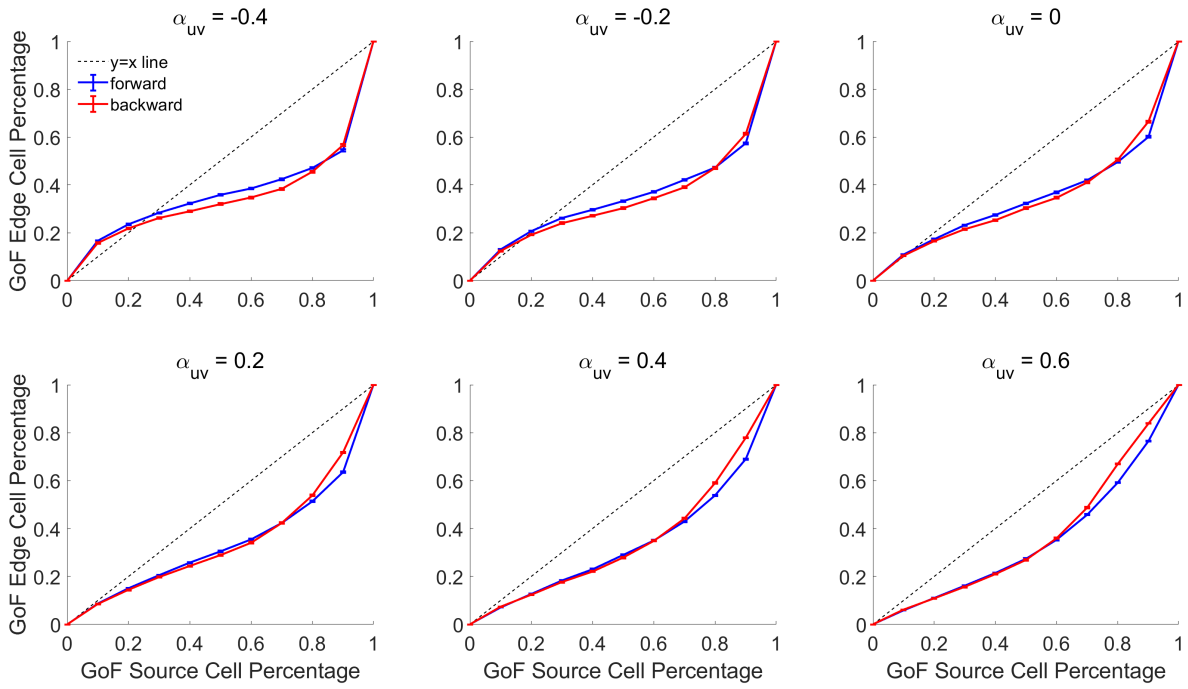

Figure B.7: **The percentage of edge cells in forward and backward directions during mixing Control$_{\mathbf{GoF}}$ and *Piezo1*-GoF cells.** The model involves mixing Control$_{\mathrm{GoF}}$ (u cells) and *Piezo1*-GoF (v cells). Cells at the wound edge are categorized based on their migrating direction: forward or protrusion (*blue*), and backward or retraction (*red*). The figures depict the mean of 100 simulation results, displaying the percentage of v cells in these two specific types of edge cells relative to the source cells' v cell percentage, under various interaction coefficient (α_{uv}). Error bars indicate the standard error of the mean.

cells), while #2 to #6 adjusted v cell parameters while keeping u cells unchanged. Initially, we investigated whether this phenomenon stemmed from retraction-related parameters or coordinated directionality. Tests #2 and #3 revealed that retraction-related parameters primarily contributed, while coordinated directionality had minimal effects. Subsequently, we sought to identify which specific parameter related to wound edge retraction played the primary role. Individual parameter changes in tests #4, #5, and #6 indicated that retraction strength was paramount. Hence, we hypothesize that the counter-intuitive phenomenon mainly arises from retraction strength.

When mixing u cells and v cells, with v cells receiving stronger retraction strength than u cells, the wound edge primarily comprises u cells (resulting in u cells being over-represented

#	u Cells	v Cells, Calibrated Based on u Cells				Results
		Retraction Strength	Retraction Duration	Inter-retraction Duration	Coordinated Directionality	
1	${}^{CM}\text{Control}_{\text{GoF}}$	+	+	−	−	✗✗
2		∼	∼	∼	−	✗
3		+	+	−	∼	✗✗
4		+	∼	∼	∼	✗✗
5		∼	+	∼	∼	✗
6		∼	∼	−	∼	✗
7	${}^{CM}\text{DMSO}$	+	−	−	∼	✓
8		+	∼	∼	∼	✗✗
9		+	−	∼	∼	✓

Table B.2: **Forward and backward edge cell distributions in model simulations.** Summary table presenting simulation outcomes using the calibrated model ($^{\text{CM}}$) to determine whether the percentage of v cells in backward edge cells surpasses that in forward edge cells under modified model parameters. A "+" indicates a parameter set has a predicted increase upon an experimental measure while a "−" indicates a predicted decrease. A check mark (✓) indicates that model simulation consistently demonstrates a higher percentage of v cells in backward edge cells compared to forward edge cells across various p_v and α_{uv} values. A cross mark (✗) indicates the absence of such a trend, implying that there are combinations of p_v and α_{uv} where the percentage of v cells in backward edge cells is lower than in forward edge cells. Double cross marks (✗✗) highlight cases where this lower percentage is significantly more prominent than instances with a single cross mark (✗).

in edge cells). Consequently, the backward movement of the wound edge depends more on u cells. If the interaction between u and v cells is expelling (e.g., $\alpha_{uv} = -0.4$), the retracted u cells would exert further pressure on v cells, pushing them backward into the inner monolayer. This would make v cells even more under-represented in the backward edge cells compared to their percentage in the forward edge cells. However, when the percentage of v cells is large, this pushing force is diminished, as v cells outnumber u cells, making it harder for u cells to push them backward. It's worth noting that mixtures involving Yoda1-treated cells also exhibit strong retraction on v cells, but high-frequency short-duration retraction mitigates this effect. This trend was observed in test #7. Conversely, when only retraction strength was applied without shortening the retraction duration (test #8), the same phenomenon as the *Piezo1*-GoF case was observed, and shortening the retraction duration rescued this trend (test #9).

To further validate our hypothesis, we measured the percentage of v cells in forward and backward edge cells across various thresholds γ_{edge} defining edge cells (Fig. B.8). These simulations, performed in the mixture of $\text{Control}_{\text{GoF}}$ and *Piezo1*-GoF under $\alpha_{uv} = -0.4$ and $p_v = 0.5$, confirmed our hypothesis that v cells are retracted to the inner monolayer. Specifically, when the threshold γ_{edge} is small, indicating proximity to the wound edge, the backward edge cell percentage is smaller than the forward edge cell percentage, as observed earlier. However, when the threshold γ_{edge} exceeds 0.4, indicating the inner monolayer, the backward edge cell percentage is higher than the forward edge cell percentage, as we hypothesized.

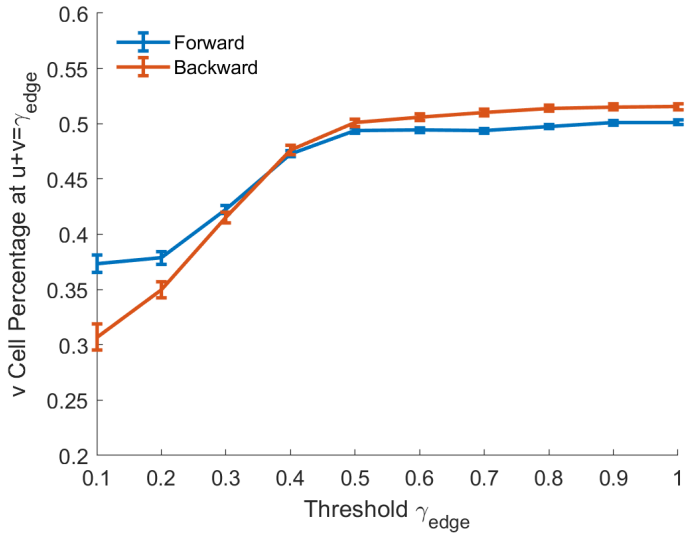

Figure B.8: **Edge cell distribution across thresholds.** This figure illustrates the percentage of v cells at the wound edge across various thresholds (γ_{edge}), specifically under conditions where $\alpha_{uv} = -0.4$ and $p_v = 0.5$. The lines represent the mean, while error bars denote the standard error of the mean, derived from 1182 data points for forward moments and 539 data points for backward moments.

B.1.6 Supplementary figures

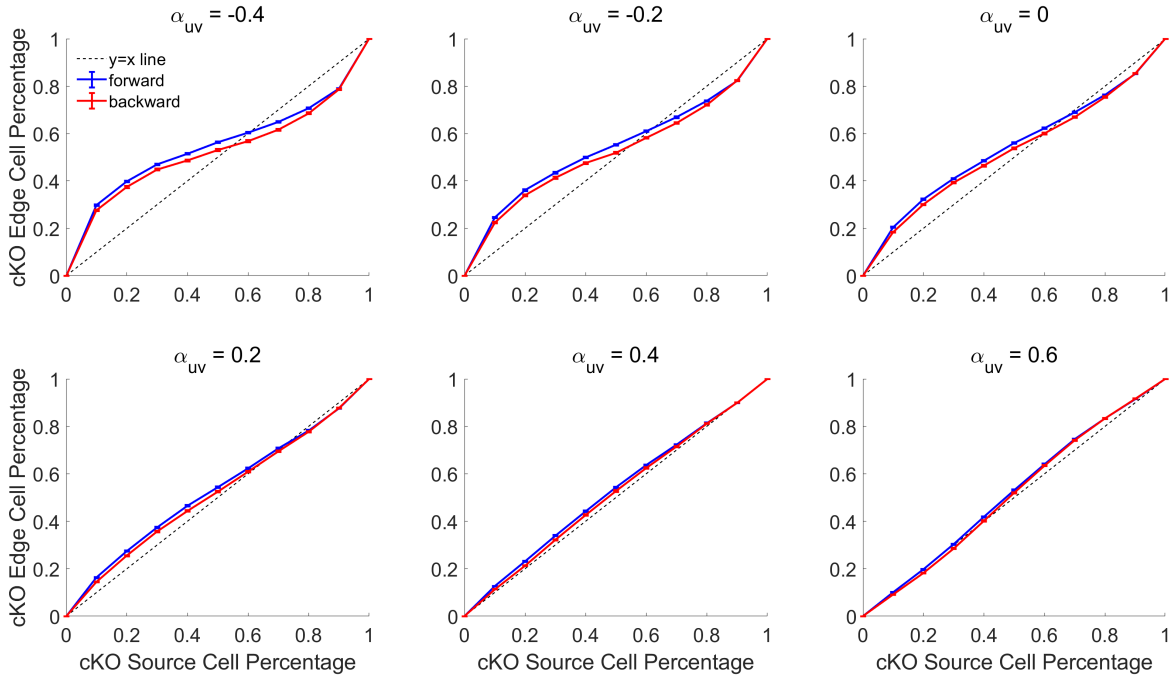

Figure B.9: **The percentage of edge cells in forward and backward directions during mixing Control$_{\mathbf{cKO}}$ and *Piezo1*-cKO cells.** The model involves mixing Control$_{\text{cKO}}$ (u cells) and *Piezo1*-cKO (v cells). Cells at the wound edge are categorized based on their migrating direction: forward or protrusion (*blue*), and backward or retraction (*red*). The figures depict the mean of 100 simulation results, displaying the percentage of v cells in these two specific types of edge cells relative to the source cells' v cell percentage, under various interaction coefficient (α_{uv}). Error bars indicate the standard error of the mean.

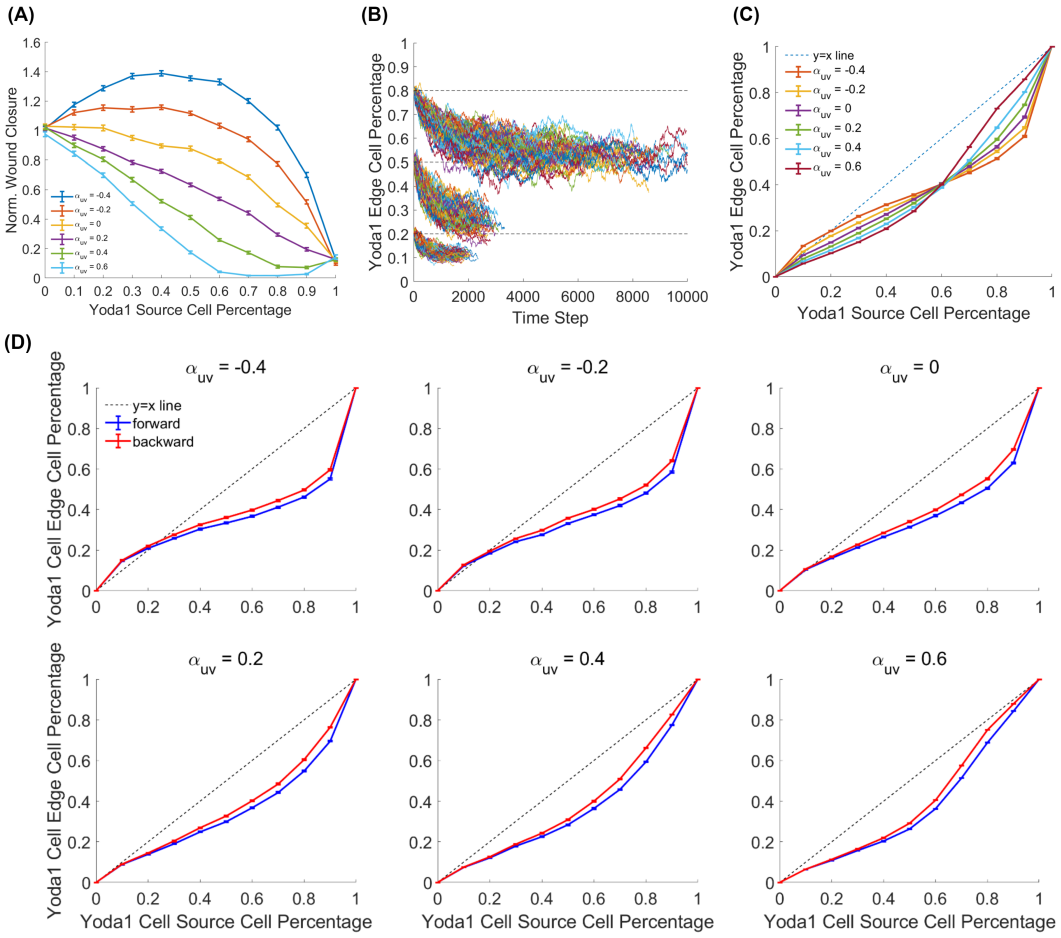

Figure B.10: **The mixture of DMSO-treated and Yoda1-treated cells.** The model involves mixing DMSO-treated (u cells) and Yoda1-treated (v cells). **(A)** Line graphs illustrate the mean of 100 simulation results, displaying the normalized wound closure versus the Yoda1-treated source cell percentage. Error bars indicate the standard error of the mean. The various colored lines denote different interaction coefficient values (α_{uv}). **(B)** Line graphs within each cluster represent 100 individual tracks (300 total trajectories in the figure), demonstrating the evolution of Yoda1-treated (v cells) percentage in edge cells over simulation time steps during wound closure. The clusters correspond to distinct source cell conditions, with Yoda1-treated (v cells) percentages set at 20% (*bottom* cluster), 50% (*middle* cluster), and 80% (*top* cluster). These levels are indicated by black dashed lines. **(C)** Line graphs illustrate the mean of 100 simulation results, displaying the percentage of Yoda1-treated (v cells) cells in edge cells versus the percentage in source cells. The various colored lines denote different interaction coefficient values (α_{uv}), and error bars indicate the standard error of the mean. **(D)** Cells at the wound edge are categorized based on their migrating direction: forward or protrusion (*blue*), and backward or retraction (*red*). The figures depict the mean of 100 simulation results, displaying the percentage of v cells in these two specific types of edge cells relative to the source cell percentage for v cells, under various interaction coefficient (α_{uv}). Error bars indicate the standard error of the mean.

Parameter	Notation	Base Value
retraction strength	$\mu_{s,u}$, $\mu_{s,v}$	30
retraction duration	$\mu_{r,u}$, $\mu_{r,v}$	2×10^{-3}
inter-retraction duration	$\mu_{nr,u}$, $\mu_{nr,v}$	1×10^{-3}
cell motility	d_u, d_v	1
cell-cell adhesion	α_{uu}, α_{vv}	0.2
interaction coefficient	α_{uv}	0.2
coordinated directionality	$w_{A,u}$, $w_{A,v}$	0.4
u source cell percentage	p_u	0.5
v source cell percentage	p_v	0.5
grid size	h	0.01
threshold for wound edge cells	γ_{edge}	0.2
retraction width	ω_r	0.2
boundary mean	μ_0	0.6
boundary standard deviation	σ_0	0.3
Heaviside smoothing steepness	k	10
spatial smoothing width	k_1^s	0.3
spatial smoothing steepness	k_2^s	3
temporal smoothing width	k_1^t	0.5
temporal smoothing steepness	k_2^t	10

Figure B.11: **List of parameters and their base values for the heterogeneous PIEZO1 model.**

Appendix C

Experimental methods and materials

C.1 Ethics statement

All studies were approved by the Institutional Animal Care and Use Committee of University of California at Irvine and The Scripps Research Institute and performed within their guidelines.

C.2 Materials

C.2.1 Animals

Keratinocyte samples from *Piezo1*-cKO and *Piezo1*-GoF mice were a gift from Dr. Ardem Patapoutian's lab, the Scripps Research Institute. *Piezo1*-tdTomato reporter mice (*Piezo1*-tdTomato; JAX stock 029214), *Piezo1*-cKO and *Piezo1*-GoF mice were generated in previous studies [35, 70].

C.2.2 Keratinocyte isolation and culture

Primary keratinocytes were isolated from the upper dorsal skin of P0-P5 mice as previously described [35]. Briefly, dissected tissue was allowed to dissociate for 15-18 hours. After dissociation, the epidermis was separated and incubated in Accutase (CellnTec CnT-Accutase-100) for 30 minutes at room temperature. Subsequently, the epidermis was transferred to a dish of CnT-Pr media (CellnTec), supplemented with 10% FBS and 1% penicillin/streptomycin where the epidermis was minced and then agitated using a stir plate for 30 min. After agitation, cells were strained through a 70 μm cell strainer (Falcon). Strained cells were spun down and resuspended in CnT-Pr media (CellnTec) supplemented with ISO-50 (1:1000) (CellnTec) and Gentamicin (50 μg/ml) (Thermo Fisher).

Isolated keratinocytes were seeded directly onto the glass region of #1.5 glass-bottom dishes (Mat-Tek Corporation) coated with 10 μg/ml fibronectin (Fisher Scientific, CB-40008A). For single cell migration experiments, isolated cells were sparsely seeded onto the glass region at 1.5×10^4 cells/dish while for monolayer scratch assay experiments, isolated cells were densely seeded onto the glass region at a density of $1.5\text{x}10^5$ cells/dish. One day after seeding, CnT-Pr supplemented culture media (see above) was switched to Cnt-Pr-D media (CellnTec) to promote keratinocyte differentiation. Keratinocytes were imaged 3 days after primary isolation, allowing at least 2 days for keratinocyte differentiation in Cnt-Pr-D media (CellnTec).

C.2.3 Microscopy

For *in vitro* image acquisition, an Olympus IX83-ZDC inverted microscope equipped with a SOLA light engine (Lumencor) was utilized. For time-lapse imaging experiments, a full enclosure stage-top incubator system (Tokai Hit) enabled cells to be imaged at 37°C with 5% CO_2 to maintain optimal cell health. μManager, an open-source microscopy controller

software, was used for microscope hardware control and image acquisition [21, 22]. For all experimental data, images were taken using a UPlanSApo 10× dry objective with a numerical aperture of 0.40 and acquired using a Hamamatsu Flash 4.0 v2+ scientific CMOS camera.

C.3 Experiments

C.3.1 Immunofluorescence staining

For immunostaining of healing monolayers in Fig A.12, scratch wounds were generated in confluent monolayers of isolated keratinocytes and then treated with either 4 μM Yoda1, or the equivalent concentration of the solvent DMSO, before allowing the monolayers to collectively migrate. 24 hours after initial wounding the monolayers, monolayers were fixed and then immunostained for total levels of Rac1 (Fig A.12, *left*) and RhoA (Fig A.12, *right*). Immunostaining was performed as previously described [67] using the following antibodies: Mouse anti-Rac1 (Millipore Cat#05-389-25UG, 1:200), Rabbit anti-RhoA (Proteintech Cat#10749-1-AP, 1:100), Donkey anti-Mouse 647 (Abcam Cat#AB150107, 1:500), Goat anti-Rabbit 488 (Life Sciences Cat#A32731, 1:500). Nuclei were stained by Hoechst (Invitrogen Cat#H1399) at 1μg/mL for 5 minutes.

C.3.2 Single cell migration assay

As previously described [35], time lapse sequences of DIC images were taken at 5 minute intervals. In brief, sparsely seeded keratinocytes were allowed to migrate for 16.67 hr at 37°C with 5% CO_2 in fibronectin-coated glass-bottom dishes. Cell centroids were tracked using Cell Tracker (https://celltracker.website/index.html, Piccinini2016-dx) and resulting trajectories were analyzed using the cell trajectory analysis software, DiPer [28].

C.3.3 Wound closure assay

Primary keratinocytes were cultured for 3 days until they formed a confluent monolayer. Prior to imaging experiments, cell nuclei were labeled by addition of SiR-Hoechst [58] (1 μM; Cytoskeleton Inc.) to Cnt-Pr-D+1.2 mM Ca^{2+} bath media for 1 hour prior to imaging. As previously described, monolayer scratches were generated using a 10 μl pipette tip and resulting cell debris was removed by performing three successive washes of culturing media [35, 55]. Time-lapse imaging series of wound closure were acquired by taking sequential DIC and fluorescence images at multiple positions. 1 μM SiR-Hoechst remained in the Cnt-Pr-D+1.2 mM Ca^{2+} bath media throughout the imaging period. For Yoda1 experiments, 4 μM Yoda1 or, as a control, the equivalent concentration of DMSO was supplemented to bath media prior to imaging. Leader cells display broad lamellipodia and are located at the front of protrusions along the leading edge of healing monolayers. During identification, leader cells were identified by manually reviewing time lapse image series and counting the number of cells located at the front of fingering protrusions at the leading edge which display increased polarization and large, prominent lamellipodia. Example leader cells identified during manual review are denoted by white arrows within Fig A.1. The number of leader cell formations is reported at the time point when either the wound interfaces touch or the imaging period finishes.

C.4 Analysis

C.4.1 Wound edge length analysis

Monolayer sheets were segmented from images taken during wound closure assays using a custom deep-learning based U-net architecture written in Python [74]

(https://github.com/Pathak-Lab/PIEZO1-Collective-Migration). The length of the segmented wound edge was calculated by taking the cumulative euclidean distance between all detected pixel positions along the segmented monolayer leading edge. Due to any possible differences in edge length which might arise when manually making scratches in monolayers, each field of view's edge length was normalized by dividing the edge length at T_{final}, the time point when either the wound interfaces touch or the imaging period finishes by T_0, the starting edge length at the starting time point for a field of view. This normalized edge length was used as a measure of the prevalence of leader cells along the wound edge for a given condition.

C.4.2 Image analysis

Using the open-source image analysis software Fiji [75] the signal-to-noise ratio of SiR-Hoechst images was increased using Contrast Limited Adaptive Histogram Equalization (CLAHE) (https://imagej.net/plugins/clahe) prior to further analysis. For some images which had poor labeling of SiR-Hoechst, the denoising algorithm Noise2Void was also used to further increase the signal-to-noise ratio of nuclei images [46] (Fig A.13).

C.4.3 Individual cell tracking

We combined the deep learning-based object detection method StarDist with the cell tracking software TrackMate to perform automated tracking of cells within monolayers [23, 24, 82]. Cell trajectories harvested using TrackMate were then exported for further analysis. Due to the technical limitations surrounding Microsoft Excel's ability to handle large datasets, we developed Cell_Pyper (https://github.com/Pathak-Lab/PIEZO1-Collective-Migration) a Pythonic analysis pipeline based on the open-source algorithm DiPer [28] to analyze the Mean Squared Displacement (MSD), Speed and Velocity autocorrelation of harvested cell

trajectories.

For efficient computation of a trajectory's MSD, MSDs are computed according to Eq. C.1 (Eq. 4.11 in [12]) where $r(k) \equiv r(k\Delta t)$ is a cell trajectory consisting of N_t timepoints and the MSD is calculated for timestep m.

$$\Delta^2(m) = \frac{1}{N_\mathrm{t} - m} \sum_{k=0}^{N_t - m - 1} [r(k+m) - r(k)]^2 \quad m = 0 \ldots N_t - 1 \tag{C.1}$$

As described by Gorelik & Gautreau (Eq. 6 and 7 in [28], Velocity Autocorrelation analysis is calculated according to equations C.2 and C.3 for a trajectory consisting of N timepoints with a time-step of Δt=5 min. A normalization factor (Norm; Eq. C.2) is initially calculated for velocity vector v_i with starting coordinates (x_i, y_i) which is used to calculate the average velocity autocorrelation coefficient v_{ac} with step size n.

$$\begin{aligned} \mathrm{Norm} &= \frac{1}{N} \Sigma_{i=0}^{N-1} |\bar{v}|_i^2 \\ &= \frac{1}{N^*(\Delta t)^2} \Sigma_{i=0}^{N-1} \left[(x_i - x_{i+1})^2 + (y_i - y_{i+1})^2 \right] \end{aligned} \tag{C.2}$$

$$\begin{aligned} v_{ac}(n) &= \frac{1}{N-n} \left(\Sigma_{i=0}^{N-n} \bar{v}_i \cdot \bar{v}_{i+n} \right) * \frac{1}{\mathrm{Norm}} \\ &= \frac{1}{N-n} \Sigma_{i=0}^{N-n} \left[\frac{(x_i - x_{i+1})(x_{i+n} - x_{i+n+1}) + (y_i - y_{i+1})(y_{i+n} - y_{i+n+1})}{(\Delta t)^2} * \frac{1}{\mathrm{Norm}} \right] \end{aligned} \tag{C.3}$$

C.4.4 Particle image velocimetry analysis

Particle Image Velocimetry (PIV) analysis was performed using the Python implementation of OpenPIV [56] (https://github.com/Pathak-Lab/PIEZO1-Collective-Migration). We use multiple passes of interrogation window sizes, initially using first-pass calculations with a 64 pixel x 64 pixel (55.2 μm x 55.2 μm) window followed by two iterations of 32 x 32 (27.6 μm x 27.6 μm) pixel windows and two iterations of 16 x 16 pixel (13.8 μm x 13.8 μm) windows. Each interrogation window was computed with a 50% overlap. A signal-to-noise filter (Threshold=1.3) was used on detected velocity vectors to remove any vector outliers. Outputs produced by OpenPIV analysis were then used to generate PIV flow fields as shown in Fig 3.3A-C. Working from the flow fields, individual PIV vectors were isolated and PIV vector direction was calculated and normalized to 0° to account for differences in angles of scratches made in monolayers (https://github.com/Pathak-Lab/PIEZO1-Collective-Migration). Vector direction distributions are illustrated as the probability density distribution across experimental replicates in Fig 3.3D-F. The von Mises distribution was employed to fit vector direction datasets by minimizing the mean squared error between the vector direction data and the von Mises probability density function. The resulting fitted curves represent the best approximation of the data by adjusting the parameters μ (mean) and κ (concentration or strength) of the von Mises distribution. The parameter μ represents the location where the distribution is clustered, while parameter κ indicates the level of directionality in our experimental context. The probability density function of the von Mises distribution for the vector direction angle x is expressed as:

$$f(x|\mu,\kappa) = \frac{exp(\kappa \cos x - \mu)}{2\pi I_0(\kappa)}, \tag{C.4}$$

where $I_0(\kappa)$ represents the modified Bessel function of the first kind with order 0

$$I_0(\kappa) = \frac{1}{\pi}\int_0^{\pi} e^{x\cos\theta} d\theta, \tag{C.5}$$

which is selected to ensure the distribution integrates to unity:

$$\int_{-\pi}^{\pi} exp(\kappa\cos x)dx = 2\pi I_0(\kappa). \tag{C.6}$$

The variance of PIV vector directions within a field of view was calculated as the mean angular deviation, z, where z is defined in Eq. C.7 (Eq. 2 in [49]). Outputs of this equation are bounded such that zero indicates no variability in vector direction within a flow field and one indicates high variability in vector direction.

$$z = \frac{1}{N}\left[\left(\sum_i^N \cos\theta_i\right)^2 + \left(\sum_i^N \sin\theta_i\right)^2\right]^{1/2} \tag{C.7}$$

The spatial autocorrelation function, C , is computed according to Eq. C.8 (Eq. 4 in [49]) using the radial velocity component of a given PIV vector, v, within a vector flow field at varying length scales, r.

$$C(\Delta r) = \frac{\Sigma_{r_i} v\left(r_i\right) \cdot v\left(r_i + \Delta r\right)}{\sqrt{\Sigma_{r_i} v_i^2\left(r_i\right) \cdot \Sigma_{r_i} v^2\left(r_i + \Delta r\right)}} \tag{C.8}$$

For measurement of the local autocorrelation in vector direction, the spatial autocorrelation

at $\Delta r = 150$ μm was used to capture correlation of motion at multiple cell lengths. Length constants were calculated by using OriginLab to fit an exponential function whose exponent is a 2$^{\text{nd}}$ order polynomial (Eq. C.9) to the spatial autocorrelation dataset and calculating the distance at which $C(\Delta r) \approx 0.37$.

$$y = e^{a+bx+cx^2} \tag{C.9}$$

C.4.5 Statistical analysis

P values, statistical tests, and sample sizes are declared in the corresponding figures. All datasets were tested for normality using the Shapiro-Wilk test prior to statistical analysis. The two-sample t-test was used where data were modeled by a normal distribution and a nonparametric test was used in the case of non-normal distributions. Cumming estimation plots were generated and Cohen's d value was calculated using the DABEST python [32] (https://github.com/ACCLAB/DABEST-python). The Cohen's d effect size is presented as a bootstrap 95% confidence interval (95% CI) on a separate axes. p values for Fig 3.3G-I are declared in Fig A.11.